AD-A082 003 WASHINGTON STATE UNIV PULLMAN DEPT OF PHYSICS F/G 11/6
SHOCK-INDUCED MARTENSITE REVERSAL IN FE/30%NI.(U)
FEB 80 G E DUVALL, P M BELLAMY, R J LIVAK DAAG29-77-C-0030
UNCLASSIFIED ARO-14619.1-MS NL

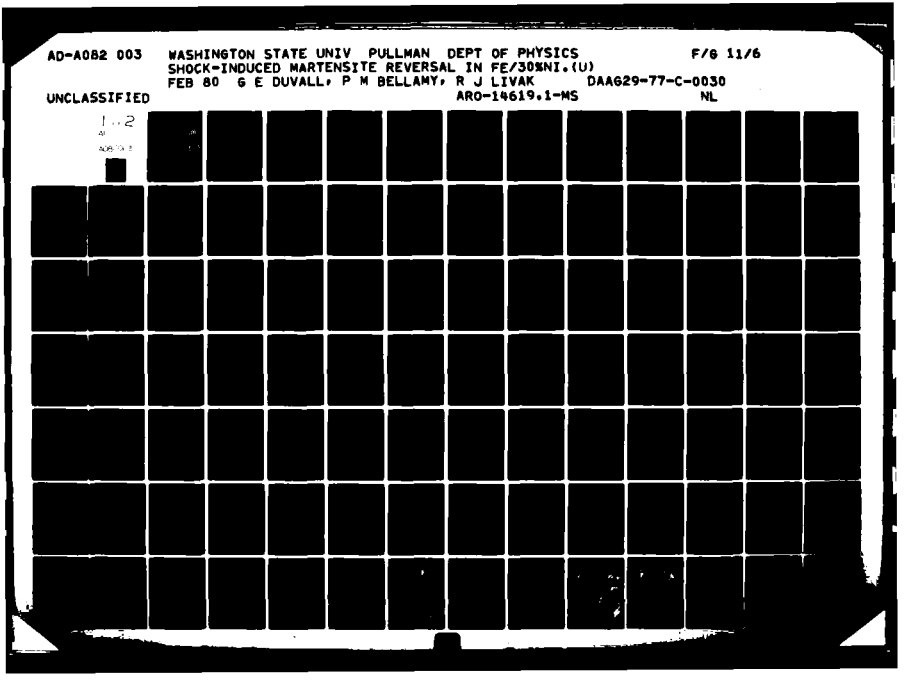

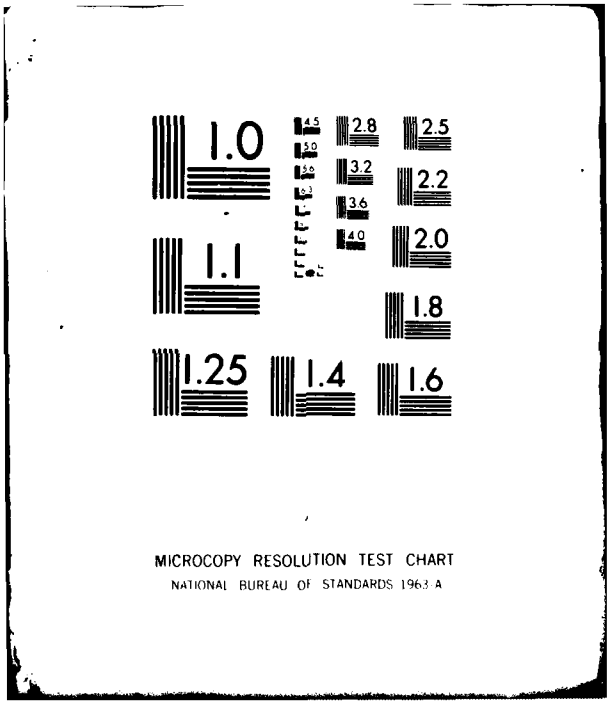
1.0
1.1
1.25
1.4
1.6
1.8
2.0
2.2
2.5
2.8
3.2
3.6
4.0
4.5
5.0
MICROCOPY RESOLUTION TEST CHART
NATIONAL BUREAU OF STANDARDS 1963-A

(19) ARO 14619.1-MS

(12) B.S.

(6) SHOCK-INDUCED MARTENSITE REVERSAL IN Fe/30%Ni.

(9) Final Report. 16 Sep 77-15 Sep 79

(10) George E. Duvall and Paul M. Bellamy
Shock Dynamics Laboratory
Department of Physics

and

Ronald J. Livak
Department of Materials Science and Engineering

(11) 14 Feb 1980

(12) 105

U. S. Army Research Office
Contract No. (15) DAAG29-77-C-0030

Washington State University
Pullman, WA 99164

401957

The findings of this report are not to be construed as an official Department of the Army position, unless so designated by other authorized documents.

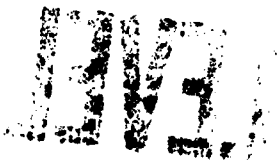

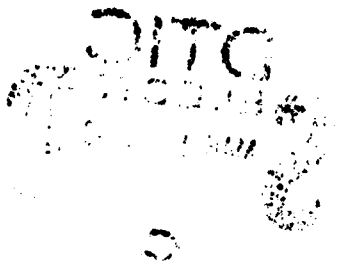

UNCLASSIFIED

SECURITY CLASSIFICATION OF THIS PAGE (When Data Entered)

REPORT DOCUMENTATION PAGE		READ INSTRUCTIONS BEFORE COMPLETING FORM
1. REPORT NUMBER	2. GOVT ACCESSION NO.	3. RECIPIENT'S CATALOG NUMBER
4. TITLE (and Subtitle) SHOCK-INDUCED MARTENSITE REVERSAL IN Fe/30%Ni		5. TYPE OF REPORT & PERIOD COVERED Final Report, 9/15/77 - 2/14/80
		6. PERFORMING ORG. REPORT NUMBER
7. AUTHOR(s) George E. Duvall, Paul M. Bellamy, and Ronald J. Livak		8. CONTRACT OR GRANT NUMBER(s) DAAG29-77-C-0030
9. PERFORMING ORGANIZATION NAME AND ADDRESS Department of Physics Washington State University Pullman, Washington 99164		10. PROGRAM ELEMENT, PROJECT, TASK AREA & WORK UNIT NUMBERS ARO P-14619-MS
11. CONTROLLING OFFICE NAME AND ADDRESS U. S. Army Research Office P.O. Box 12211 Research Triangle Park, N.C. 27709		12. REPORT DATE February 14, 1980
		13. NUMBER OF PAGES 82
14. MONITORING AGENCY NAME & ADDRESS(if different from Controlling Office)		15. SECURITY CLASS. (of this report) unclassified
		15a. DECLASSIFICATION/DOWNGRADING SCHEDULE

16. DISTRIBUTION STATEMENT (of this Report)

Approved for public release; distribution unlimited

17. DISTRIBUTION STATEMENT (of the abstract entered in Block 20, if different from Report)

18. SUPPLEMENTARY NOTES

19. KEY WORDS (Continue on reverse side if necessary and identify by block number)

phase transitions
shock waves
martensite
Fe-Ni

20. ABSTRACT (Continue on reverse side if necessary and identify by block number)

It is pointed out that variations of shear stress in a solid undergoing transition may have an important effect on the conditions under which transitions occur. Such variations are not calculable from present knowledge, and for practical reasons description of the state of shear during the transition must be made part of the constitutive relations. The difficulty of defining a Gibbs energy in a solid is pointed out and the thermodynamic problems are indicated in some details. Experiments are described which promise to reveal

DD FORM 1 JAN 73 1473

UNCLASSIFIED

SECURITY CLASSIFICATION OF THIS PAGE (When Data Entered)

the state of shear in the α-γ transition in Fe/30%Ni at high temperatures using shock wave methods. Attempts to carry out these experiments are described, and numerical calculations of phase transitions with and without shear stress show that characteristic shock wave structures do indeed result from various shear conditions during transformation. Transformation experiments at various initial temperatures suggest that there may be a third phase--perhaps ε--which is reached in shock experiments for modest driving pressures and for initial temperatures less than 200°C. A description of the metallographic state after shock transition is given. There is minimal evidence that the shear stresses were sharply reduced for initial temperatures of 400°C.

TABLE OF CONTENTS

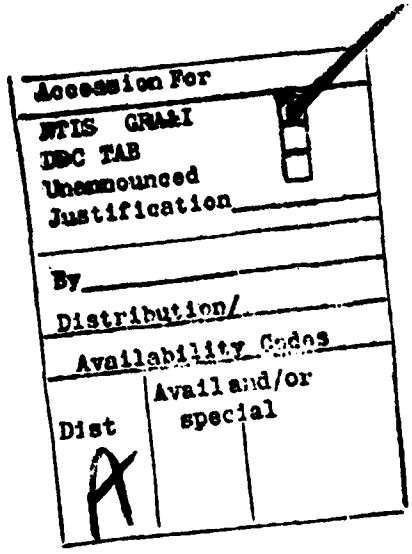

FOREWORD

This work was carried out principally over a period of two years from September 16, 1977 to September 15, 1979. During most of this period progress suffered somewhat from lack of adequate metallurgical advice and assistance. Dr. Ronald J. Livak of the WSU Department of Material Science and Engineering joined us for the summer of 1979 and contributed materially during that brief period to our progress and understanding. His formal work is reported in a "Metallurgical Report" included as Part B of this final report. His total contribution through insight and understanding he shared with us greatly exceeded this formal report, substantial though it is. During the early part of the work we were fortunate to have the counsel via telephone of Dr. Richard Rohde of Sandia Laboratories, whose earlier work provided the motivation for that reported here.

PART A

G. E. Duvall and P. M. Bellamy

I. Introduction

The role of shear stress in phase transitions is controversial and the questions involved are implicit in the work of Gibbs, though he was wise enough to avoid discussion of the problem. What he did was to show how thermodynamics applies to a solid-liquid system which can be reduced to a set of thermodynamic variables involving only one stress parameter, the hydrostatic pressure (Gibbs, 1971). His treatment is relatively straightforward and unquestionably correct. The basic difficulty lies in the meaning of the "Gibbs function," which is well-defined for a system with only one stress parameter and does not exist for multiparameter systems. (The function defined in many texts by Legendre transformation from the free energy and called the Gibbs function does not play the role in phase transitions that the hydrostatic Gibbs function does). Some simple aspects of the problem are described below; more detailed reviews and calculations have been given by Kamb (1961), Paterson (1973), and Robin (1974). In the simple and quite unrealistic example of non-hydrostatic transition treated below, thermodynamics says nothing about the effect of transition on the shear stress; that must be supplied as an additional hypothesis.

Before launching into details of examples, some preliminary remarks are in order. We first consider the stress deviations in uniaxial strain and some consequences of their collapse.

1.1 Collapse of Stress Deviators

With all other factors being equal, it is clear that a transformed nucleus growing in a parent matrix will have less energy if it harbors no

shear stress than if it does. Then one's simple expectation is that mean shear stress in a material undergoing polymorphic transition will be reduced by transformation, at least in its early stages. Given the non-equilibrium and inhomogeneous aspects of transformation in real materials, it is by no means evident that this will indeed occur in a shock wave. Some experimental evidence exists to indicate that it does.

Whereas impact in real systems involves complicated three dimensional stress systems, shock experiments are usually done in plane geometry, in which strain is uniaxial in the direction of propagation. When an isotropic elastic material is compressed uniaxially to a pressure $p_z \equiv -\sigma_z$ in the direction of compression, maximum resolved shear stress and hydrostatic pressure are*

$$\tau = -\frac{(1 - 2\nu)}{2(1 - \nu)} p_z \qquad (1)$$

$$= -p_z/3 \qquad \text{for Poisson's ratio, } \nu = 1/4$$

$$p = \frac{1 + \nu}{3(1 - \nu)} p_z \qquad (2)$$

$$= 5p_z/9 \qquad \text{for } \nu = 1/4$$

Ductile materials yield when τ is large enough; brittle materials fracture. The stress deviators in uniaxial compression are $S_x = 4\tau/3$, $S_y = S_z = -2\tau/3$, $S_{ij} = 0$, $i \neq j$.

If a material can exist in either of two phases under given conditions of temperature and pressure, the stable or equilibrium phase is that with the lower Gibbs energy; i.e. the material transforms to lower its Gibbs energy. Solid-solid or polymorphic phase transitions at high pressure are normally studied under near-hydrostatic conditions, and only pressure and temperature contributions to the Gibbs energy need be considered. In shock compression

* Equation numbers start with (1) in each section. Reference to equations in another section is made by appending the section number, e.g. (1-1).

of high strength materials, the hydrostatic component of stress may be accompanied by very large shear or deviatoric components. In such cases it is anticipated that phase transformations, when they occur, will occur so as to reduce the shear contribution to the Gibbs energy, as well as the pressure and temperature contributions. This is illustrated in Fig. 1.1: a material might be driven to a state A in phase I, and it would transform to a state B in phase II in order to reduce G, both without shear. With combined pressure and shear stress it might be driven to A'; it would still be expected to transform so as to approach the point B' in phase II without shear. That is the nuclei in phase II would attempt to align and orient themselves so as to minimize the total Gibbs energy.

If the material at A' had been on the point of fracturing because of shear stresses present in phase I, the danger of fracture would have been diminished by the transformation. There exists fragmentary evidence that this can occur in shock compression.

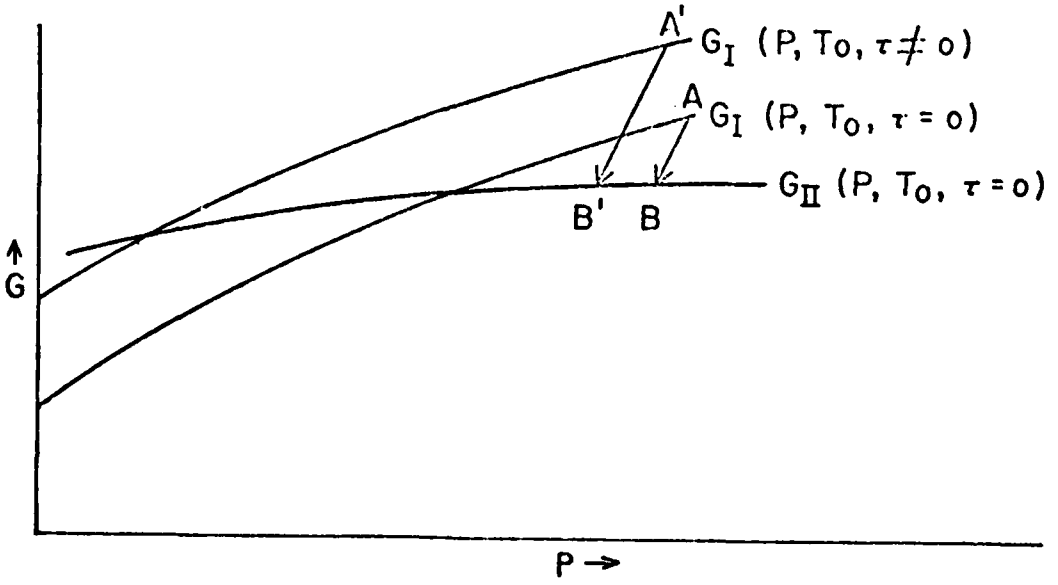

Fig. 1.1 Reduction of Gibbs Energy by Phase Transformation

Fig. 1.2 is a tracing of a quartz gage record obtained for an impact-produced shock wave which has propagated through a single crystal of CdS in the direction of the c-axis. The first arrival, at the left of the trace, has propagated with elastic velocity. The second arrival, at the far right, has propagated with a velocity which indicates the material has partially or completely transformed between the times of first and second arrivals. The authors of this work identify the relatively flat region between first and second arrivals with the polymorphic phase transition known to occur at 27 kilobars. The difference between 27 and 31.5 kbar may represent residual shear stress or incomplete transformation. The basic concept seems correct.

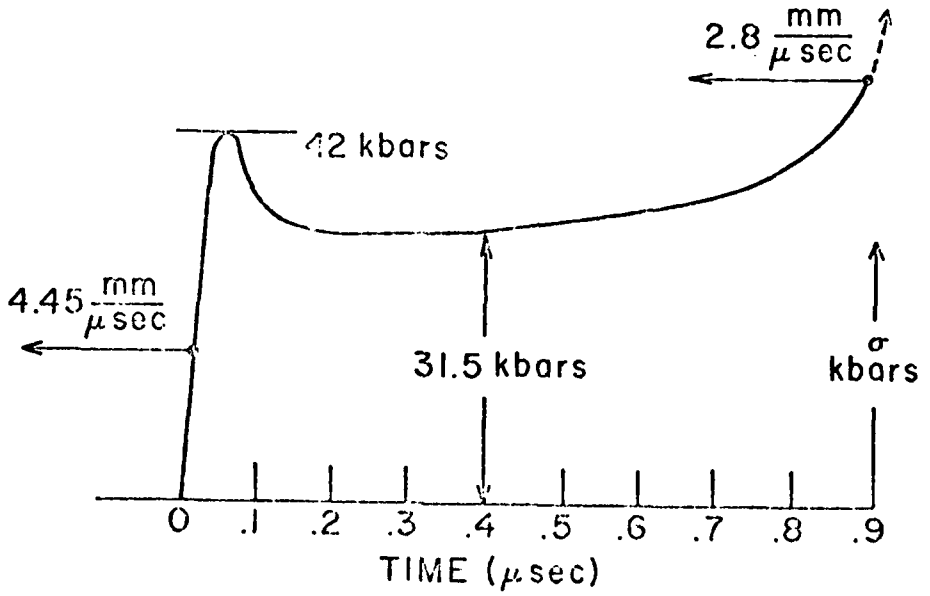

Fig. 1.2

Quartz gage records of shock transmitted through single crystal CdS. Propagation is along the "c" or "z" axis (Kennedy and Benedick, 1966).

Figure 1.2 can be better understood with the help of the diagram in Fig. 1.3. Suppose the line OAM represents the curve of elastic compression of CdS in uniaxial strain along the c-axis, and that, without phase transition,

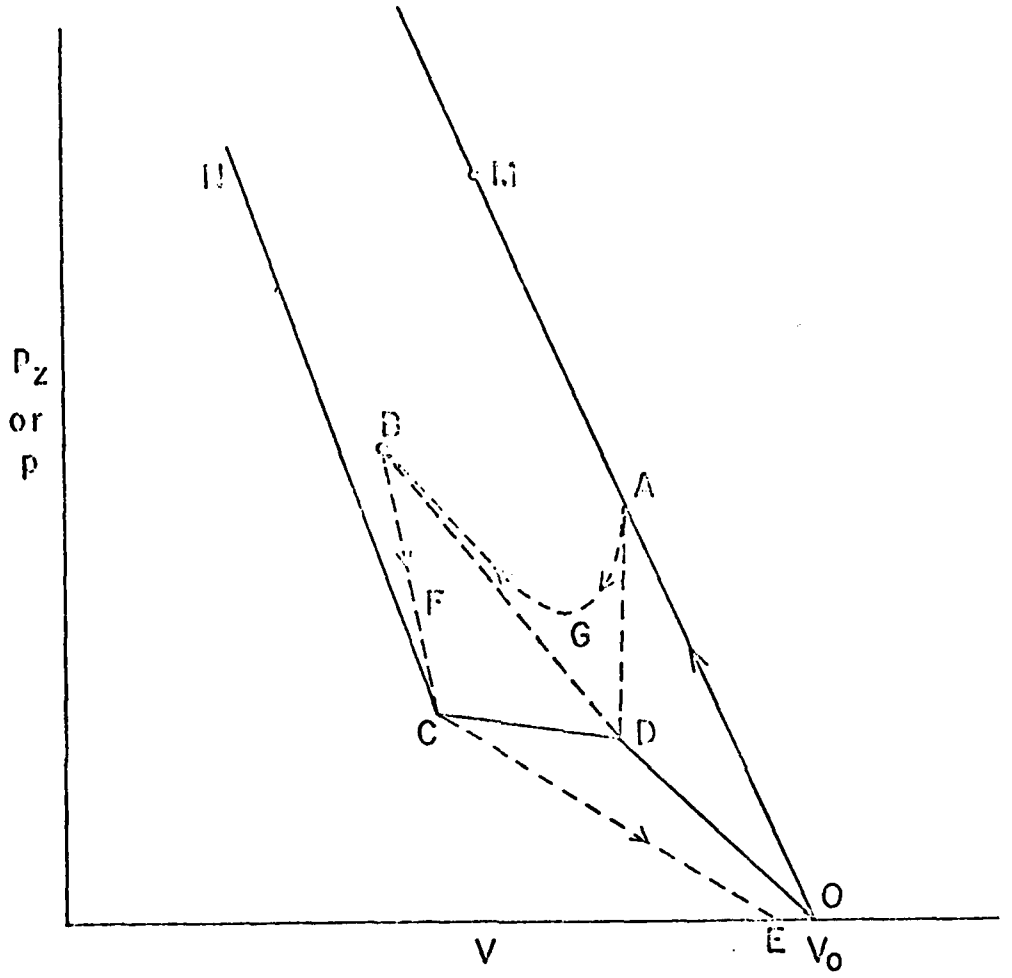

Fig. 1.3

Postulated pressure-volume
loci for the record of Fig. 1.2

dynamic failure would occur at the point M. Curve ODCN is the curve of hydrostatic compression of CdS and the segment DC represents the transition from phase I to phase II. Suppose further that in uniaxial elastic compression the phase transition is initiated at the same average pressure as under hydrostatic compression. Then transition from phase I to phase II is initiated at point A, the shear stress is immediately relieved and p_z starts to drop. This corresponds to the drop in stress immediately behind the first peak in Fig. 1.2.

The trajectory of the state point AGB is determined only by a detailed integration of the flow equations; but it is required to lie above the Rayleigh line connecting the stable transition point, D, with the final state, B. At point B the material is in phase II with some shear stress. On relief of the shock pressure, the state point will probably traverse some trajectory like BCE, ending up at zero p_z with some residual elastic strain.

This picture is very conjectural but still quite plausible in general. The actual details cannot now be stated. In support of the picture one can make the following calculation:

Let p_z be stress along the line OAM in Fig. 1.3 and p be the mean pressure on OD. Then for uniaxial strain along the Z or "C" direction,

$$p_z = C_{33}\epsilon_z$$
$$p_x = p_y = C_{13}\epsilon_z$$
$$p = (p_z + 2p_x)/3 , \quad \text{so}$$
$$p_z = 3p/(1 + 2C_{13}/C_{33})$$
$$= 1.363p \quad \text{for CdS.}$$

Taking the ratio of the first peak in Fig. 1.2 to the amplitude of the following valley as (p_z/p):

$$(p_z/p)_{meas} = 1.354 < 1.363$$

The difference between this and the calculated value corresponds to the vertical difference between G and D in Fig. 1.3, if the hypothesis of shear collapse is correct.

A second experiment from Sandia Laboratories, using InSb, shows a result similar to that for CdS (Kennedy and Benedick, 1965).

Rohde (1970) has reported measurements of the shock-induced reversal of martensite to austenite in an Fe-Ni-Cr alloy between room temperature and 400°C. Reversal pressure, p_z, decreases monotonically with temperature. At normal temperatures, a three wave structure exists: an elastic precursor followed by the phase transition wave, followed in turn by compression to the driver pressure. At the highest temperature the three wave structure appears, in a single observation, to be replaced by a two wave structure. Moreover, the extrapolated transition pressure lies below the Hugoniot Elastic Limit,* suggesting that the transition has caused τ to vanish or to become very small, and that the elastic wave is thereby preempted. No studies were made to determine whether or not clues to events lay in the microstructure of recovered specimens. There was no follow-up to this observation.

A recently completed set of experiments and calculations for a high velocity projectile shocking an iron plate show unambiguously that the 130 kbar phase transition in iron has marked influence on the nature and extent of structural damage to the plate (Bertholf et al., 1975). Numerical calculations which best agreed with the experiments assumed that stress vanished as phase transformation occurred.

1.2 Definition of the Gibbs Function

Classical thermodynamics is <u>essentially</u> macroscopic, i.e., it must work when the only knowledge of a system is external. When phase transitions occur within a volume under observation, it still must be true that the total increase in internal energy is equal to heat added plus work done on the system by external forces. If we assume changes to be irreversible, $dQ = TdS$. Then, always

---

* The Hugoniot Elastic Limit (HEL) is the amplitude of the elastic precursor in a shock wave whose final pressure is greater than the HEL. The amplitude of the HEL is $(1-\nu)/(1-2\nu)$ times the dynamic yield stress at the point of measurement.

$$dE = TdS + dW \tag{3}$$

By examining the interior of the system, we can infer other useful relations. For example, if the system is transforming from phase 1 to phase 2, the mass fraction of phase 2 is denoted x, temperature is common to both phases and surface energy is neglected, then specific volume, entropy and internal energy of the phase mixture are related to values in the two phases by the equations:

$$V = (1 - x)V_1 + xV_2 \tag{4a}$$

$$S = (1 - x)S_1 + xS_2 \tag{4b}$$

$$E = (1 - x)E_1 + xE_2 \tag{4c}$$

If the only stress acting is hydrostatic pressure, which is common to both phases, then

$$dW = -pdV \tag{5}$$

$$dE_1 = TdS_1 - pdV_1 \tag{6}$$

$$dE_2 = TdS_2 - pdV_2 \tag{7}$$

The above equations can be combined to give the relation:

$$\begin{aligned} dE &= (1 - x)dE_1 + xdE_2 + (E_2 - E_1)dx \\ &= TdS - PdV = (1 - x)(TdS_1 - pdV_1) + x(TdS_2 - pdV_2) + \\ &\quad + [T(S_2 - S_1) - p(V_2 - V_1)]dx \end{aligned} \tag{8}$$

It is evident that if Eq. (3) is to be satisfied, we must have

$$E_2 - E_1 = T(S_2 - S_1) - p(V_2 - V_1)$$

or

$$G_2 = E_2 - TS_2 + pV_2 = E_1 - TS_1 + pV_1 = G_1 \tag{9}$$

Eq. (9) can be taken as the definition of the Gibbs function for this situation; i.e. the Gibbs function is that function whose continuity insures the sanctity of Eq. (3).

To illustrate the possibility that shear stress can enter into the phase equilibrium condition, consider the following artificial situation wherein the second phase grows as a slab compressed between two slabs of phase one, with the system in a state of overall uniaxial strain, Fig. 1.4.

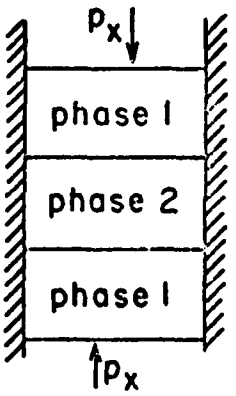

Fig. 1.4

Transformation in uniaxial strain

Since p_x is common to both phases, the argument leading to Eq. (9) can be repeated exactly, with p_x substituted for p. The equation of equilibrium now becomes

$$E_2 - TS_2 + p_xV_2 = E_1 - TS_1 + p_xV_1 \tag{10}$$

and the Gibbs function for this problem is

$$G = E - TS + p_xV \tag{11}$$

Equations (10) and (11) are formally identical to the hydrostatic Gibbs function except that p_x replaces p. The equilibrium point for the two phases may be significantly affected by differences in their physical meanings, however. Consider the compression process in detail, assuming that phase 1 is an elastic solid with finite yield point. From the uniaxial strain condition it follows that, for elastic compression,

$$p_x = 3p(1 - \nu)/(1 + \nu) \tag{12a}$$

$$= 3p/2 \qquad \text{for } \nu = 1/3 \tag{12b}$$

where ν = Poisson's ratio. Above the yield point, when $p_x - p_y = Y$,

$$p_x = \bar{p} + 2Y/3 \tag{13}$$

From Eq. (11),

$$dG_1 = -S_1 dT + V_1 dp_x \tag{14}$$

For dT = 0, this becomes, using Eqs. (12b) and (13), and assuming Y = constant,

$$dG_1 = 3V_1 dp/2 \qquad \text{below the yield point,} \tag{15a}$$

$$dG_1 = V_1 dp \qquad \text{above the yield point.} \tag{15b}$$

The stress state in phase 2 has less obvious constraints. It might grow in such a way that $p_x = p$, i.e., with no resolved shear stress. Then

$$dG_2 = V_2 dp \tag{16}$$

If it grows as an elastic system in uniaxial strain,

$$dG_2 = 3V_2 dp(1 - \nu)/(1 + \nu) \tag{17}$$

If yield should occur, above the yield point Eq. (16) again applies with a different value for Y. Some possible variations and their effects on $\bar{p}$ are shown in Fig. 1.5.

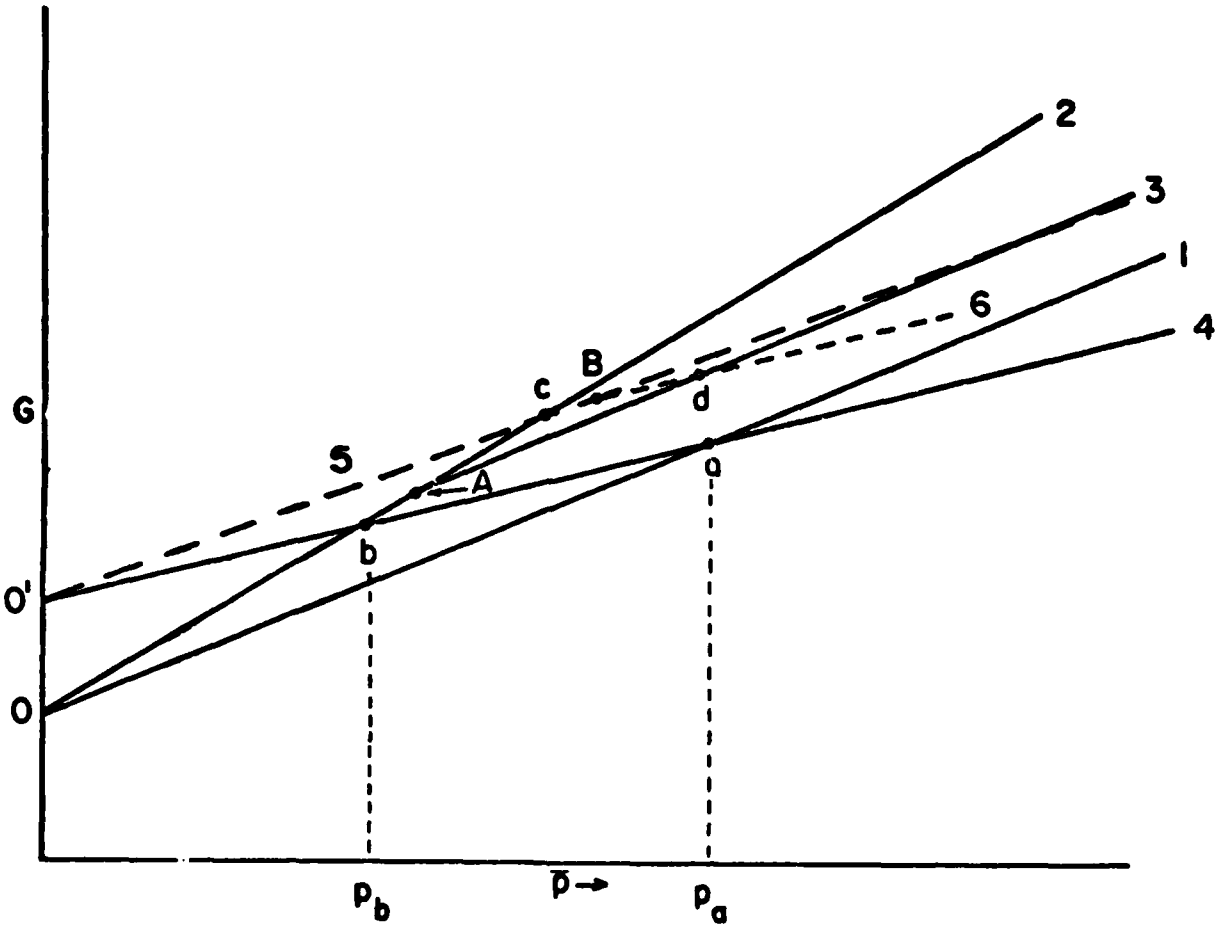

Fig. 1.5

Gibbs functions for uniaxial strain. The effects of changes in V_1 and V_2 have been ignored.

1. $dG_1 = V_1 dp$
2. $dG_1 = 3V_1 dp(1 - \nu)/(1 + \nu), \quad \nu = 1/3$
3. Same as 2 with yield at A.
4. $dG_2 = V_2 dp$
5. $dG_2 = 3V_2 dp(1 - \nu)/(1 + \nu), \quad \nu = 1/3$
6. Same as 5 with yield point at B.

Implications of the above conditions for the equilibrium point are shown in Fig. 1.5. Points a-d have the following meaning;

a. phase equilibrium for hydrostatic compression,

b. phase 1 is compressed elastically, phase 2 grows hydrostatically,

c. both phases are elastic in states of uniaxial strain,

d. both phases are in states of plastic flow.

The meanings of curves 1-4 are defined in the figure caption. If transitions were sensitive only to mean pressure, transition pressure would be p_a. If phase 1 were to remain elastic until transition occurs, and if phase 2 were hydrostatic, transition would occur at b and the locus of states would be Obc. The difference between p_a and p_b in such a case could be quite large. Other possibilities are described in the caption.

A more realistic situation, which illustrates the complexities of the problem, is that in which an isolated nucleus of phase-two material is growing in a matrix of phase 1. To be definite, let the system be in an overall state of uniaxial strain, as in Fig. 1.6.

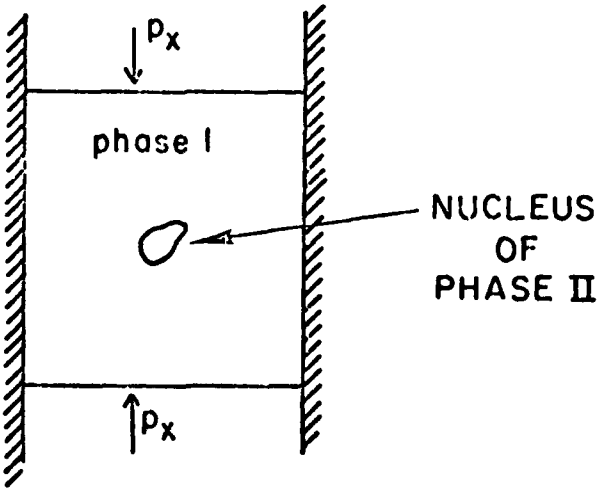

Fig. 1.6

Transformation in uniaxial strain

We still require that changes of internal energy of the entire system be given by

$$dE = TdS - p_x dV \ . \tag{18}$$

But now, since the stress state varies from point to point, we must solve a boundary-value problem to relate overall changes of E, S, V to changes in individual components, i.e., we seek more general expressions as substitutes for Eqs. (4).

First of all we define specific internal energies, e_j, specific volumes, v_j, and specific entropies, s_j, where j = 1 for phase 1 and 2 for phase 2. Then the total energy, etc. for each phase are:

$$E_j = \int_{V_j} (e_j/v_j)dV \tag{19}$$

$$S_j = \int_{V_j} (s_j/v_j)dV \tag{20}$$

$$V_j = \int_{V_j} dV \tag{21}$$

$$m_j = \int_{V_j} dV/v_j \tag{22}$$

$$x = M_2/(M_1 + M_2) \tag{23}$$

Note that dV/v_j is the mass of the volume dV under current conditions. If dV is taken to be the current value of the initial, untransformed, uncompressed volume in phase 1, we have by conservation of mass,

$$dV/v_j = dV^\circ/v_1^\circ = \text{constant} = dm \tag{22a}$$

Then Eqs. (19), (20) and (22) become

$$E_j = \int_{V_j} e_j dV^\circ/v_1^\circ \tag{19a}$$

$$S_j = \int_{V_j} s_j dV^\circ/v_1^\circ \tag{20a}$$

$$m_j = \int_{V_j} dV^\circ / v_1^\circ \tag{22a}$$

Now suppose that the boundary of phase 2 undergoes at each point a displacement $\delta\vec{u}$ and there is a simultaneous change in applied pressure, p_x. The resulting change in E_2 results from a change in e_2 integrated over the entire volume plus a change resulting from incorporation of new material within the boundary:

$$\delta E_2 = \int_{M_2} \delta e_2 dm + \int_{C_2} e_2 \delta m_2 \tag{24}$$

where $\delta m_2 = (\delta\vec{u}\cdot\vec{n})dA$ and the second integral is over the surface, C_2, enclosing M_2. Neither δe_2 nor e_2 may be constant over the region of integration, and we indicate this by a bar over the quantity. Then

$$\delta E_2 = M_2\overline{\delta e_2} + \bar{e}_2 \delta M_2 \tag{25}$$

where $\delta M_2 = \int_{C_2} \delta m_2$.

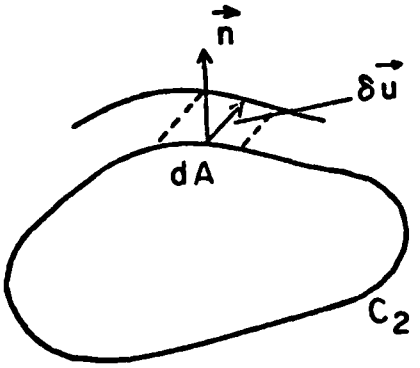

Fig. 1.7

Change in volume of phase 2.

Similarly, recalling that $\delta M_1 = -\delta M_2$,

$$\delta E_j = M_j \overline{\delta e_j} \pm \bar{e}_j \delta M_2 \tag{26}$$

$$\delta S_j = M_j \overline{\delta s_j} \pm \bar{s}_j \delta M_2 \tag{27}$$

$$\delta V_j = M_j \overline{\delta v_j} \pm \bar{v}_j \delta M_2 \tag{28}$$

with $\delta E = \delta E_1 + \delta E_2$, etc. and $M_2 = Mx$, $M_1 = M(1 - x)$, and T common to both phases, Eqs. (24)-(28) in Eq. (18) give

$$(1 - x)\,[\overline{\delta e_1} - T\overline{\delta s_1} + p_x\,\overline{\delta v_1}] + x[\,\overline{\delta e_2} - T\overline{\delta s_2} + p_x\,\overline{\delta v_2}]$$

$$+ \delta x[(\overline{e_2^s} - T\overline{s_2^s} + p_x\,\overline{v_2^s}) - (\overline{e_1^s} - T\overline{s_1^s} + p_x\,\overline{v_1^s})] = 0 \tag{29}$$

where superscripts "s" denote averages over the surface C_2.

According to Eq. (29), equilibrium is achieved and Eq. (18) is satisfied if $\bar{g}_1 = \bar{g}_2$, where

$$\bar{g}_j = \overline{e_j^s} - T\,\overline{s_j^s} + p_x\overline{v_j^s} \tag{30}$$

The pressure, p_x, is that applied to the pistons, Fig. 1.6, not the local value at the interface.

Equations (29) and (30) are deceptively simple. Values of e_j, s_j, v_j and their increments may vary dramatically throughout a volume containing an odd-shaped nucleus of material which is elastically dissimilar to the matrix. The quantity g in Eq. (30) looks like a Gibbs function, but it is not a point function; nor is it a state function in even an average sense, since p_x is the externally applied stress, not the local value.

Solutions required to evaluate Eq. (29) do not normally exist. One might reasonably expect to establish conditions for the onset of transition

by applying the above considerations to a spherical nucleus or to a lens, but any such simple relation must fail when the transition progresses far enough.

There is one other interesting case which can be treated in an elementary way. Suppose that the stress system consists of one component shear, τ, with corresponding strain γ. Suppose further that the total shear strain is

$$\gamma = \gamma_1(1 - x) + \gamma_2 x \ .$$

Then $dW = V\tau d\gamma$ and equilibrium exists when

$$E_1 - TS_1 - V\tau\gamma_1 = E_2 - TS_2 - V\tau\gamma_2 \ .$$

Coe (1970) has suggested that such a transition exists in the mineral enstatite.

Robin (1974) has pursued the problem of defining a Gibbs function in a crystalline lattice. He has found that such a function can be defined exactly for displacive transitions which maintain a plane boundary between the two phases, with orientation of the normal in certain directions, when strains produced by the displacement is small. This is interesting, but not particularly helpful in dealing with most solid-solid transitions.

Unless simplifying conditions can be found empirically, prospects for a simple theoretical description of a transforming solid do not appear bright. Unfortunately, these difficulties are not always recognized by material scientists and physicists dealing with solid-solid transitions. It was the intent of the present study to seek empirically some guidance in treating the effects of shear stress (distortion) on transformation. But the experiments turned out to be more difficult than anticipated.

II. Experimental Details

2.1 Experiment Design

The objective of these experiments was to determine whether or not collapse of stress deviators accompanies phase transitions in a solid. The first step toward this objective is based on the observations by Rohde (1970) that the amplitude of the elastic wave in shocked Fe/30%Ni* is independent of temperature and that the pressure of the α-γ or α-ε transition diminishes monotonically with temperatures apparently dropping below the elastic wave amplitude at 400°C. If transition pressure is less than elastic wave amplitude, the structure of the resulting shock wave is sensitive to collapse of the stress deviators. This can be seen with reference to Fig. 2.1. We see plotted there several curves for a material imagined to exist in either of two phases: OAB is the curve of uniaxial elastic compression of phase I; OD is the hydrostat of phase I; QJ and QH are the uniaxial elastostat and hydrostat, respectively, of phase II; ODGH is the equilibrium hydrostat, including phase transition from D to G. Curve OAC is that for quasistatic elastic-plastic compression of phase I with yield occurring at A.

Under steady conditions, with constant driving pressure, P_H, the shock OACH,J would be recorded, with E the elastic wave, P_I the wave corresponding to phase transition initiated at C and P_{II} the final wave. The end state of this transition is shown at H on the hydrostat of phase II, though it may include some shear stress. This three-wave structure would be expected after the wave has propagated a long way. The transition from A to C involves plastic deformation; the phase transition occurs between C and H,J.

---

* The symbols Fe/30Ni are used throughout to denote an alloy of iron and nickel containing 30% of the latter element in solution.

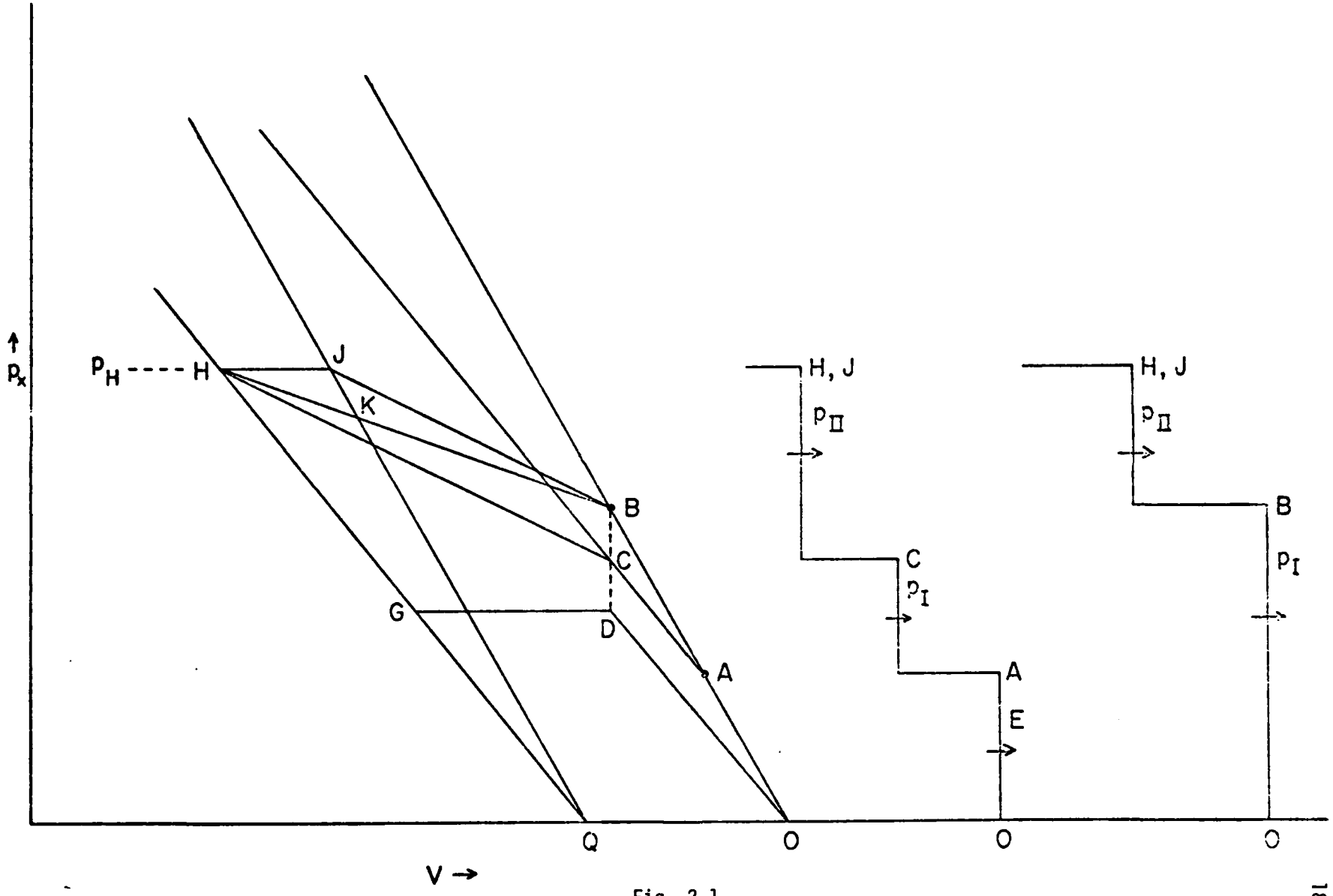

Fig. 2.1

Effects of phase transition on wave structure

If the Hugoniot elastic limit (point A) were to lie above B, where phase transition from the elastostat is assumed to occur, with final state H or J, a two-wave structure like OBH,J would be expected, unless failure occurred in the elastic state of phase II. OB is an elastic transition; BJ and BH represent the phase transition with or without shear stress in the second phase. If the transformation conserves shear stress and if elastic failure occurs above K, then transition B to H,J will break into two waves for some value of P_H. Retention of the two-wave structure for all P_H implies that shear is diminished in the transition process. "Second shock" experiments can be used to measure sound velocity in the final state and to distinguish between elastic and plastic states.

If elastic failure is relatively slow compared to phase transition, as is true in iron (Forbes, 1976), then for thin samples the Hugoniot Elastic Limit (HEL) may lie above B, while for thick specimens it lies below. This makes it possible to determine effects of transition on shear by varying specimen thickness and driving pressure, and to thus supplement variation of other physical parameters which alter relative amplitudes of HEL and transition. It has already been observed that this can be accomplished by variation of alloying materials (Blackburn et al., 1965; Stepakoff and Kaufmann, 1968; Fowler et al., 1961; Loree et al., 1966; Gust and Royce, 1970) in iron and by temperature variation (Rohde, 1970).

In light of these considerations, it was proposed to do a set of experiments with Fe/30Ni in which temperature is varied to bring transition pressure below the HEL. Sample thickness would also be varied, giving data on transition kinetics at the same time.

It was proposed to do plane shock experiments at temperatures such that transition pressure lies both above and below the HEL in order to determine

effects of transition on material failure. Three kinds of experiments were envisioned:

1. Dynamic experiments using quartz, sapphire, or manganin gage to monitor the wave structure in compression, thus determining the phase transition pressure and HEL, where both exist.
2. Recovery experiments in which transition pressure lies above and below the HEL in turn. Microstructure of specimens would be compared to determine differences in the nature and extent of microstructural damage in the two cases.
3. Transition kinetic experiments. These were to be of two kinds: (i) front surface impact experiments and (ii) shock transmission experiments. Front surface impact experiments are most easily done, and they lead to direct measurement of transition rate (Dandekar and Duvall, 1973). Transmission experiments display elastic and phase transition waves and the decay of both.

The WSU Shock Dynamics Facility was used for generation and measurement of the shock waves (Fowles et al., 1970).

2.2 Materials

If the proposed experiments were to be carried out, a phase-transforming material was required in which the relative amplitudes of elastic and transition waves could be varied. Loree et al.(1966) reported that addition of Ni to Fe reduced the $\alpha \rightarrow \varepsilon$ phase transition pressure, and they gave a value of approximately 82 kbar for the transition when Ni concentration was 30%. Rohde (1970) later suggested that the Fe/Ni/C/Mn/Si-70.45/28.4/0.5/0.45/0.2% alloy had a transition pressure less than 10 kbar at 390°C. Fowler et al. (1961) showed that an 18/8-Cr/Ni stainless steel had a transition pressure of 30 kbar at room temperature, but Gust and Royce (1970) in remeasuring a pure

18/8 alloy found a value of 79 kbar. Zukas and Levinson (1976) reported that a pure cast alloy of 18/8 Cr/Ni transformed readily and reversibly from α to γ phase under the influence of either temperature or pressure, and that the normal phase at room temperature is ferrite (α). They also reported that commercial 18/8 stainless (321) could be transformed to α-phase at liquid nitrogen temperature by cold working.

It appeared then that Fe/30Ni was the most promising candidate material, but that 18/8 - Cr/Ni was worth examining. Billets of pure Fe/30Ni and 18/8-Cr/Ni were ordered from Carpenter Steel Co., and some effort was made to convert commercial 304 stainless to α-phase for preliminary experiments. This effort was unsuccessful; no amount of work at liquid nitrogen temperature served to convert a significant fraction to α.

Experiments at room temperature showed that neither 18/8-Cr/Ni nor 70/30-Fe/Ni had a well-defined elastic precursor and that transition pressure for the Fe/Cr/Ni was only slightly less than that for the Fe/Ni. So experimentation was continued with the Fe/Ni alone because of extensive data on its properties which were already available.

Carpenter Steel Co. provided an analysis of the starting materials for each casting and Dr. Donald Mikkola of Michigan Technological University very kindly arranged for analysis of the materials after they had been cast and forged. Results of both analyses on two different castings are given in Table I. The A-Casting was received first in the as-cast form. Preliminary experiments produced a very slowly rising precursor, and microscopic examination suggested that small particles of Ni were distributed throughout the bar. It was returned for hot forging and the resulting material was denoted AF. After this treatment there was a fractured region in the center of the bar and what appeared to be microscopic pores distributed throughout.

The second casting--the B-Casting--was cast and hot-forged before delivery. It was of better quality mechanically and contained about the same amount of carbon as the first casting. The carbon content did not appear to interfere with transformation to the α-phase.

TABLE I

Impurities in 70/30-Fe/Ni provided by Carpenter Steel Co.

	A-Casting		B-Casting	
	Carpenter analysis	Mikkola analysis*	Carpenter analysis	Mikkola analysis
Ni	30.86%	29.7%	29.85%	29.5%
C	.002	.0165	.005	.0163, .0191
Mn	<.01	Traces of Ti, Al, Si, P	<.01	Traces of Ti, Al, Si, P
Si	.03		<.01	
P	<.005		<.005	
S	.004		.002	
Cr	.01		.01	
Mo	<.01		.01	

Sample A contained a center crack and microscopic voids.
Sample B was not porous.
A was returned for hot forging after initial examination indicated precipitated Ni. B was hot forged immediately after casting.

* D. F. Mikkola, Metallurgy Department, Michigan Technological University.

2.21 Transformation Properties of Fe/30Ni

This alloy can exist as either austenite (fcc) or martensite (bcc) at room temperature and up to about 350°C. If Ni content is much less than this, austenite is not retained at room temperature. If Ni content is much greater

than 30%, the bcc phase cannot be obtained by cooling. General features of the transformation properties are shown in Fig. 2.2.

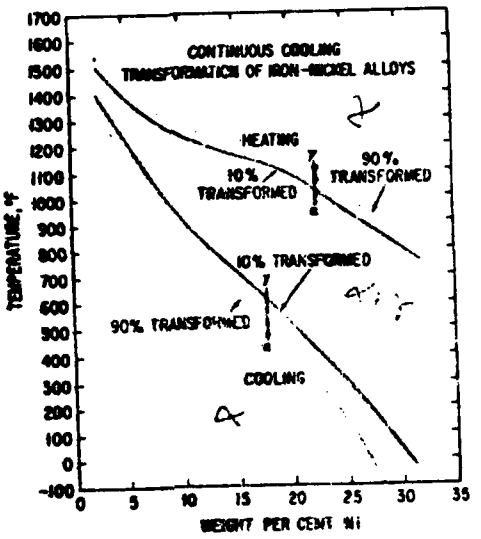

Fig. 2.2

General features of temperature-induced α-γ transitions in Fe/Ni alloys (Decker, 1960)

Details of transformation appear to depend on the investigator, on the exact amount of nickel, which may differ by a percent or more from the nominal value, and on the presence or absence of other impurities.

Machlin and Cohen (1951) published the results of a study made with single crystals of Fe/30Ni partially transformed to martensite at -40°C. By measuring the orientation of martensite habit planes with respect to the fcc matrix they were able to show that the transformation is in accord with the Bowles (1951) double-strain analysis for martensitic transformations, provided one additional assumption is made in the Bowles analysis: The second direction of atom motion lies along the only remaining close-packed direction in the unrotated close-packed plane after the first strain.

Patel and Cohen (1953) measured the effects of uniaxial tension and compression on Ms for Fe/20Ni/.5C rods and the effect of hydrostatic pressure on Ms for Fe/30Ni. They found Ms to be raised by application of uniaxial stress and depressed by hydrostatic pressure, and they found both results to be in accord with the thermodynamic concept of a driving force ($-\Delta F$) which depends on stored elastic energy as well as temperature.

Otte (1957) examined the effects of low temperatures and cold work on laboratory-prepared Fe/Ni alloys containing 28, 32, or 40% Ni. The 28% Ni, undeformed, was examined only at room temperature. X-ray revealed the presence of γ and α phases and suggested ϵ, but this was tentative. The 32% Ni showed only γ with some extra lines appearing after deformation at -196°C. He concluded that faulting in these alloys was minimal and there was little evidence for work-hardening.

Breedis (1964) found the martensite start temperature of a pure Fe/33.1%Ni alloy to be -100°C. He found the martensitic transformation occurring spontaneously and "in audible bursts."

Papadakis and Reed (1961) reported that quenching of Fe/30Ni in dry ice and acetone produced 40% martensite and quenching in liquid N_2 produced 90%.

Graham et al. (1967) measured the shock Hugoniot curves of a commercial alloy, "Temperature Compensator 30," manufactured by the Carpenter Steel Co. It contained 29.5%Ni/0.5%Mn/0.2%Si/0.1%C. Samples were austenitized at 650°C for two hours, furnace-cooled to 100°C, and air-cooled to room temperature. They were held in liquid N_2 for 168 hours to produce 95% martensite. Bulk modulus of the fcc phase increases rapidly with pressure at about 25 kbar, and they inferred from this that the material was undergoing a pressure-induced Curie transition from ferromagnetic to paramagnetic. The α-phase had constant bulk modulus to 50 kbar.

Samples of Fe/30%Ni/.026%C and Fe/28%Ni/0.1%C were rolled to 200 μ-thick sheets, austenitized at 750°C for one hour and quenched to room temperature (Bowden and Kelly, 1967). The 30% Ni was cooled to -55°C, the 28% Ni to -90°C, in order to produce 60% α-martensite in both alloys. Two-inch square specimens were shock-loaded to 100, 160 and 200 kbar, respectively, and examined for changes in structure.

Before shock loadings, specimens showed a structure of twinned and partially twinned α-martensite plates in a matrix of retained austenite with a small amount of lath martensite having no internal twinning. Transmission electron microscopy of shocked specimens showed that some or all of the α-martensite had transformed to the γ-phase, which was retained. Transformation was complete for the 160 and 200 kbar specimens. Only a small amount of the α-martensite was transformed at 100 kbar, and discrete plates of γ-martensite were found within the α-martensite. It was inferred from habit plane orientation that the γ-plane is produced by two distinct mechanisms. The normal mechanism produces austenite with the same orientation as the parent austenite. This is not true for the second mechanism, austenite in this case was assumed to have been produced by inhomogeneous shear on $(101)_\alpha$ planes.

Rohde et al. (1968) measured the amount of austenite produced by shocking bcc martensite of "Temperature Compensator 30" to various pressures. Their samples were from the same lot as that used by Graham et al. (1967), and the heat treatment was the same. The initial and final concentrations of austenite are shown in the following table, taken from their work:

Shock pressure (kbar)	0	18	50	70	100
% Austenite	26.2 ± 1	33.5 ± 1	37.5 ± 1	44.4 ± 1	50.0 ± 1

They also inferred that at 100 kbar an fcc martensite had been produced. It's interesting to note that Bowden and Kelly (1967) found little transformation

to austenite for a 100 kbar shock into 60% martensite; whereas Rohde et al. found 25% conversion for 74% initial martensite. The difference might involve pressure duration, the effect of varying initial α concentration, or differences in impurity content of their materials. It has been found that carbon and manganese in steel tend to stabilize austenite, and the "Temperature Compensator 30" contains both.

Rohde and Graham (1969) measured the effect of hydrostatic pressure on the "austenite start temperature," A_s, i.e. the temperature at which the α-phase begins to convert to γ as temperature is increased at a uniform rate. In their experiments the heating rate was 3 or 4°C/min. They found $dA_s(P)/dP$ to be non-linear with values -4.5°C/kbar from 0 to 10 kbars and -3.5°C/kbar from 0 to 20 kbars. They also found $A_s(0) = 380°C$. In contrast, Patel and Cohen (1953) found the pressure dependence of the martensite start temperature of Fe/30Ni to be $dM_s/dP = -8.8°C/kbar$ with $M_s(0) = -20°C$. Rohde and Graham inferred from their thermodynamic analysis that the rate of transformation from α to γ will increase with increasing pressure. The material used by Rohde and Graham was "Temperature Compensator 30" described by Graham et al. (1967). Their results were fitted equally well by thermodynamics of isothermal or isentropic transformation. They concluded that for thermodynamic purposes it is adequate to use the gross work done on the sample in computing the driving force. Stress and strain fields for a single plate are not required.

Pope and Edwards (1973) measured the effects of hydrostatic pressure and cold work on the martensite-austenite reversal in Fe/30.3Ni. They found $dA_s/dP < -30°C/kbar$, $0 < P < 2.3$ kbar, dA_s/dP positive and decreasing with P for $2.3 < P < 6$ kbar, and $dA_s/dP \simeq -1.9°C/kbar$ for $6 < P < 20$ kbar. The graph of A_s vs. P has a sharp cusp at 2.3 kbar, and decreasing negative curvature thereafter. Thirty percent cold work increases A_s from 390 to 440°C

at atmospheric pressure and from 320° to 310°C at 20 kbars. Cold work shifts the cusp to slightly higher pressures. The authors explain their results by the proposal that hydrostatic compression of the mixed phase containing martensite platelets, which differ elastically from austenite, causes shear stresses at the α-γ interfaces. This contributes to the driving force, causing $-dA_s/dP$ to be initially large. When yield occurs, this contribution vanishes and A_s returns to a more normal dependence on pressure.

Since we were planning shots at high temperature in order to achieve transition from bcc to fcc at very low pressure, we would necessarily be working near the austenite start temperature. We determined that our experimental procedure required specimens to be at temperature for as much as half an hour before being shocked. We measured the amount of austenite produced in transformed specimens on being held at various temperatures for 30 minutes. The results are given in Fig. 2.3. There is no detectable change at 300°C, <5% at 350° and about 13% at 400°C. If A_s is defined as the point of intersection of extended straight portions of the curve, as shown in the figure, $A_s \simeq 395$°C. This same procedure was used by Rohde and Graham (1969), who

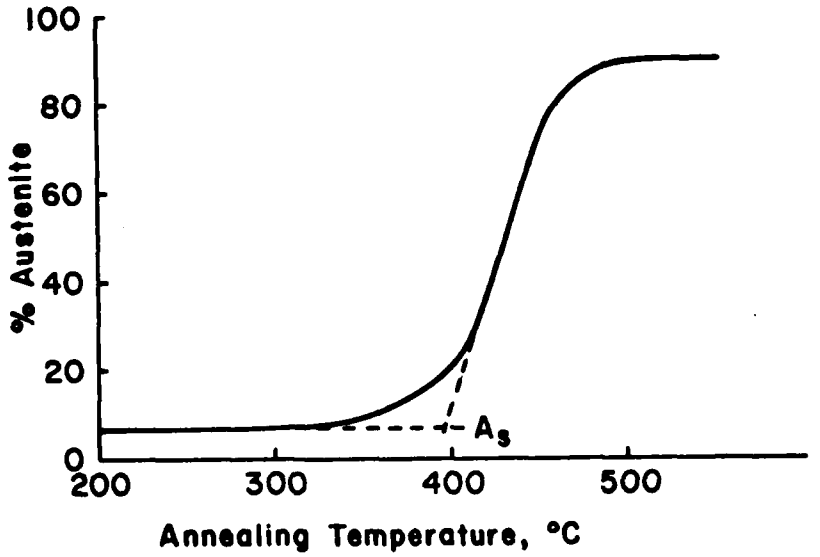

Fig. 2.3 Effects of annealing on bcc martensite in Fe/30Ni. Specimen from casting B transformed by cycling in liquid N_2 and annealed for 30 minutes at various temperatures.

found $A_s \approx 380°C$ for "Temperature Compensator 30" alloy. This difference tends to confirm the belief that addition of carbon and manganese stabilizes the austenitic phase when it's added to Fe/30Ni. This point will arise again in discussion of the Hugoniot for the α-phase (Section 2.22).

In most of the work discussed above the fraction of austenite existing in a sample was determined by x-ray diffraction methods (Miller, 1964; Hilliard and Cahn, 1961; Averbach et al., 1950; Lindgren, 1965). Other methods used involved inductance changes (Rohde and Graham, 1969; Pope and Edwards, 1973) or resistance changes (Patel and Cohen, 1953).

An extensive review of martensitic transformations at low temperatures containing over 600 references is given by Reed and Breedis (1965).

2.22 Mechanical Properties

Papadakis and Reed (1961) determined the effect of α-phase content on relative contributions of Rayleigh scattering and elastic hysteresis to ultrasonic attenuation. Their material was described only as Fe/30Ni. In the course of their experiments they measured longitudinal and transverse wave velocities for various conditions of the specimens. Their Table I is reproduced here, with wave velocities converted from inches per microsec to mm/μsec.

"Microstructure and ultrasonic velocity during transformation. Frequency = 7 Mc; velocity in mm/μsec.

Treatment	% Austenite	Longitudinal Wave Velocity	Transverse Wave Velocity
Cold rolled	100	--	--
Equiaxed[a]	100	--	--
Dry ice and acetone quench	60	4.95 ± .05	2.64 ± .05
Liquid nitrogen quench	9-11	5.23 ± .05	2.51 ± .05
Tempered[b]	10-15	4.95 ± .05	2.59 ± .05
Recrystallized[c]	100	4.65 ± .05	--

a. Heated to 1500°F (815°C) b. 300°F(149°C) for 2 hours
c. At 1500°F (815°C) for 2 hours".

It is hard to evaluate these measurements. If "Tempered" values are excluded, the three remaining longitudinal velocities fit a straight line quite well:

$$C_L (mm/\mu sec) = 4.67 \pm .0064 \times (\%\alpha)$$

With the tempered value again omitted, the straight line through the remaining pair of transverse values is

$$C_S = 2.74 - .0026 \times (\%\alpha)$$

Micrographs in the paper show that tempering at 149°C for three hours has smoothed the appearance of the material. But annealing experiments done here at various temperatures show that a half hour anneal produces no change in α-content below 350°C, Fig. 2.3. Yet the longitudinal velocity given in the above table falls on the straight line if α-content is 44% instead of 87.5%. And the transverse value corresponds to 58% on the transverse line, Fig. 2.4.

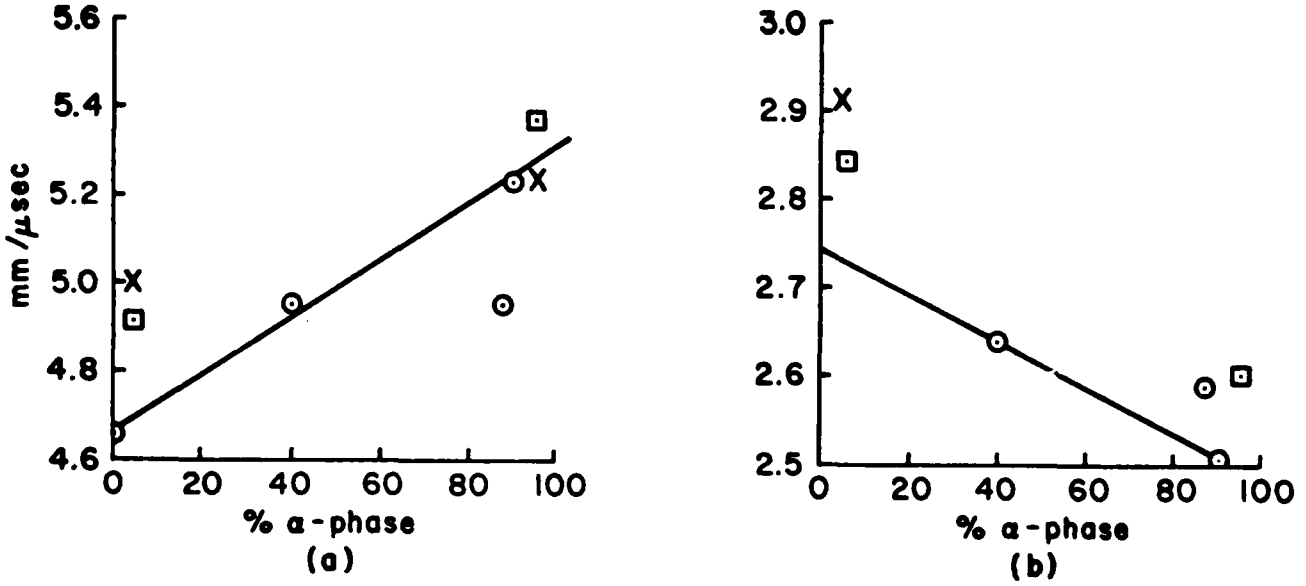

Fig. 2.4 Effect of martensite (α) content on sound velocity.
a) Longitudinal, $C_L = 4.67 + .0064 \times (\%\alpha)$
b) Shear, $C_S = 2.74 - .0026 \times (\%\alpha)$

⊙ Papadakis and Reed (1961)
× Graham et al. (1967)
⊡ Present work

If the difference is split and we suppose the true α-content was 51%, each translated value is in reasonable accord with the straight lines given above.

Graham et al. (1967) reported longitudinal and shear velocities for austenite and longitudinal velocities for martensite. They are plotted in Fig. 2.4. They also inferred compressibilities from their shock wave measurements. Elastic constants from ultrasonic and shock measurements are given in Table II.

TABLE II

Elastic Constants and Densities of Fe/30Ni

	%α	Density	λ+2μ kilobars	μ kilobars	k kilobars	Reference
	0	8.195[a]	1772	--	--	Papadakis and Reed (1961)
(20)	5	8.158	2048	696	1120	Graham et al. (1967)
	5	8.186±.005	1978	661	1097	Present work
	40	8.121[a]	1990	566	1235	Papadakis and Reed (1961)
	87.5	8.034[a]	1968	539	1249	Papadakis and Reed (1961)
	90	8.029[a]	2196	506	1521	Papadakis and Reed (1961)
(88)	95	8.032	2016	--		Graham et al. (1967)
	95	8.020±.003	2315	541	1594	Present work
	5	8.158	Hugoniot modulus:		1163	Graham et al. (1967)
	95	8.032	Hugoniot modulus:		1667	Graham et al. (1967)

a. Papadakis and Reed do not quote densities; these values are calculated from the equation $\rho = 8.195 - .1844\ (\%\alpha/100)$. Constants in this equation are obtained from values obtained in our work.

The first eight rows are from ultrasonic measurements at atmospheric pressure. The last two are from shock measurements below 50 kbar.

Average density for the pure γ-phase of Fe/30Ni determined from x-ray diffraction angles is

$$\rho_\gamma = 8.167 \pm .013 \text{ g/cc}$$

For the α-phase it is

$$\rho_\alpha = 8.000 \pm .013 \text{ g/cc}$$

If we assume the austenitic phase to be 95% γ and the martenistic phase to be 95% α, the mean densities are

$$\rho \text{ (austenite)} = 8.159 \text{ g/cc}$$

$$\rho \text{ (martensite)} = 8.008 \text{ g/cc}$$

These compare with measured densities for our samples

$$\rho \text{ (austenite)} = 8.186 \pm .005 \text{ g/cc}$$

$$\rho \text{ (martensite)} = 8.020 \pm .003 \text{ g/cc}$$

The room temperature P-V Hugoniot curves for Fe/30Ni are shown in Fig. 2.5. The upper points on the α-phase curve by Loree et al. (1966) and by Rohde (1970) are transition states at which the α-γ phase transformation occurs. The difference between them may result from small differences in composition of their materials. Rohde used "Carpenter temperature compensator 30" which contains about 0.5% C, 0.45% Mn and 0.2% Si. He reported a smaller initial concentration of α-phase than we found in our samples. He also found approximately 18% conversion of α to γ at pressures below the transition pressure, which we did not find; this has the effect of softening the Hugoniot, indicated by the dotted line in the figure. Transition pressures we measured for cast material A averaged 79 kbar, including one anomalously low value. The cast and forged material, AF, later found to include micropores, had a mean transition pressure of 74 kbar; the lower value is presumed to result from the porosity. We assumed the point of Loree et al. (1966) to be valid for our work, and the α-phase Hugoniot was taken to be the solid curve in Fig. 2.5. In estimating impact pressures (Table VI), the high pressure state was assumed to be in the γ-phase, taken from the LRL Compendium (Van Thiel et al., 1977, Vol. 3, p. 662) and Graham et al. (1967). The locus of final states used in choosing experimental parameters was faired into the γ-phase data

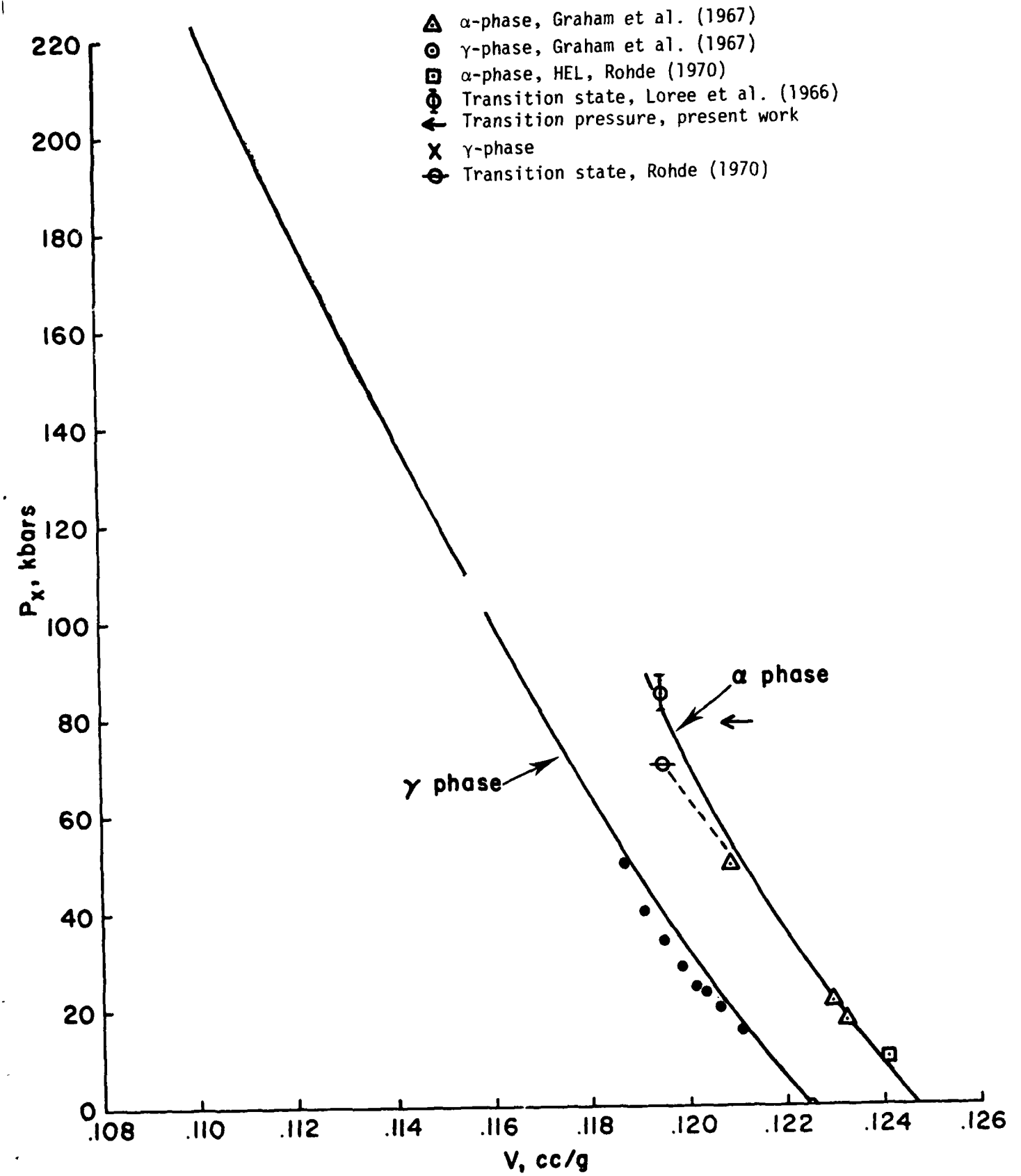

Fig. 2.5 Hugoniot Curves for Fe/30Ni

of Graham et al. from the high pressure points given in the Compendium. This procedure is in error in principle, but it was adequate for experimental design purposes. In estimating the impact pressures produced in experiments at different temperatures, no account was taken of the thermal offset of the Hugoniot. For both these reasons, the impact pressures given in Table VI are estimates only. They may be in error by a few kilobars.

The Hugoniot curve in the pressure-particle velocity (P_x,U_p) plane was estimated as follows. The expected transition pressure was chosen and the corresponding (P_x^T,V^T) pair was chosen from the α-phase values of Table III, say P_x^T = 40 kbar, V^T = .12178 cc/g. The particle velocity corresponding to this pair is $U_p^I = [P_x^T(V_o - V^T)]^{1/2}$ = .0108 cm/μsec. The second shock Hugoniot is then given by

$$U_p^{II} = U_p^I + [(P_x^F - P_x^T)(V^T - V^F)]^{1/2}$$

where P_x is in megabars and U_p is in cm/μsec. P_x^F and V^F pairs were chosen from γ-phase values in Table III. The resulting curves are like those shown in Fig. 2.6.

TABLE III

α-phase		γ-phase	
Pressure P_x, kbar	Volume V, cc/g	Pressure P_x kbar	Volume V, cc/g
0	.12469	50	.11883
10	.12393	60	.11820
20	.12318	70	.11762
30	.12246	80	.11706
40	.12178	90	.11651
50	.12110	100	.11598
60	.12058	110	.11549
70	.12004	120	.11495
80	.11960	130	.11443
82.5	.11940	140	.11393

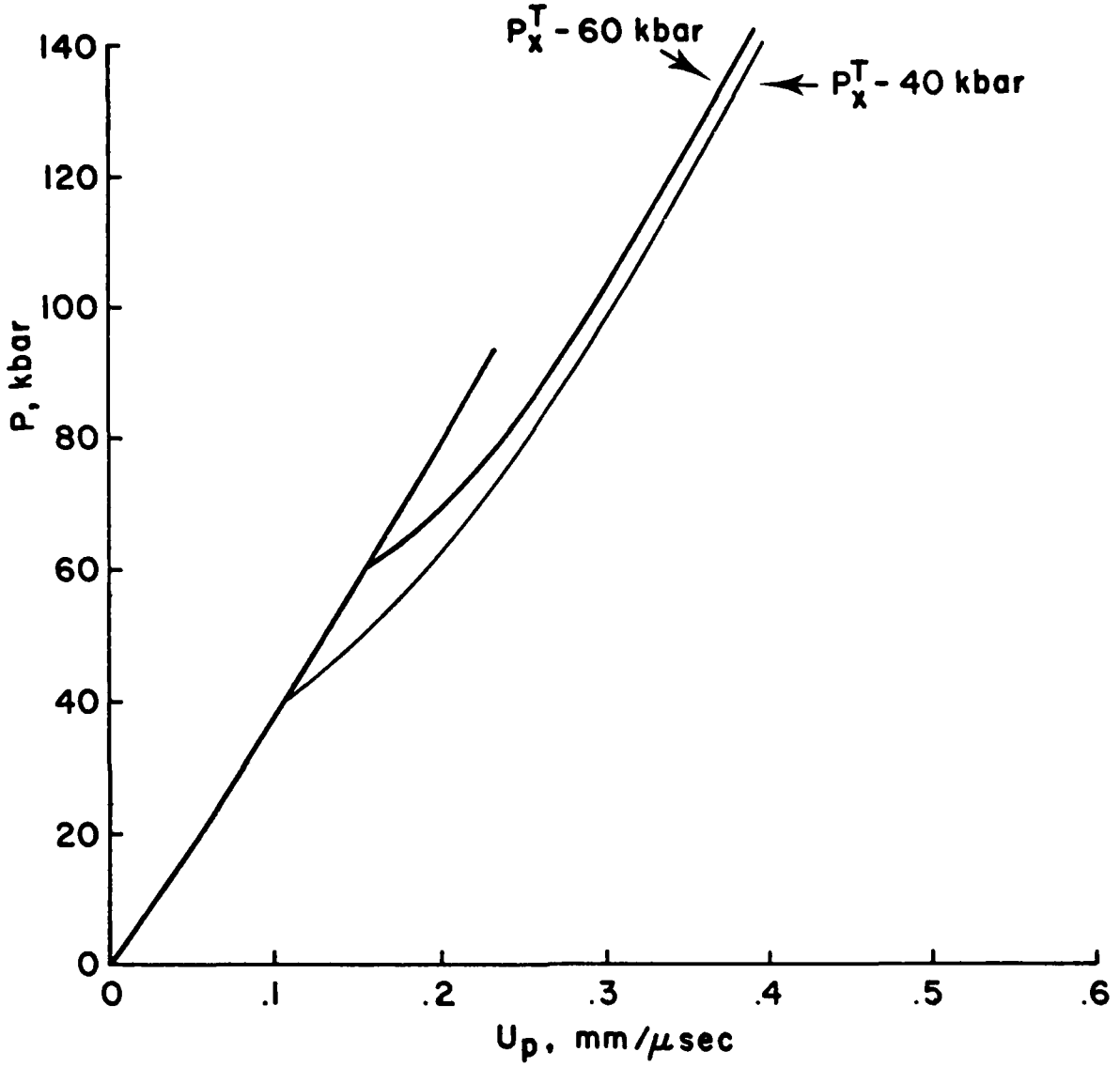

Fig. 2.6 Hugoniot curves of Fe/30Ni used for estimating impact pressures. This was constructed by assuming that the state behind the second shock lies on the γ-phase Hugoniot and that $U_p = U_p^{II} = [P_T(V_o - V_T)]^{\frac{1}{2}} + [(P_F - P_T)(V_T - V_F)]^{\frac{1}{2}}$

2.3 Procedures

2.31 Material Preparation

Samples were in the form of disks approximately 1.25 inches diameter. They were heated for 2 hours in a metal bag at 650°C and water-quenched. They were converted to the α-phase by alternately quenching to liquid nitrogen

temperature and warming to room temperature. Five cycles of this treatment were enough to produce about 95% α-phase. Relative concentrations of γ-and α-phases were measured by x-ray diffraction using the method of Miller (1964). Micrographs of specimens before and after cycling in liquid N_2 are shown in Plate I (Part B). The mean concentration cf γ-phase concentrations after cycling, was 6 ± 2%. Densities were measured using a displacement method, but were not accurate enough to determine phase concentrations.

After transformation to the α-phase, samples were lapped flat and parallel on both faces, then polished. Samples to be heated had a hole drilled near one edge of the back surface (away from the impact surface) and tapped for a thermocouple. Room temperature shots were potted in epoxy in a target ring with the impact face perpendicular to the axis of the gun barrel. A quartz gage was epoxied to the back face of the specimen. Samples to be heated were mounted in the furnace described in Section 2.33.

2.32 Tilt Manipulator

Clear differentiation of multiple wave arrivals in a shock experiment requires that tilt of the flat face of the projectile with respect to the flat face of the target at impact be small. Tilt angles greater than 10^{-3} radians are generally unacceptable. Target and impactor surfaces can readily be aligned at room temperature before the target chamber is evacuated, and this alignment is maintained reasonably well during evacuation and up to the time of impact.

When targets are heated or cooled, following evacuation of the target chamber, the alignment normally changes as temperature changes because of differential expansion or contraction of various parts of the system. Experience has shown that alignment at the final temperature before the target chamber is closed and evacuated does not insure continued alignment after evacuation. Some means of adjusting the orientation of the target was therefore required

for experiments with heated targets.

A water cooled target holder was constructed which was supported by three worm-gear driven jack screws of the design shown in Fig. 2.7. The

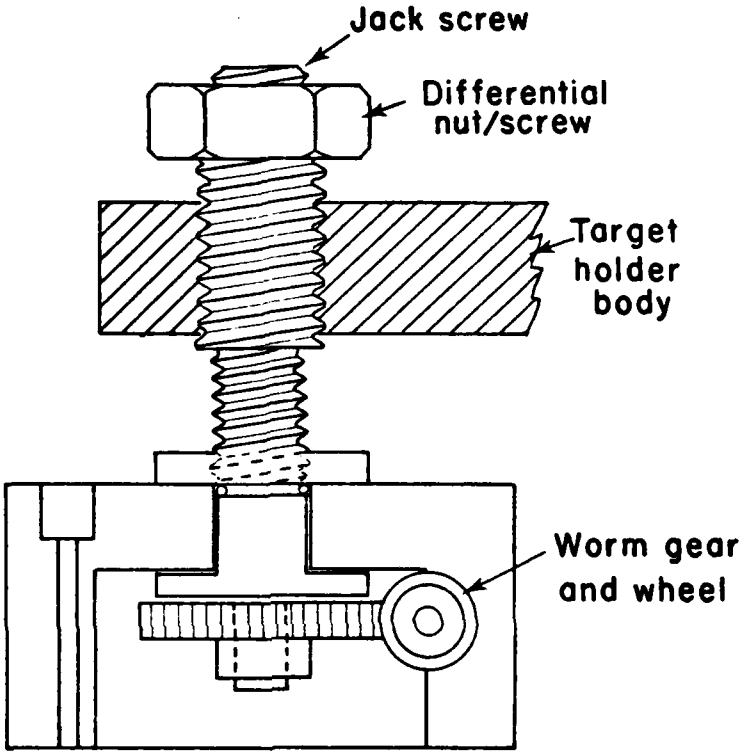

Fig. 2.7

One of three jack screws used for support and alignment of the water-cooled target holder

jack screws were connected to the target plate by differential screws to facilitate initial alignment of the target from inside the tank. The jack screw worms were driven by a gear reduction system which also formed the vacuum seals for the adjustment rods which extended through the vacuum chamber and the muzzle room wall. Initial target alignment is made in the usual way by dial indicator and breech plug. The back surface of the target was lapped and polished to a mirror finish of sufficient optical quality that an auto-collimator could be used to detect any change in the alignment of

this surface. After initial mechanical alignment the auto-collimator was aligned on the mirror surface through a system of mirrors. The jack screws were adjusted during heating so as to preserve the original alignment by following any motion through the telescope. Some experiments were done using a reflected laser beam with satisfactory results.

It was found that some late modifications of the target design made only slight or no adjustment of the target necessary. Some of these modifications include annealing the aluminum heater block and providing lava feet for the contact between the heater block and the target holder plate.

2.33 Hot Target Design

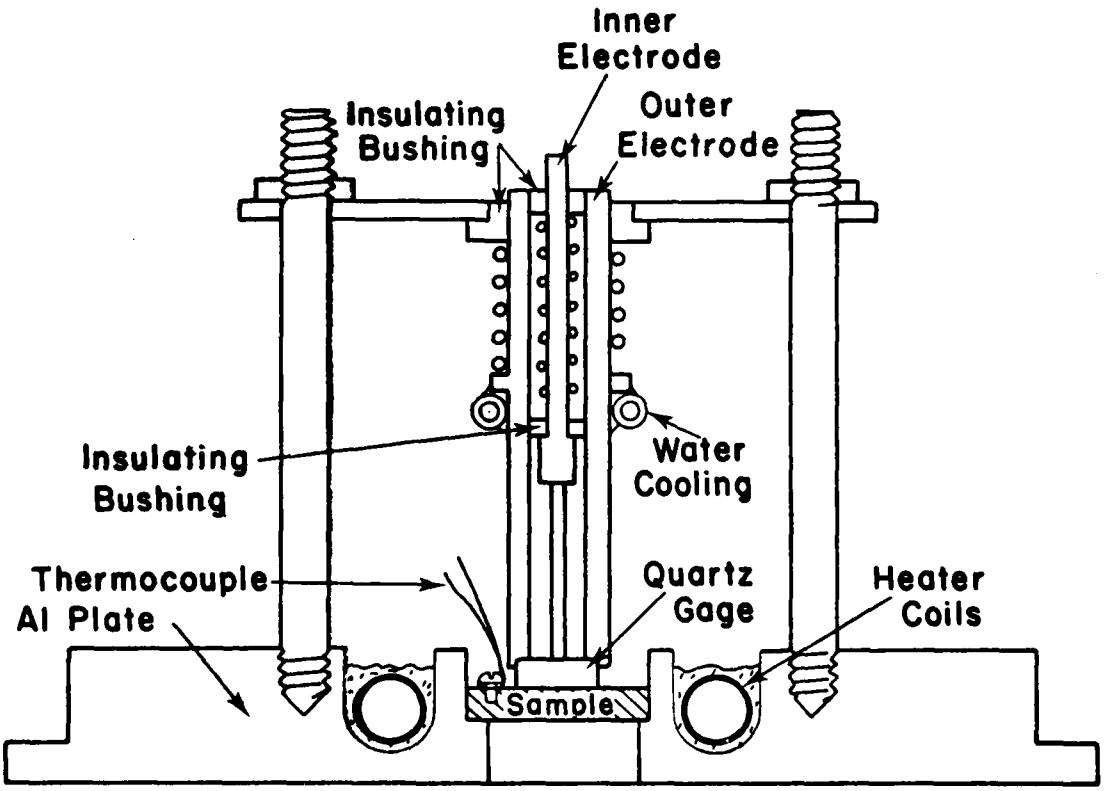

Fig. 2.8 Hot Target Assembly, Mark I

Two types of target assemblies were used for the series of high temperature experiments. The first target shown in Fig. 2.8 consists of an aluminum block into which a 125 watt nichrome heater is potted with high temperature cement. The target is held in a stepped hole by the spring-loaded contact assembly. The target was impacted by a flyer which extended far enough beyond the projectile to contact the target before the projectile touched the heater block.

The contact assembly was designed to provide a 50 Ω electrical environment down to the quartz gage. Contact with the quartz gage was by spring loading on the inner and outer electrodes. Water cooling was found necessary so as not to anneal the springs or melt the soldered connections to the contact assembly.

Results from this contact arrangement were erratic. The data seem to indicate variable contact resistance at the quartz gage. The second target assembly remedied this trouble by using silver-filled epoxy to attach the contacts. It was found that these joints also needed to be spring loaded. This assembly is shown in Fig. 2.9.

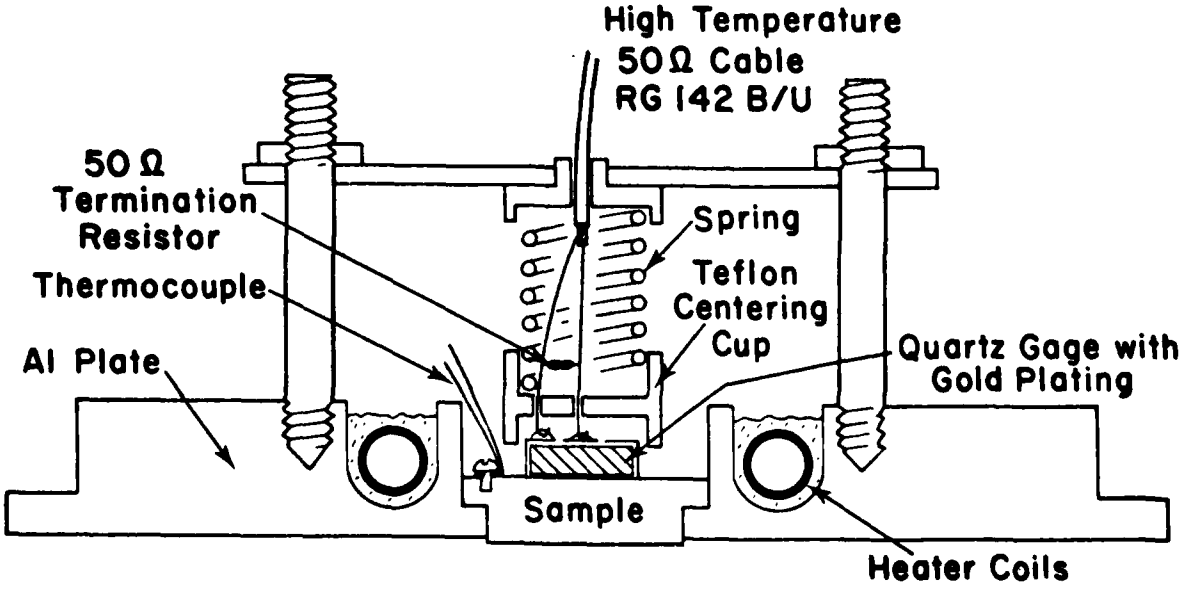

Fig. 2.9 Hot Target Assembly, Mark II

2.34 Shot Procedure

For room temperature shots the target ring containing the sample was mounted in the target ring holder and aligned parallel to the face of a gage plug in the end of the gun barrel. Cables from tilt pins, trigger pins, and the quartz gage were led to oscilloscopes outside the muzzle room. The quartz gage output was to be recorded on two separate oscilloscopes, and these were calibrated for current input from the quartz gage. The target chamber was closed and evacuated, the gun breech pumped to the desired pressure, oscilloscope sweep triggers set and the gun was fired. The resulting records were read on a microscope with a moving stage and digitized output, and the results were converted to pressure vs. time diagrams, to be described in Section III.

For hot shots the procedure was the same. In addition it was necessary to monitor the temperature and alignment of the target and to adjust alignment, as required, using the tilt manipulator described in Section 2.32.

III. Experimental Results

3.1 Precursor Amplitudes

Elastic precursor waves were discernible on 7 records with initial temperatures ranging from 20°C to 225°C. There was no detectable dependence of amplitude on temperature. In some cases they were barely discernible, in others they were well-defined. They seemed to be better defined at elevated temperatures than at room temperature. Cold working of samples had no effect on precursor detectability. Rise times in the precursor were always large. The mean amplitude was

9.05 ± 1.01 kbar.

TABLE IV

Precursor amplitudes for Fe/30Ni

Shot #	thickness, cm	P_x^e, kbar	Quality	T_o
78007	.6543	7.6	poor	20°C
78010	.1895	9.5	fair	20°C
78021	.4942	9.85	good	20°C
78023	.1587	8.0	poor	20°C
78041	.7239	8.9	good	81°C
78047	.7467	10.5	good	170°C
78049	.7470	9.0	good	225°C
		$\overline{P_x^e} = 9.05 \pm 1.01$ kbar		

3.2 Effect of temperature and pressure on recovered martensite

The amount of austenite in samples recovered after shocking is shown in Table V and in Fig. 3.1. There is no apparent dependence on impact pressure. If the 120°C, 140 kbar point is omitted, shocking produces no significant change in austenite for $T_o \leq 200$°C. For higher temperatures the amount of recovered austenite increases with T_o. This suggests that materials shocked at the lower temperatures go into a different phase from those shocked at high temperatures. The transition which occurs in Fe/30Ni is derived from the 130 kbar α-ε transition in iron. It is not unreasonable that the ε phase should still be accessible by compression at this composition. In that case it may well be that the large fraction of recovered γ in the 120°C, 140 kbar shot arises because, at that large pressure, the material is carried through the ε-γ boundary and into the γ-phase.

TABLE V

Austenite in recovered samples for different initial temperatures and impact pressures

% γ in Recovered Sample	Initial Temperature, °C	Impact Pressure, kbar
12	20	85
5	20	85
9	80	80
65	120	140
10	200	65
45	275	70
40	275	80
89	400	85
87	400	85
86	390	90

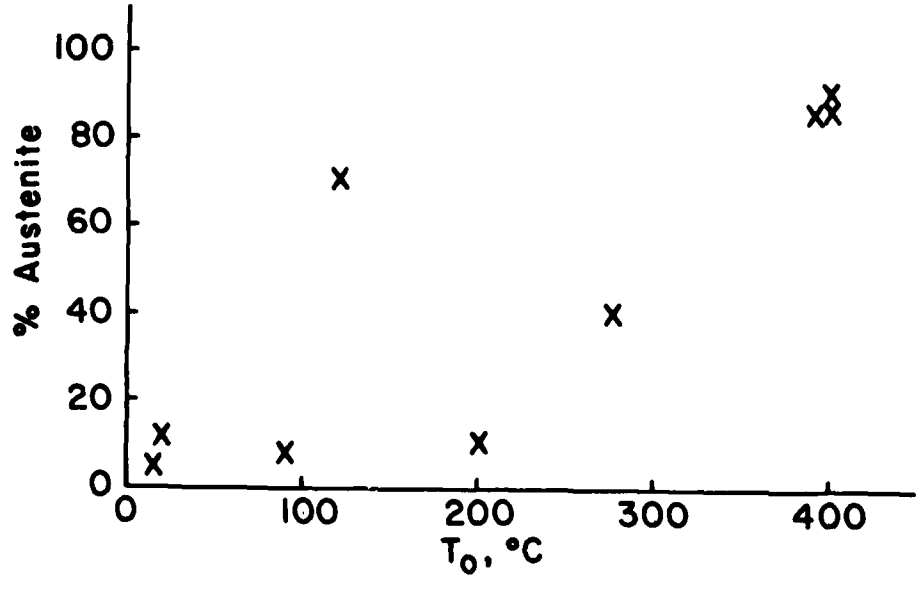

Fig. 3.1

Retained austenite vs. initial temperature

3.3 Effect of initial temperature on transition pressure

Transition pressure vs. initial temperature is plotted in Fig. 3.2, along with similar measurements reported by Rohde (1970). Except for two points at T_o = 200°C and 225°C, the points correspond fairly well with Rohde's measurements, being a little higher at the lower temperatures.

These measurements and those of Rohde were made with quartz gages affixed to the rear faces of the specimens. The quartz gage is at or near its upper limit of reliability for pressures the order of 70 or 80 kilobars in the Fe/Ni; some of the differences between our data and Rohde's may be due to that. It was suggested earlier that the alloy Rohde used may convert more readily to austenite than our material, a circumstance which could lead to differences of the kind shown in Fig. 3.2 at the lower temperatures. It is surprising, however, that the differences appear to vanish at the higher temperatures.

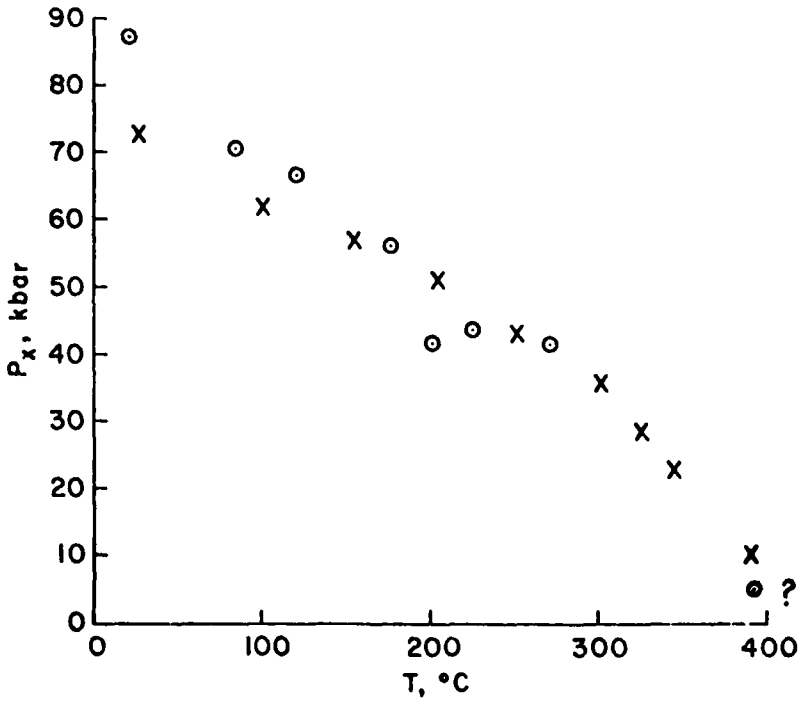

Fig. 3.2

Transition pressure, P_x, vs. initial temperature for Fe/30Ni

× Rohde (1970)

⊙ Present Measurements

Rise times in the oscilloscope records at elevated temperatures were very long. One of the records, reduced to shock pressure and time, is shown in Fig. 3.3. The first wave is the elastic precursor, the second is the transition wave. Impact pressure was estimated at 55 kbar, and the final wave is off the scale to the right. Reasons for the long rise times are not apparent. Tilt of the target was monitored before the shot, and there was no evidence of warping of the target.

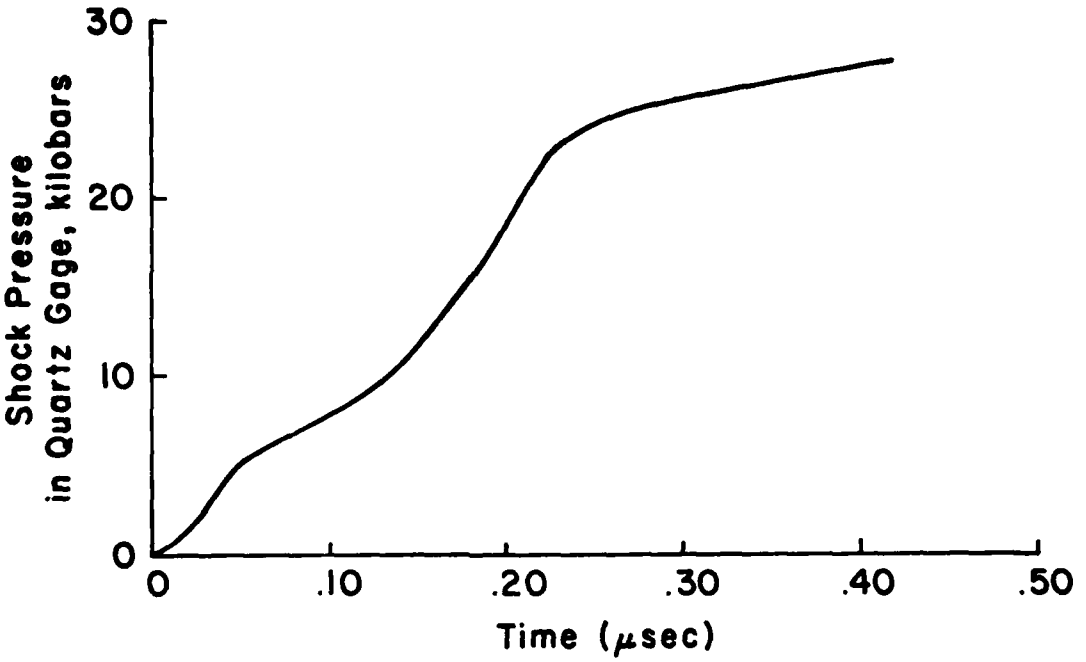

Fig. 3.3 Pressure time history for shot no. 79-049. Fe/30Ni, material B. T_o = 225°C. Impact pressure ≈ 55 kbars. Elastic precursor 9 kbars, phase transition at 43 kbars.

Initial temperatures and transition pressures are given in Table VI.

TABLE VI

Variation of Transition Pressure with Initial Temperature

Shot No.	Material	Sample thickness mm	Temperature at impact °C	Projectile velocity mm/μsec	Impactor	Impact Pressure calc., kbar	P_1 Transition Wave Pressure kbar	P_1 Pressure in Quartz kbar[a]
78-007	A	6.543	20	.560	Cu	105	72	41 s
78-010	A	1.895	20	.47	Cu	85	81	46.0s
78-011	A	1.811	20	.516	Cu	95	81	45.6s
78-013	A	1.189	20	.505	Cu	92	83	47 s
78-018	AF	1.098	20	.510	Fe/30Ni	90	78	44.4s
78-021	AF	4.942	20	.505	Fe/30Ni	90	71	40.0s
79-023	AF	1.587	20	.508	Fe/30Ni	90	77	43.6s
79-027	AF	8.5	392	.528	Fe/30Ni	87	6[b]	3.8ss
79-039	B	5.39	20	.465	Fe/30Ni	90	78	44 ss
79-041	B	7.239	81	.464	Fe/30Ni	78	71	41 ss
79-044	B	7.465	200	.421	Fe/30Ni	65	42	23.7ss
79-046	B	7.465	120	.785	Fe/30Ni	142	67	37.8ss
79-047	B	7.467	170	.525	Fe/30Ni	87	56	31.8ss
79-049	B	7.470	225	.343	Fe/30Ni	55	43	24.6ss
79-052	B	6.689	275	.488	Fe/30Ni	76	41	23.5ss
78-019	Fe/Cr/Ni-74/18/8	1.050	20	.510	Fe/Cr/Ni-74/18/8	90	72	40.9s
78-020		5.507	20	.509		90	74	42.0s

a. The letter "s" indicates that the gage was used in the shunted mode. "ss" indicates the shorted mode.

b. Transition wave not positively identified. See text.

There were three shots with initial temperature 400°C. Only one of them yielded gage records which could be read with any confidence. Oscilloscopes triggered late and only part of the initial wave was recorded, Fig. 3.4.

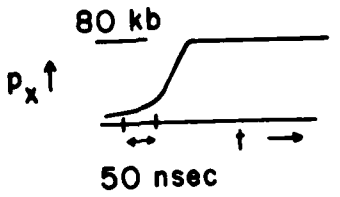

Fig. 3.4 Oscilloscope record from shot no. 79-027. Fe/30Ni, material B. Initial temperature 390°C. Impact pressure ~ 85 kbar (calc.).

The amplitude of the ramp at the time of its first appearance is approximately 5.5 kbars, which is little more than half the precursor amplitude recorded for initial temperatures from 20°C to 225°C. It's not possible that this precursor is the elastic wave; it's too far separated from the final wave, and there is no transition (PI) wave. It's unlikely that the sample has converted to austenite before being shocked. Fig. 2.3 suggests that it was at least 80% martensite when shocked. It seems most likely that it is the transition (PI) wave and that it did indeed collapse the stress deviators and thereby pre-empt the elastic precursor.

The ramp amplitude quoted above is plotted with a question mark beside it in Fig. 3.2. It falls below Rohde's estimate at 390°C.

Sample thicknesses were varied from 1 mm to 8 mm and there was no indication that either elastic precursor amplitude or transition pressure depends on sample thickness to a marked extent.

IV. A Computational Model for Shear Relief during Phase Transformation

When the experiments described in the previous section are extended to sufficiently high temperatures, we expect to find some interference between yield and phase transition, depending on the extent to which stress deviators are collapsed by the transition. As an aid to interpretation of the experiments, a one-dimensional wave propagation program is required which incorporates time-dependent yield, time-dependent phase transformation, and an adjustable model of stress deviator collapse. In the course of the wave calculations, time will be incremented and new values of stress, strain and energy will be calculated for each new time. Section 4.1 describes computational procedures for time-dependent yield in general terms for arbitrary strain increments. Section 4.2 deals more explicitly with uniaxial strain and 1-D wave propagation for time-dependent yield. A program for time-dependent phase transition is described in Section 4.3. Some numerical results are given in Section 4.4.

4.1 Yield Calculations for Arbitrary Strain Increments.

The increment in internal energy corresponding to a set of strain increments $(d\varepsilon_{ij})$ is

$$dU = \sigma_{ij} d\varepsilon_{ij} ,$$

where σ and ε are stress and strain, respectively, both positive in tension. Let

$$S_{ij} = \sigma_{ij} + \delta_{ij} p$$

$$de_{ij} = d\varepsilon_{ij} - \delta_{ij} d\theta/3$$

$$d\theta = d\varepsilon_{ii} .$$

Then

$$dU = (S_{ij} - p\delta_{ij})(de_{ij} + \frac{d\theta}{3} \delta_{ij})$$

$$= S_{ij}de_{ij} + \frac{d\theta}{3} S_{ij}\delta_{ij} - p\delta_{ij}de_{ij} - \frac{p}{3} d\theta\delta_{ij}\delta_{ij}$$

$$S_{ij}\delta_{ij} \equiv 0 ; \qquad \delta_{ij}de_{ij} \equiv 0 ; \qquad \delta_{ij}\delta_{ij} \equiv 3$$

$$dU = pd\theta + S_{ij}de_{ij}$$

= increment in work of compression + increment in work of deformation

For elastic strains

$$de_{ij} = \frac{dS_{ij}}{2\mu}$$

where μ is shear modulus. For μ = constant, the energy of deformation is

$$U_o = \frac{1}{2\mu} \int_0^{S_{ij}} S_{ij}dS_{ij} = \frac{S_{ij}S_{ij}}{4\mu} \equiv \frac{J_2}{2\mu}$$

where J_2 is the second invariant of the stress-deviator tensor: $J_2 = S_{ij}S_{ij}/2$.

The von Mises criterion for yield amounts to a statement that elastic failure occurs when the energy of deformation exceeds a critical value which depends on material. Its exact form is

$$J_2 = S_{ij}S_{ij}/2 \leq Y^2/3 \qquad (1)$$

where Y is yield stress in simple tension for thin bars. If the inequality applies, the material state is elastic. The equality is satisfied when the material state lies on the yield surface. In principal axis coordinates,

$$J_2 = \frac{1}{2}(S_x^2 + S_y^2 + S_z^2) . \qquad (2)$$

When the equality in (1) applies, Eqs. (1) and (2) define a sphere in (S_x, S_y, S_z) space, centered at the origin:

$$S_x^2 + S_y^2 + S_z^2 = R^2 = 2Y^2/3 \qquad (3)$$

The trace of the deviators vanishes, as a consequence of their definition:

$$S_x + S_y + S_z = 0 \tag{4}$$

Equation (4) defines a plane in deviator space. Its intersection with the sphere of Eq. (3) determines a circle, centered at the origin, lying in a plane whose normal makes equal angles with the three principal axes. When the combined stress state of the material lies within this circle, the material is behaving elastically; when it is on or outside the circle (as it may be for time-dependent yield), it is behaving plastically.

Elimination of S_z between Eqs. (2) and (4) gives*

$$J_2 = S_x^2 + S_y^2 + S_x S_y \tag{5}$$

Since J_2 is invariant, it is independent of the coordinates in which it is computed. A given value of J_2 represents a sphere in (S_x,S_y,S_z) space. S_x,S_y,S_z are constrained to lie on a plane in that space by condition (4). The origin of the plane and the origin of the sphere are common, so a point (S_x,S_y,S_z) which lies in the plane also lies on a radius of the sphere, and that radius lies entirely in the plane. This property is critical to the computational procedure described below. It leads to the

* With $J_2 = Y^2/3$, Eq. (5) describes an ellipse, this being the projection of the aforementioned circle on the (S_x,S_y) plane. The equation of the ellipse can be expressed in normal form by rotating the S_x,S_y axes 45°:

$$S_x' = \frac{1}{\sqrt{2}}(S_x + S_y) \quad , \quad S_y' = \frac{1}{\sqrt{2}}(-S_x + S_y)$$

$$\frac{(S_x')^2}{a^2} + \frac{(S_y')^2}{b^2} = 1$$

$$a^2 = \frac{2Y^2}{9} \quad , \quad b^2 = \frac{2Y^2}{3}$$

conclusion that if each deviator is reduced in the same ratio, the resulting point withdraws toward the center of the sphere along a single radius.

The philosophy of computation is this: Compute S_x, S_y from the total strain, assuming that total strain is elastic. Compute J_2 from these deviators and compare with $Y^2/3$. If $J_2 \leq Y^2/3$, the deviators are correct as calculated. If $J_2 > Y^2/3$, the deviators are too large and must be reduced. If plastic flow is time independent, the deviators are reduced by the factor $\alpha = Y/\sqrt{3J_2}$. This brings them back to the yield surface along their radius. If plastic flow is time dependent with relaxation time τ, the amount by which the radius vector from the origin to the calculated values of S_x, S_y, S_z exceeds the radius of the yield sphere is reduced by the ratio $\Delta t/\tau$, where Δt is the time step. This excess radius is

$$\Delta r = \sqrt{2J_2} - Y\sqrt{2/3} .$$

If $\Delta t/\tau \geq 1$, the flow is treated as time independent.

More explicitly, the computation is made as follows: Assuming the computed change in strain to be elastic, S_x, S_y are computed. Denote these values by S_x', S_y'. From Eq. (5), the corresponding invariant is computed. Denote it by J_2'. The comparison of J_2' with $Y^2/3$ is made. If J_2' exceeds $Y^2/3$, and if time-independent plasticity is assumed, the state point is reduced radially to the yield surface by setting

$$S_x = \frac{Y}{\sqrt{3J_2'}} S_x' \quad : \quad S_y = \frac{Y}{\sqrt{3J_2'}} S_y' \tag{6}$$

Then

$$J_2 = \frac{Y^2}{3J_2'} J_2' = \frac{Y^2}{3}$$

For time dependent plasticity, the deviator J_2' corresponds to a point in (S_x, S_y, S_z) space at a distance from the origin $r' = \sqrt{2J_2'}$. The radius of the equilibrium surface is $r_{eq} = Y\sqrt{2/3}$. Assume $r' > r_{eq}$. The calculated change in

strain took place in a time Δt, and we suppose that the state point has relaxed along its radius vector toward the yield surface by an amount

$$(r'-r_{eq})\,\frac{\Delta t}{\tau} \quad ,$$

where τ is the current value of relaxation time for the stress-relaxing process.

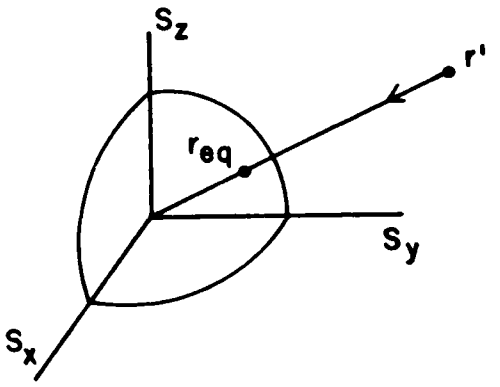

Figure 4.1: Time-dependent stress relaxation.

Then the new radius, at the end of the time step Δt, is

$$r = r' - (r'-r_{eq})\,\frac{\Delta t}{\tau} \quad , \tag{7}$$

provided $\Delta t/\tau < 1$. If $\Delta t/\tau \geq 1$, r is set equal to r_{eq}.

Individual deviators have components

$$S_x' = \ell r', \quad S_y' = mr', \quad S_z' = nr' \tag{7a}$$

where ℓ,m,n are direction cosines of the radius vector r'. The final values of S_x, S_y, S_z are therefore

$$S_x = \frac{r}{r'} S_x' \quad , \quad S_y = \frac{r}{r'} S_y' \quad , \quad S_z = \frac{r}{r'} S_z' \tag{8}$$

where

$$r/r' = 1 - (1-Y/\sqrt{3J_2'})(\Delta t/\tau). \tag{9}$$

This process is related to the governing differential equation of relaxation in the following way. There exists a relaxation law for S_j of the form

$$\frac{dS_j}{dt} = 2\mu \frac{de_j}{dt} - g(\underline{\sigma},T, \ldots) \tag{10}$$

where g has been assumed to be the same for all deviators. Equation (10) can also

be written in the form

$$\frac{dS_j}{dt} = 2\mu \frac{de_j}{dt} - \frac{(S_j - S_j^{eq})}{\tau} = \frac{dS'_j}{dt} - \frac{(S_j - S_j^{eq})}{\tau} \tag{11}$$

where $\tau = (S_j - S_j^{eq})/g(\underline{\varepsilon}, T, \ldots)$ and S_j^{eq} is the point at which the radius vector (S'_x, S'_y, S'_z) intercepts the yield surface. The S_j are constrained to lie on this radius, so Eq. (7a) applies. Then if Eq. (11) is divided by ℓ, m, or n, depending on the value of j, it becomes

$$\frac{dr}{dt} = \frac{dr'}{dt} - \frac{r - r_{eq}}{\tau} . \tag{12}$$

In finite difference form this becomes

$$\Delta r = \Delta r' - (r - r_{eq}) \frac{\Delta t}{\tau} . \tag{13}$$

Since

$$r = r^\circ + \Delta r$$

$$r' = r^\circ + \Delta r',$$

where

$$r^\circ = [S_x(t), S_y(t), S_z(t)]$$

$$r' = [S'_x(t+\Delta t), S'_y(t+\Delta t), S'_z(t+\Delta t)]$$

$$r = [S_x(t+\Delta t), S_y(t+\Delta t), S_z(t+\Delta t)],$$

Eq. (13) can also be written as

$$r = r' - (r - r_{eq}) \frac{\Delta t}{\tau} \tag{14}$$

If $\Delta t/\tau \ll 1$, $(r - r_{eq})$ can be replaced by $(r' - r_{eq})$ with only second order error; then Eq. (14) is identical to Eq. (7). A somewhat better approximation is obtained if Eq. (14) is used as it stands. Then

$$\frac{r}{r'} = \frac{1 + (r_{eq}\Delta t/r'\tau)}{1 + (\Delta t/\tau)} . \tag{15}$$

Equation (15) then replaces Eq. (9).

The assumption that the relaxation function, g, in Eq. (10) is the same for all deviators and the corresponding assumption that the state point approaches the equilibrium yield surface along a radius are consequences of the Associated Flow Rule of formal plasticity theory; this can be seen as follows. During the time increment, Δt, there have occurred increments, Δe_j, in the strain deviators. These increments are partly elastic and partly plastic. If they are small we can write

$$\Delta e_j = \Delta e^e + \Delta e^p \tag{16}$$

The deviators, S'_j, are calculated as if the strain increments, Δe_j, were totally elastic:

$$\Delta S'_j = 2\mu \Delta e_j \ . \tag{17}$$

They are then caused to relax to values closer to or on the equilibrium surface. Since the final change is proportional to the elastic strain increment

$$\Delta S_j = 2\mu \Delta e^e_j \ , \tag{18}$$

the reduction in stress deviat from S'_j to S_j is proportional to the plastic strain increment:

$$\delta S_j = S'_j - S_j = S^\circ_j + \Delta S'_j - S^\circ_j - \Delta S_j = 2\mu \Delta e^p_j \tag{19}$$

But by the Associated Flow Rule (Eq. (2) of the Appendix),

$$\Delta e^p_j = d\lambda \frac{\partial f}{\partial S_j} \tag{20}$$

where $f(p,S_j) = 0$ is the equation of the yield surface. Then

$$\delta S_j = 2\mu d\lambda \frac{\partial f}{\partial S_j} \ . \tag{21}$$

But $\mu d\lambda$ is the same for all j and the $\partial f/\partial S_j$ are components of $\nabla_{\underset{\sim}{S}} f$, a vector normal to the yield surface, $f = 0$; therefore, the motion of the stress point is normal to

the surface. Since it lies in the plane $S_x + S_y + S_z = 0$, the vector δS_j lies also along a radius. If the yield surface is not a sphere, the coherence of Eq. (10) and the computing procedure described by Eqs. (1)-(9) may no longer exist. Then more explicit information about material behavior is required before a suitable model for computation can be developed.

Equation (21) may appear to be in conflict with Eq. (2) of the Appendix. It is not. The increments in stress which appear in Eq. (2) of the Appendix are constrained to satisy the yield condition that all stress states lie on or within the yield surface. The stress increments in Eq. (21) are derived from independent considerations, and it follows from the Associated Flow Rule that these increments are normal to the yield surface.

4.2 Uniaxial Strain.

The problem can be cast in a much simpler form for uniaxial strain. Only one stress and one strain component need be considered and the equilibrium circle reduces to two points which move in the pressure volume plane as density changes.

In Figure 4.2, OBC is a curve of uniaxial compression from V_o. B is a yield point and BD is the equilibrium curve of uniaxial compression in the plastic regime. OA is the hydrostat through V_o. DEF is a curve of uniaxial expansion. If the loading-unloading path is OBDEF, the segment DE is one of elastic expansion.

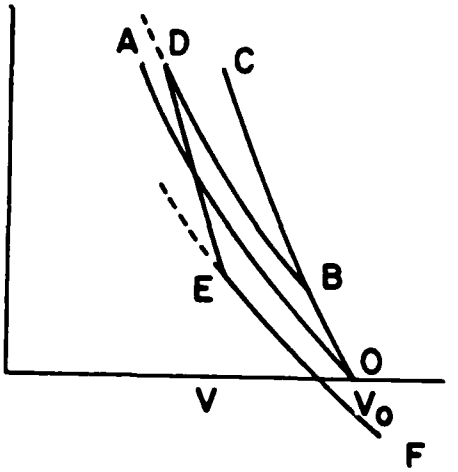

Figure 4.2: Uniaxial strain.

If it is assumed that the stresses are supported by elastic strains, then one can proceed as follows. Assume that curves BD and EF are given and $p_x = -\sigma_x$, etc.:

$$\text{on BD:} \quad p_x^{eq} = p + 2Y_c/3 \tag{22a}$$

$$\text{on EF:} \quad p_x^{eq} = p - 2Y_r/3 \tag{22b}$$

Y_c and Y_r need not be the same. Both Y_c and Y_r are positive. When a strain increment $\Delta\varepsilon_x = \Delta V/V$ is given, calculate

$$\Delta p_x' = -(\lambda + 2\mu)\Delta\varepsilon_x \tag{23}$$

$$p_x' = p_x^z + \Delta p_x' \tag{24}$$

where p_x^z is the earlier value of p_x. The current value of V, i.e., V^p, is also known. If (p_x', V^p) lies on or between BD and EF, material response is elastic and $p_x^p = p_x'$. If it lies outside the interval, it must be reduced. This can be done by setting

$$p_x^p = p(V) + 2Y(V)/3 \ , \tag{25}$$

if the equilibrium response is desired, or

$$p_x^p = p_x' - (p_x' - p_x^{eq}) \frac{\Delta t}{\tau} \tag{26}$$

if relaxation is assumed. Here p_x^{eq} is given by Eq. (22a) or (22b). The differential form corresponding to Eq. (11) is

$$\frac{dp_x}{dt} = -(\lambda + 2\mu) \frac{d\varepsilon_x}{dt} - \frac{p_x - p_x^{eq}}{\tau} \tag{27}$$

If $d\varepsilon_x = d\varepsilon_x^e + d\varepsilon_x^p$ and stress is supported entirely by elastic strain,

$$\frac{dp_x}{dt} = -\lambda \frac{d}{dt}(\quad) - 2\mu \frac{d\varepsilon_x^e}{dt}$$

$$= -(\lambda+2\mu) \frac{d\varepsilon_x}{dt} + 2\mu \frac{d\varepsilon_x^p}{dt} \tag{28}$$

Comparing Eq. (27) and (28) shows that in this case

$$\frac{p_x - p_x^{eq}}{\tau} = -\frac{2\mu d\varepsilon_x^p}{dt}$$

$$\tau = -\frac{p_x - p_x^{eq}}{2\mu\dot{\varepsilon}_x^p} \tag{29}$$

In actual computation of the uniaxial strain case, it may still be convenient to use the stress deviator formalism. In that case the computation proceeds as follows. Superscript "z" denotes values known at time t; "p" denotes those values being calculated at $t+\Delta t$; "h" denotes values midway between. V^z, S_x^z, S_y^z, S_z^z, μ^z, Y^z, and τ^z are known from the last material computation. ΔV has been calculated from the equation of continuity, $V^p = V^z + \Delta V$, $V^h = (V^z + V^p)/2$, and Δt is known. Because strain is uniaxial, only one stress deviator component is required,

$$S_y = S_z \quad S_x + 2S_y = 0 ; \qquad S_y = -S_x/2$$

Then

$$J_2 = S_x^2 + S_y^2 + S_x S_y = 3S_x^2/4 \tag{30}$$

The essence of the computation is:

$$\Delta\varepsilon_x = \Delta V/V^h \tag{31.1}$$

$$\Delta S_x' = 4\mu^h \Delta\varepsilon_x/3 \tag{31.2}$$

$$S_x' = S_x^z + \Delta S_x' \tag{31.3}$$

$$J_2' = 3(S_x')^2/4 \tag{31.4}$$

$$\text{If } J_2' \leq Y^2/3, \quad S_x^p = S_x' \tag{31.5}$$

$$\text{If } J_2' > Y^2/3, \quad \alpha \equiv Y/\sqrt{3J_2'} = r_{eq}/r' \tag{31.6}$$

If plastic flow is time-independent

$$S_x^p = \alpha S_x' \tag{31.7}$$

If plastic flow is time-dependent:

a) if $\Delta t \geq \tau$, treat as time-independent

b) if $\Delta t < \tau$,

$$\frac{r}{r'} = 1 - (1-\alpha)(\Delta t/\tau) \tag{31.8}$$

$$S_x^p = (r/r')S_x' \tag{31.9}$$

The program used for computation is somewhat more complicated than indicated above because μ and Y are assumed to depend on pressure, P, and temperature T:

$$\mu = a + bP - cT \tag{32}$$

$$Y = c_y\mu \tag{33}$$

Shear stress is assumed to be relieved during transformation according to the following model (Figure 4.3). ABCD is mean pressure in the region of the mixed phase. BC is the section which traverses the mixed phase region. A'B'CC'D' is the upper trace of the yield surface. D"C"BB"A" is its lower trace. At B', which is the boundary of the mixed phase region, *the upper yield surface is made to* collapse by setting yield strength equal to

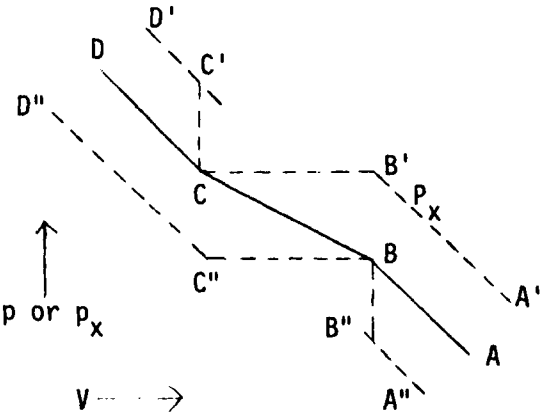

Figure 4.3: Shear relief during phase transformation

$$Y = c_y\mu(1-aq), \quad \begin{matrix} 0 < q < 1 \\ 0 \leq a \leq 1 \\ S_x > 0 \end{matrix} \tag{34.1}$$

where q is mass fraction transformed to the higher density phase. At CC' the yield

surface is allowed to return to its normal value.

Between C" and B, collapse is once more allowed:

$$Y = c_y\mu[1 + a(q-1)] \quad , \quad \begin{matrix} 0 < q < 1 \\ 0 \leq a \leq 1 \\ S_x < 0 \end{matrix} \tag{34.2}$$

A flow chart for the stress deviator computation, which encompasses Eqs. (30)-(34), is shown in Figure 4.4.

Experience with the numerical computation shows that the deviator collapse function of Eq. (34) varies too slowly with q. The following function is presently being used:

$$Y = c_y\mu[1 - \frac{2}{\pi}\tan^{-1}(aq)] \tag{35.1}$$
$$0 < q < 1$$

$$Y = c_y\mu\{1 - \frac{2}{\pi}\tan^{-1}[a(q-1)]\} \tag{35.2}$$
$$0 < x < 1$$

Some references which provide background for this computation are Wilkins (1964), Johnson et al. (1970), Johnson and Band (1967), and Lawrence (1973).

4.3 Numerical Computations

The primary point of these computations is to display the effects on wave form which result when stress deviators are made to collapse during phase transition. A great many variations are possible, but four have been chosen. In one case (Figs. 4.5a) the shock transition pressure is substantially less than the Hugoniot Elastic Limit (HEL). It is seen in this case that a shock wave with three breaks in profile is produced if deviators are not forced to collapse in the transition, whereas it has only two breaks if deviators do collapse. In the second case (Figs. 4.5b) the shock pressure of transition exceeds the HEL and three waves are present whether the deviators collapse or not. Deviator collapse does

Figure 4.4: Flow chart for computation of the stress deviators (Subroutine DEVIAT).

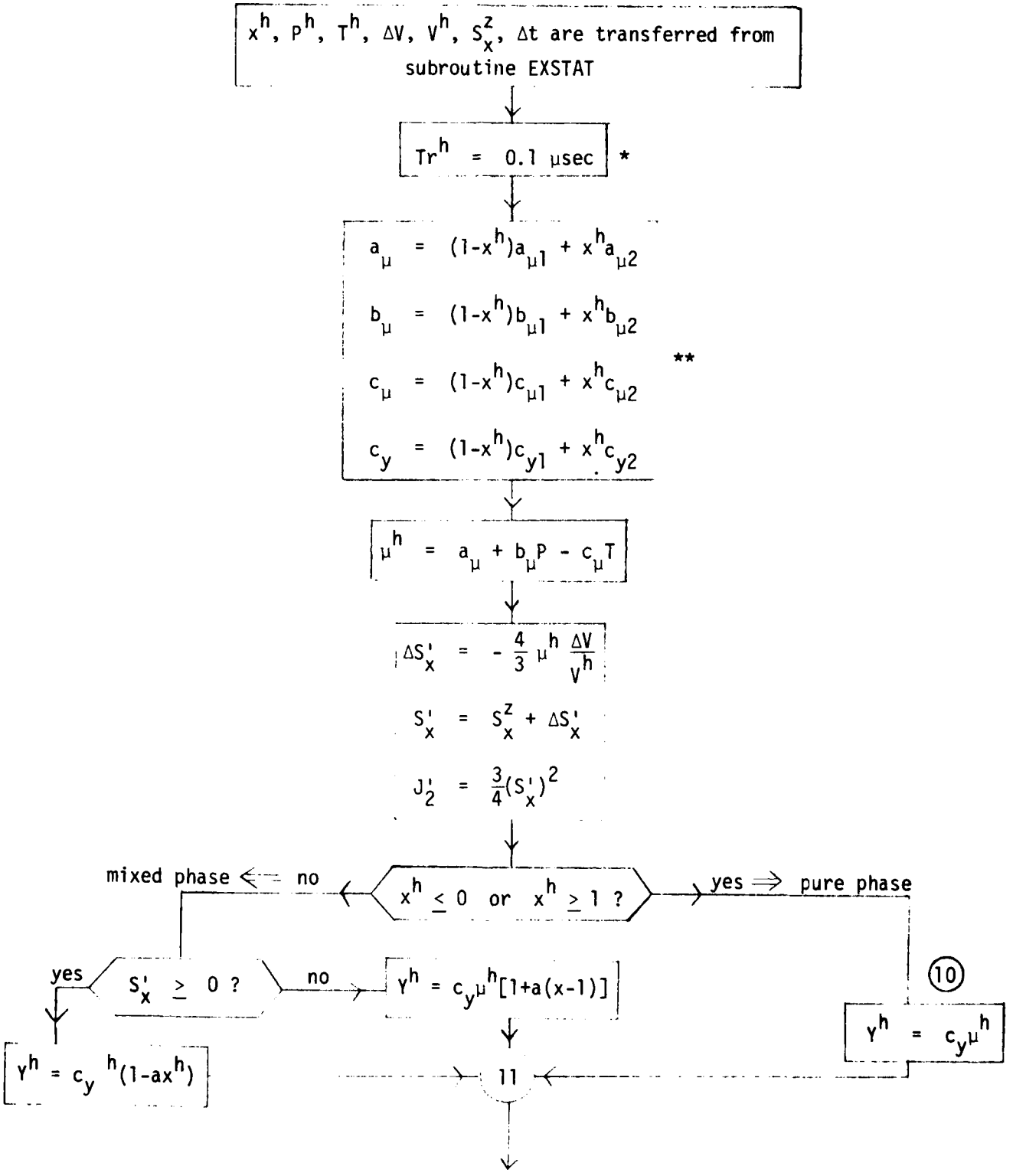

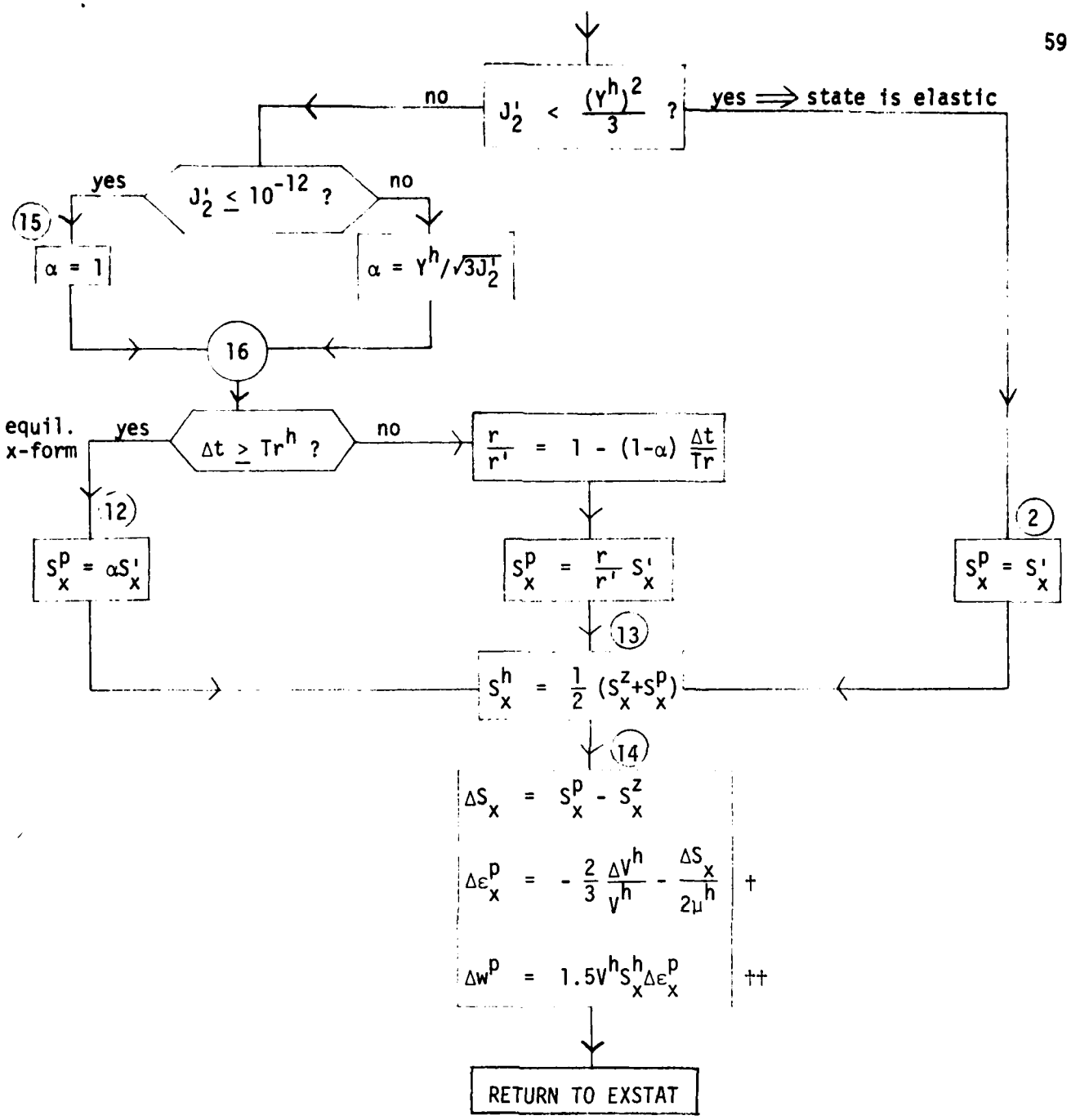

---

* Tr is relaxation time τ. Any formula can be substituted here.

** There is no substantial justification for this mixing of constants for phases 1 & 2.

† Plastic work is used in Subroutine EXSTAT in the calculation of temperature and pressure.

†† Plastic dilatation is assumed equal to zero.

produce some interesting structural details between the second and third waves, and this is something to keep in mind when examining records of phase transition. It should also be kept in mind that the profiles shown here are probably not equilibrium or steady-state profiles. Program run time is necessarily limited and details of the transformation may change considerably with a much longer run.

Figure Captions for Figs. 4.5

Effect of stress deviator collapse induced by phase transition on wave forms.

a) Shock transition pressure is less than the Hugoniot Elastic Limit (HEL), $P_x^T \simeq 9$ kbar, HEL $\simeq$ 16 kbar

(1) No deviator collapse in transition

(1.1) P_x vs. x

(1.2) P_x vs. t

(1.3) S_x vs. t

(2) Deviators collapse in transition

(2.1) P_x vs. x

(2.2) P_x vs. t

(2.3) S_x vs. t

b) Shock transition pressure is less than the HEL. $P_x^T \simeq 42$ kbar, HEL $\simeq$ 14 kbar

(1) No deviator collapse in transition

(1.1) P_x vs. x

(1.2) P_x vs. t

(1.3) S_x vs. t

(2) Deviator collapse in transition

(2.1) P_x vs. x

(2.2) P_x vs. t

(2.3) S_x vs. t

Fig. 4.5a1

Mean pressure for phase transition is $\bar{P}^T$=5.5 kilobars, corresponding to shock pressure P_x^T = 9 kilobars. The Hugoniot Elastic Limit (HEL) in the absence of transition would have been approximately 16 kbars. The stress deviator is allowed to grow during the transition, but it reaches its maximum value at point B when only about 12 percent of the material has transformed to the denser phase. Transition is not complete until point C. The three wave structure is clear. Point A marks the onset of transition, Point B is where yield first occurs, and point C is where the jump to the final state begins. Had there not been a phase transition at A, P_x would have increased smoothly to 16 kbars, and only two waves would have occurred. Oscillations in P_x and S_x following the jump to the final pressure result from choice of time step and damping coefficient.

The variation of q, the mass fraction converted to the denser phase, is interesting. Very little conversion is required to produce the first break at A and the transition is completed very quickly in a brief interval before the final jump.

Fig. 4.5a2

Mean pressure and HEL are the same as for Fig. 4.5a1, but the stress deviator, S_x, is forced to collapse when transition begins at A. The amount transformed is minute in the interval between A and B. At B the mass fraction transformed is appproximately 2%. The effect of transition on the deviator, S_x, is very small between A and B. At B the mass fraction transformed starts to increase rapidly, S_x collapses suddenly until at C the transition is essentially complete and S_x = 0. Mean pressure is essentially constant between A and C; it rises slightly as temperature increases, since the transformation is assumed to be slightly exothermic.

Details of stress behavior between A and C depend upon the model used for deviator collapse. If reductions in the deviator were very insensitive to small change in composition, a three wave structure might appear, but any reasonably rapid collapse would produce a two-wave structure similar to that shown.

The differences in behavior of mass fraction transformed with and without deviator collapse are remarkable, and the reasons for them are not apparent. Mean pressure, $\bar{P}$, rises from 5.49 kbar to 5.7 kbar with no collapse during transition; it rises from 5.49 to 5.89 with collapse. Temperature rise with collapse is about 26°C; without collapse it is about 32°C. The difference, due to the added work of deformation, probably accounts for the greater increase in pressure. This in turn may be sufficient to account for the larger values of mass fraction transformed in the no-collapse case.

What appears truly remarkable is the tiny fraction of material which must be transformed to produce a break in the wave profile. This is true both with and without deviator collapses, but is more marked in the latter case. This may explain why sluggish transitions are observed with shock waves: a combination of deviator collapse and great sensitivity of wave form to small deviations from a smooth Hugoniot.

Fig. 4.5b1

Mean pressure for the phase transition is 37 kilobars and shock pressure is 42 kilobars. The HEL is approximately 14 kilobars. The stress deviator is unaffected by the transition. The first break at point A represents yield at the HEL. The second break, at B, results from the onset of transition. As in Fig. 4.5a2, the amount transformed in the flat region following the break is very, very small. Completion of the transition occurs where the rise to the final state begins, at point C. More exactly, the fraction

transformed at 43 kbar is 89%. At the next time step P_x = 57 kbar and transformation is complete.

Fig. 4.5b2

Hugoniot Elastic Limit and transition pressure are the same as for Fig. 4.5b1, but the stress deviators are made to collapse as the transition proceeds. This wave also shows three breaks but the form differs somewhat, principally because of the nature of the function which collapses the deviators. There are four points of interest on these records. The HEL is reached at A and the stress deviator, S_x, is forced to lie on the yield surface. At B the shock transition pressure is reached, though the actual transition does not begin until point C. At C the deviator collapse begins. This record is remarkable compared to earlier ones because the transformation is delayed so long beyond the second break.

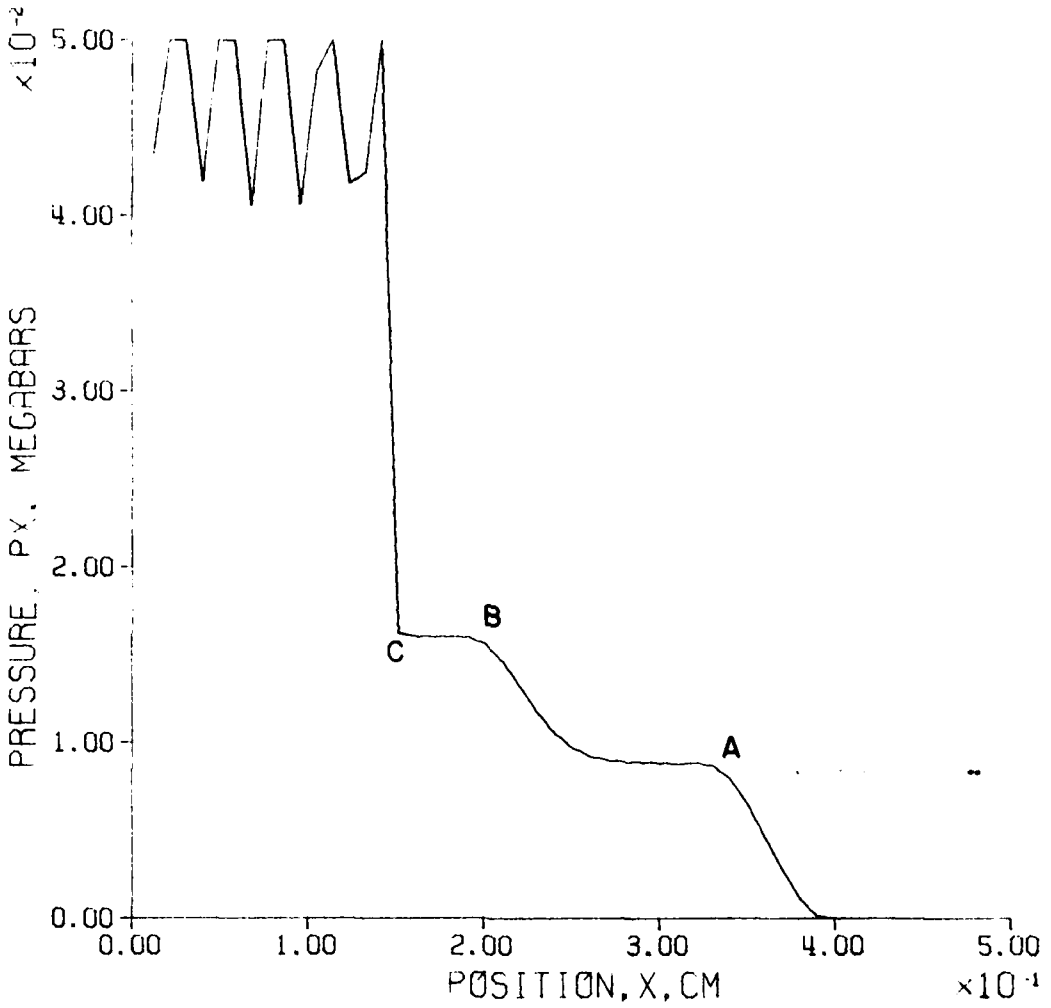
×10⁻²
5.00
4.00
3.00
2.00
1.00
0.00
PRESSURE, PX, MEGABARS
A
B
C
0.00
1.00
2.00
3.00
4.00
5.00
POSITION, X, CM
×10⁻¹

Fig. 4.5a(1.1)

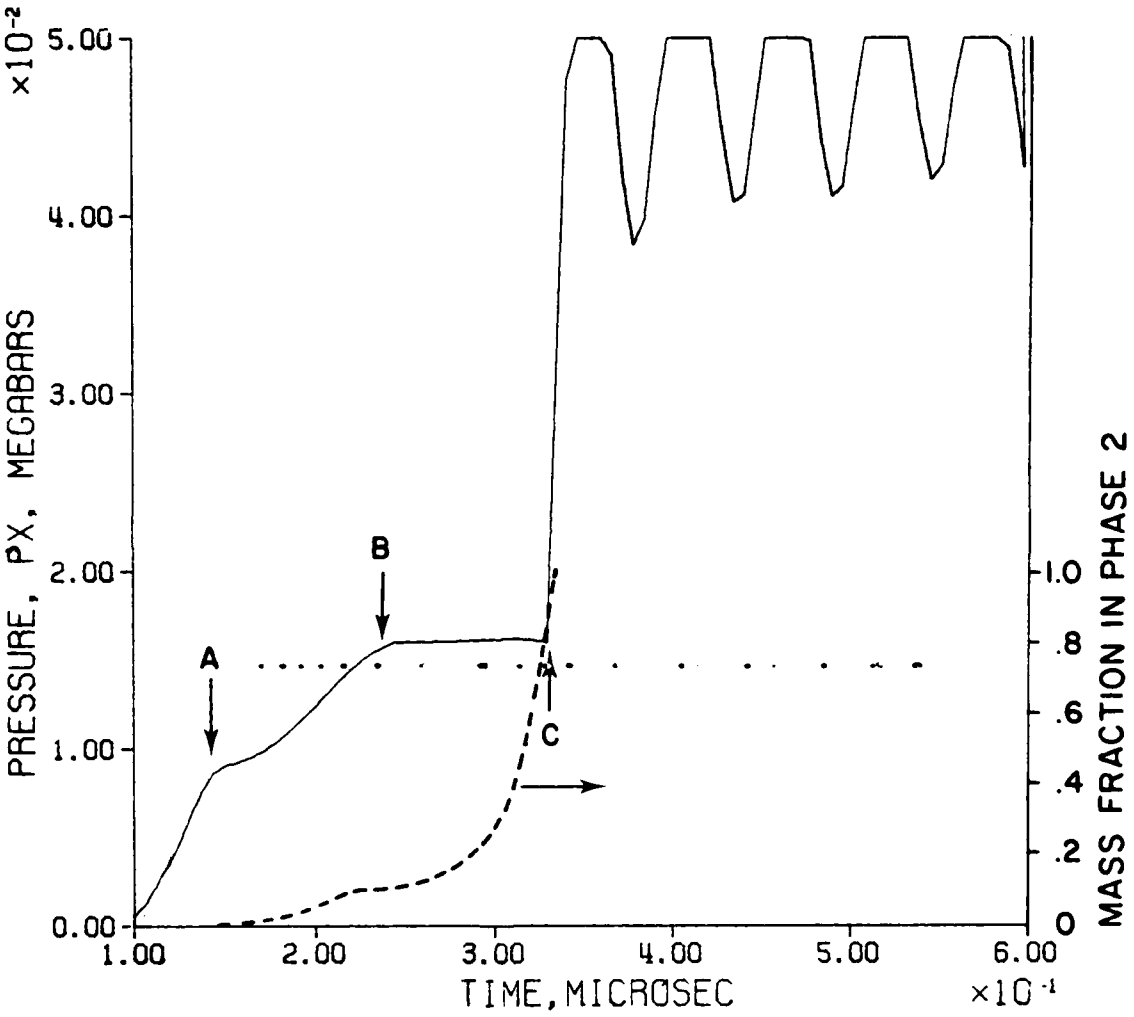
PRESSURE, PX, MEGABARS
×10⁻²
5.00
4.00
3.00
2.00
1.00
0.00
A
B
C
1.00
2.00
3.00
4.00
5.00
6.00
TIME, MICROSEC
×10⁻¹
MASS FRACTION IN PHASE 2
1.0
.8
.6
.4
.2
0

Fig. 4.5a(1.2)

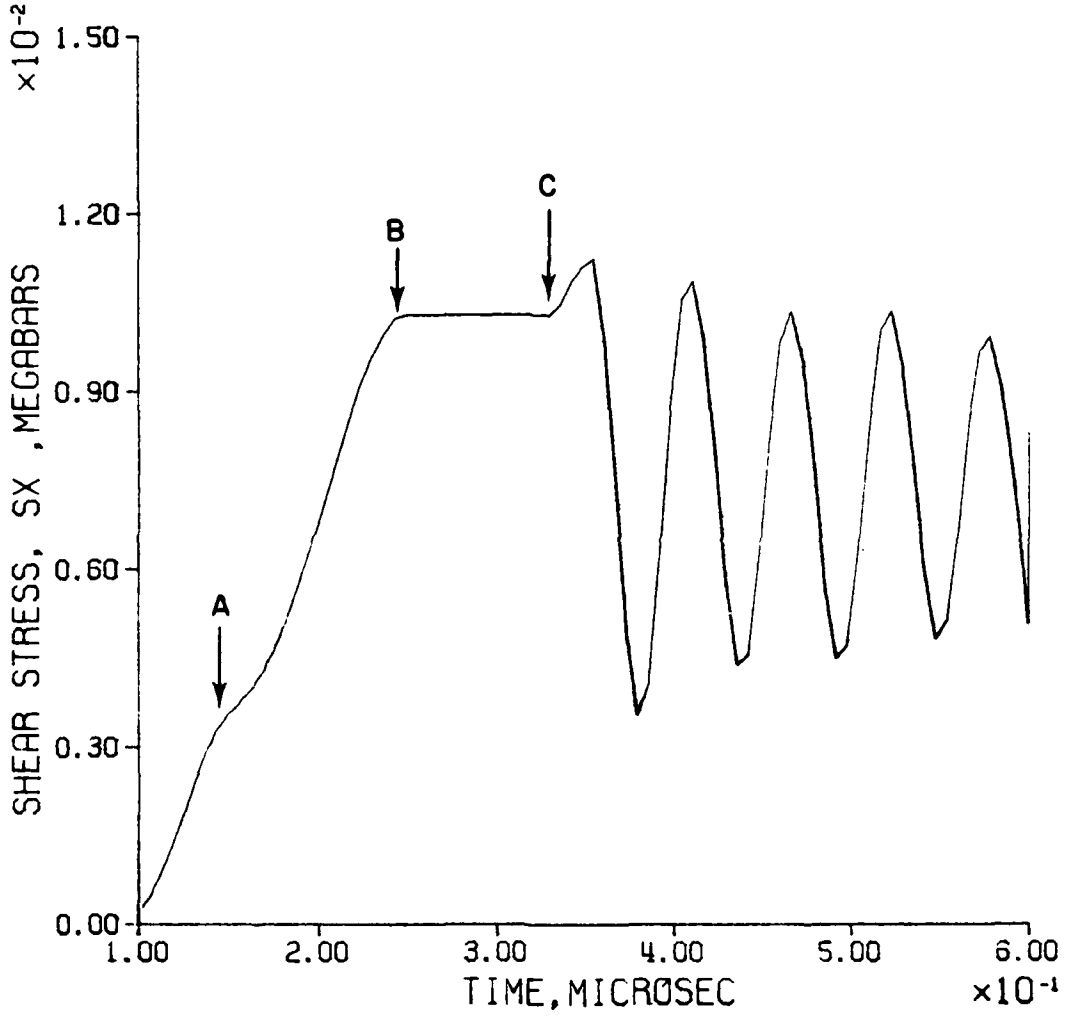
×10⁻²
1.50
1.20
0.90
0.60
0.30
0.00
SHEAR STRESS, SX , MEGABARS
A
B
C
1.00
2.00
3.00
4.00
5.00
6.00
TIME, MICROSEC
×10⁻¹

Fig. 4.5a(1.3)

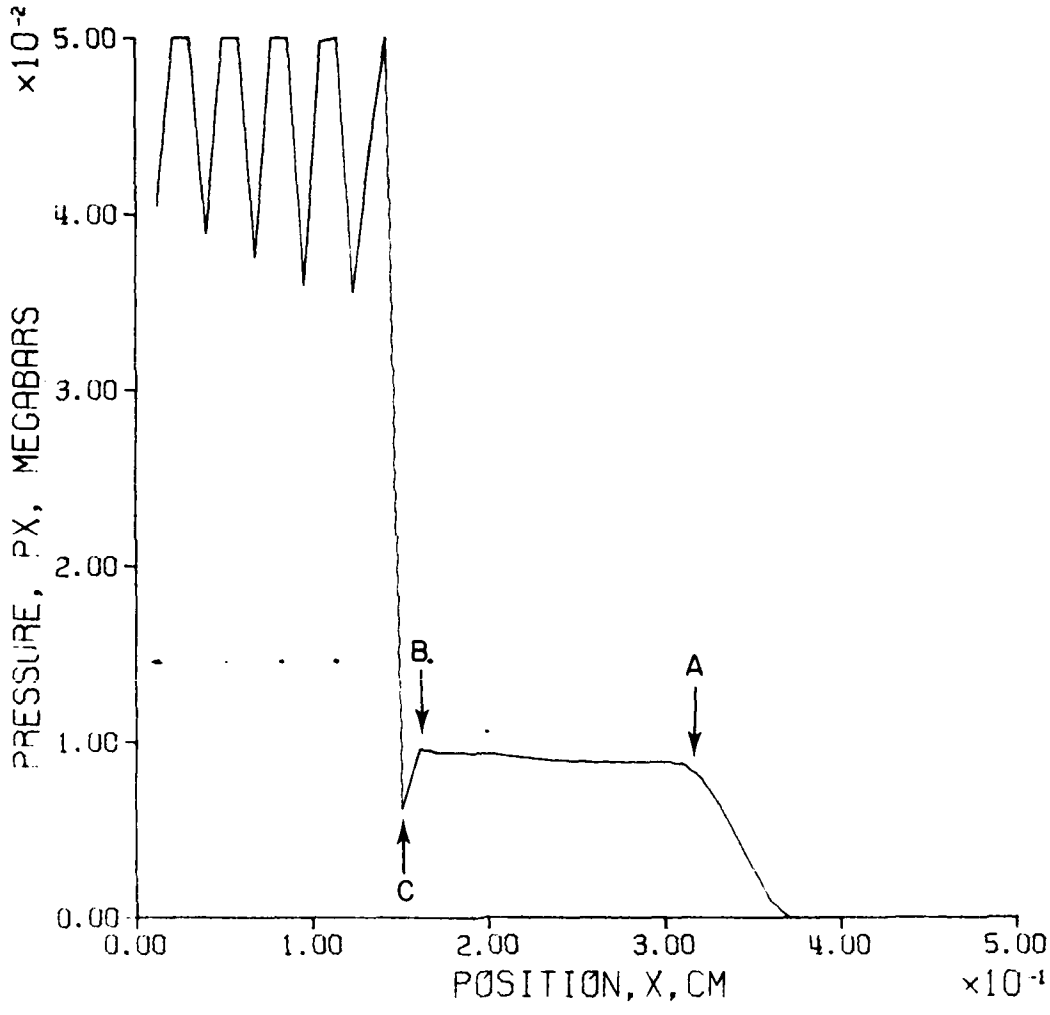
×10⁻²
5.00
4.00
3.00
2.00
1.00
0.00
PRESSURE, PX, MEGABARS
B
A
C
0.00
1.00
2.00
3.00
4.00
5.00
POSITION, X, CM
×10⁻¹

Fig. 4.5a(2.1)

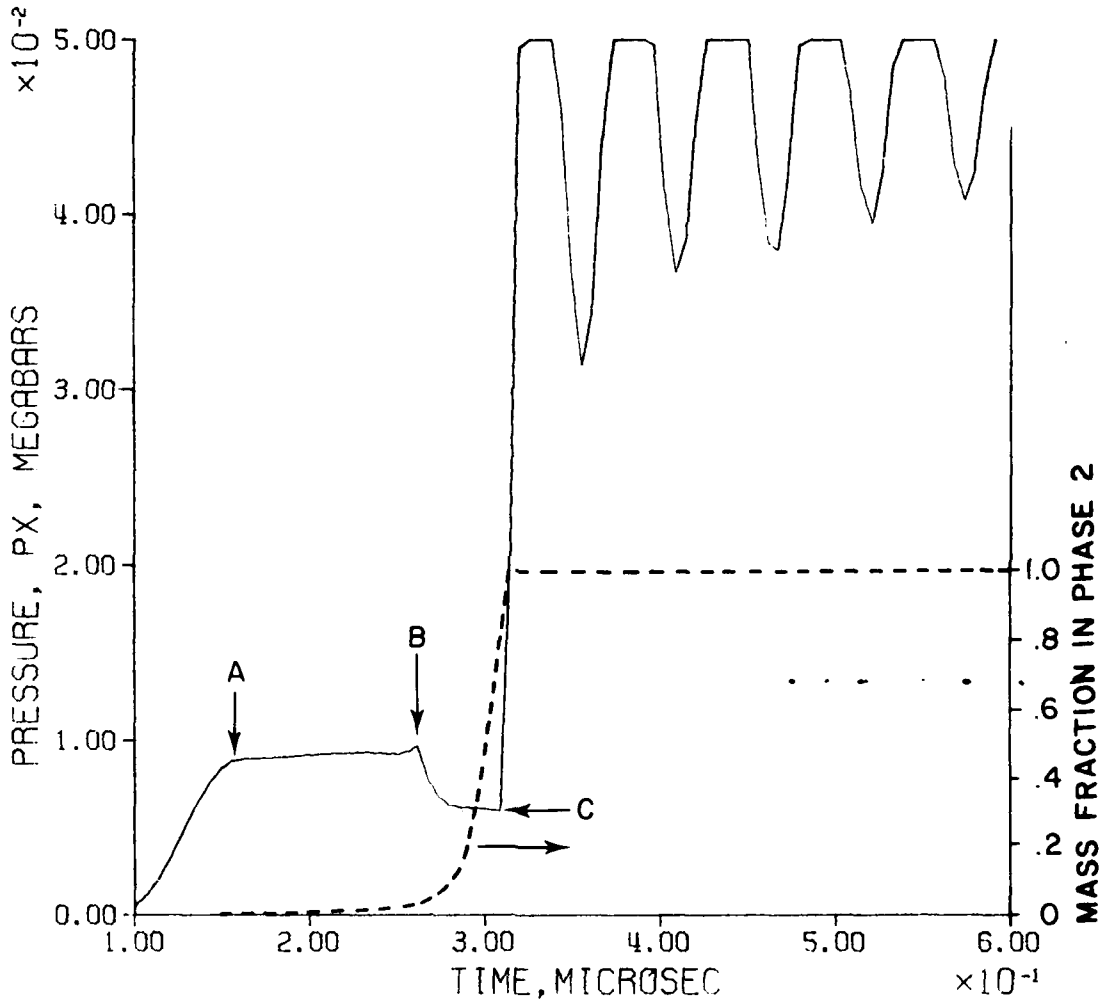
×10⁻²
5.00
4.00
3.00
2.00
1.00
0.00
PRESSURE, PX, MEGABARS
A
B
C
1.00
2.00
3.00
4.00
5.00
6.00
TIME, MICROSEC
×10⁻¹
1.0
.8
.6
.4
.2
0
MASS FRACTION IN PHASE 2

Fig. 4.5a(2.2)

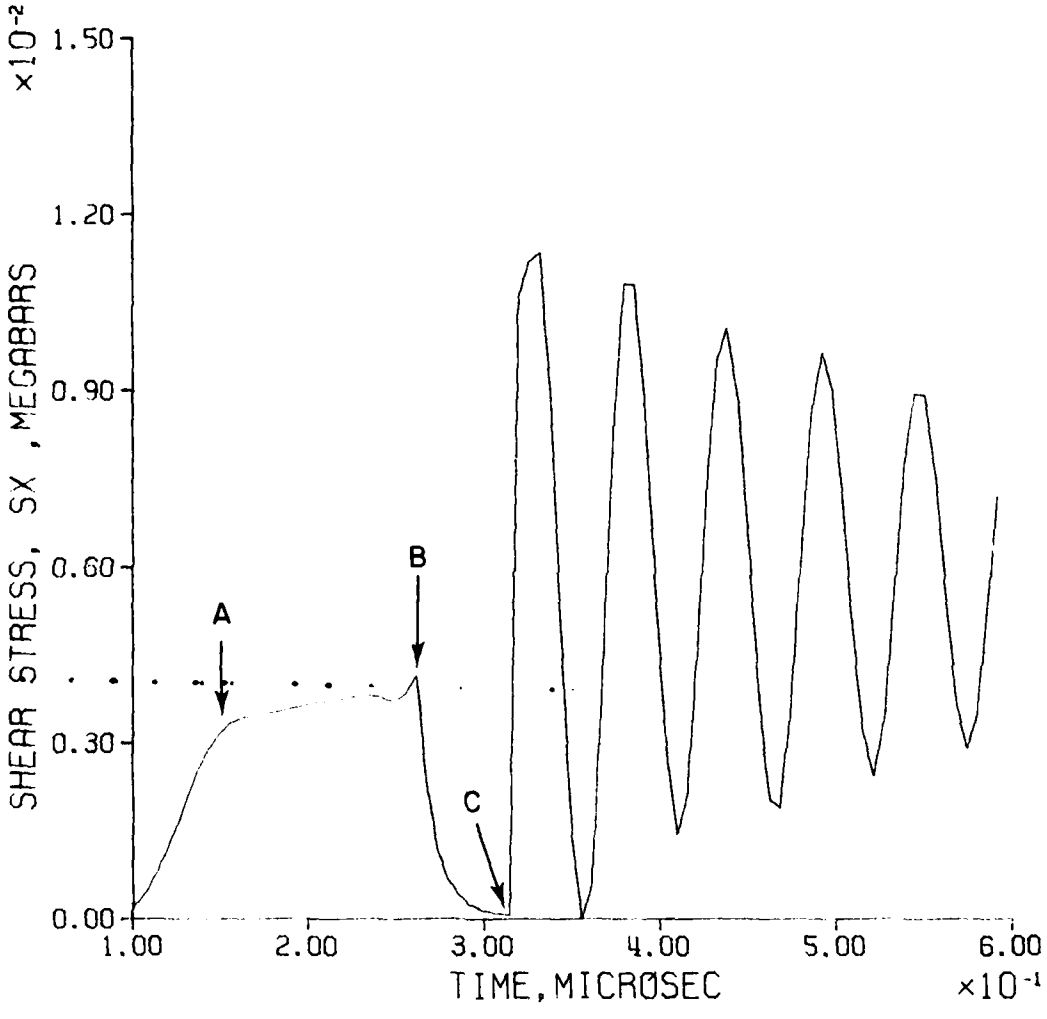
SHEAR STRESS, SX , MEGABARS
×10⁻²
1.50
1.20
0.90
0.60
0.30
0.00
A
B
C
1.00
2.00
3.00
4.00
5.00
6.00
TIME, MICROSEC
×10⁻¹

Fig. 4.5a(2.3)

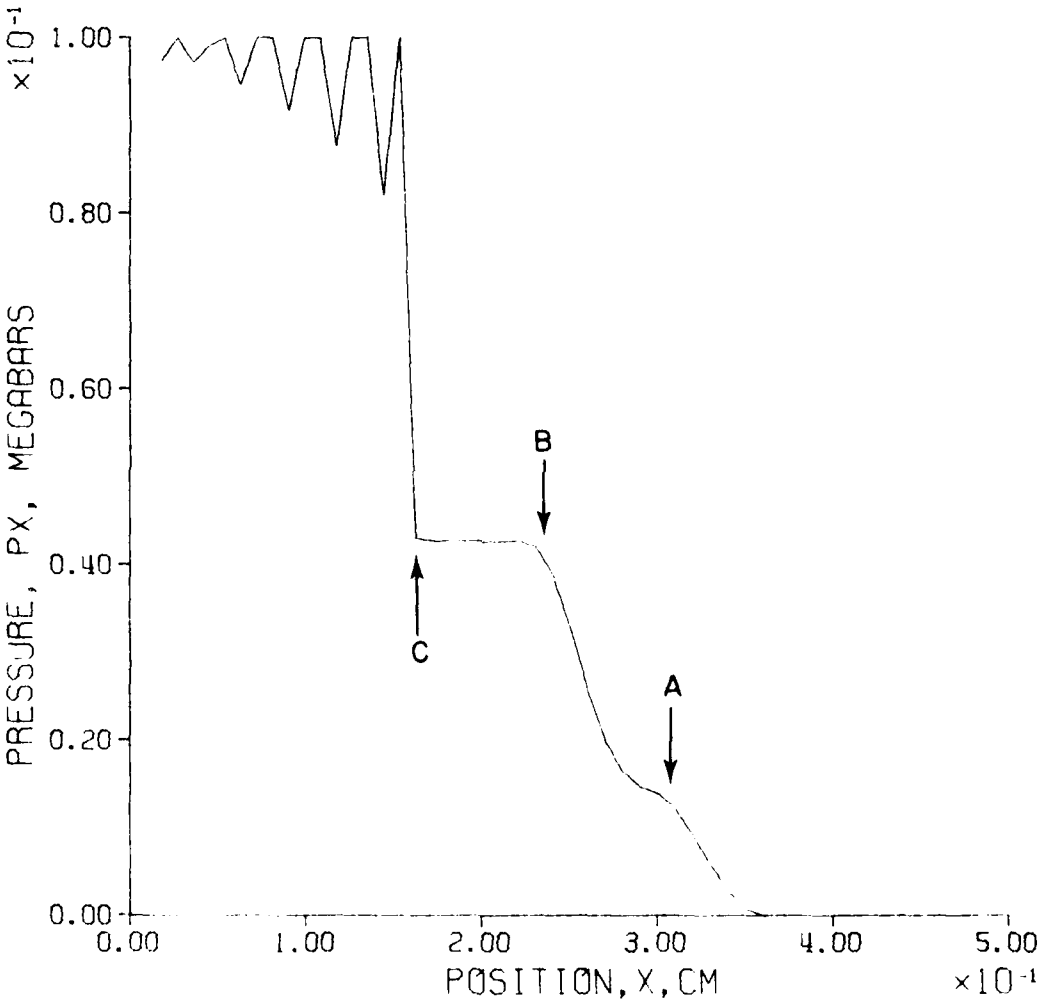
×10⁻¹
1.00
0.80
0.60
0.40
0.20
0.00
PRESSURE, PX, MEGABARS
B
C
A
0.00
1.00
2.00
3.00
4.00
5.00
POSITION, X, CM
×10⁻¹

Fig. 4.5b(1.1)

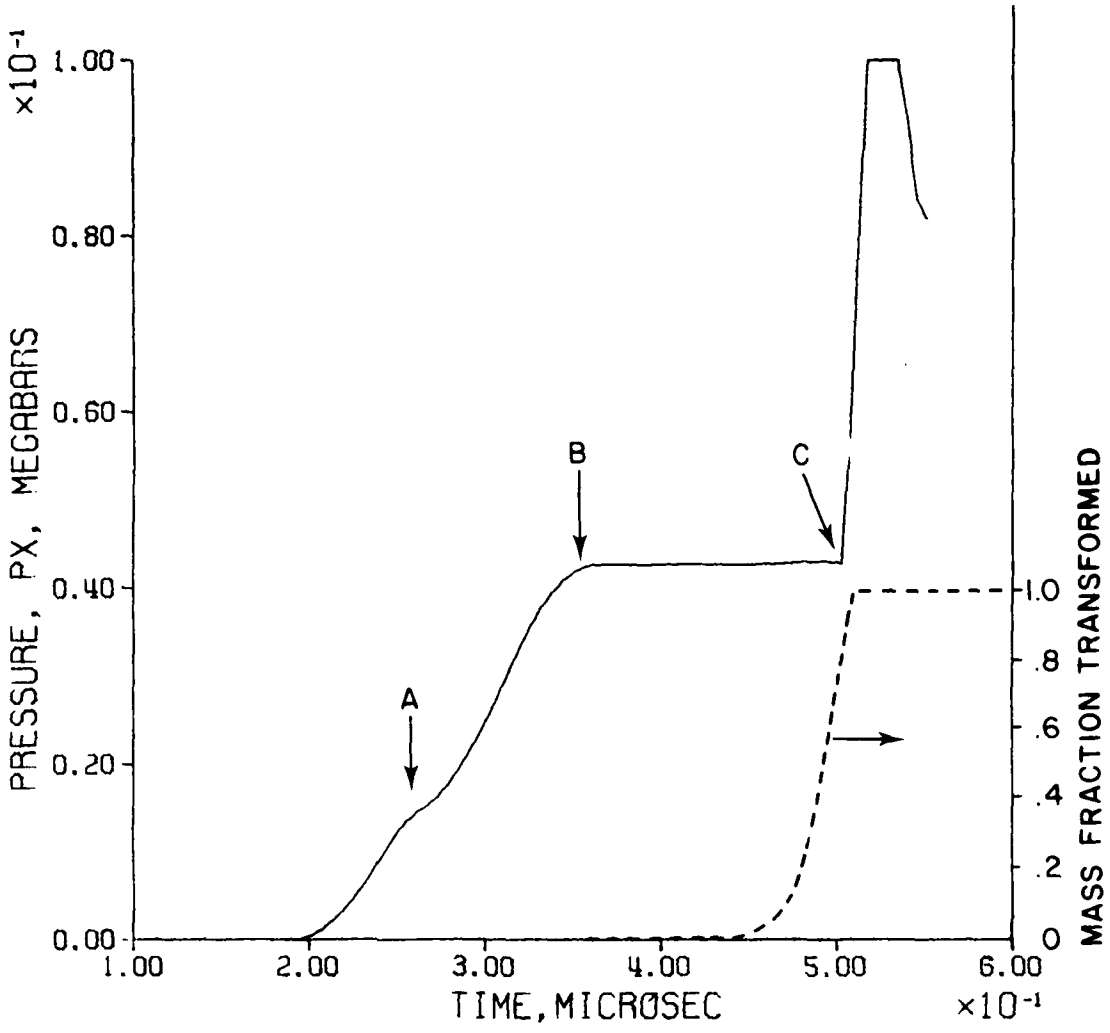
PRESSURE, PX, MEGABARS
×10⁻¹
1.00
0.80
0.60
0.40
0.20
0.00
A
B
C
1.00
2.00
3.00
4.00
5.00
6.00
TIME, MICROSEC
×10⁻¹
MASS FRACTION TRANSFORMED
1.0
.8
.6
.4
.2
0

Fig. 4.5b(1.2)

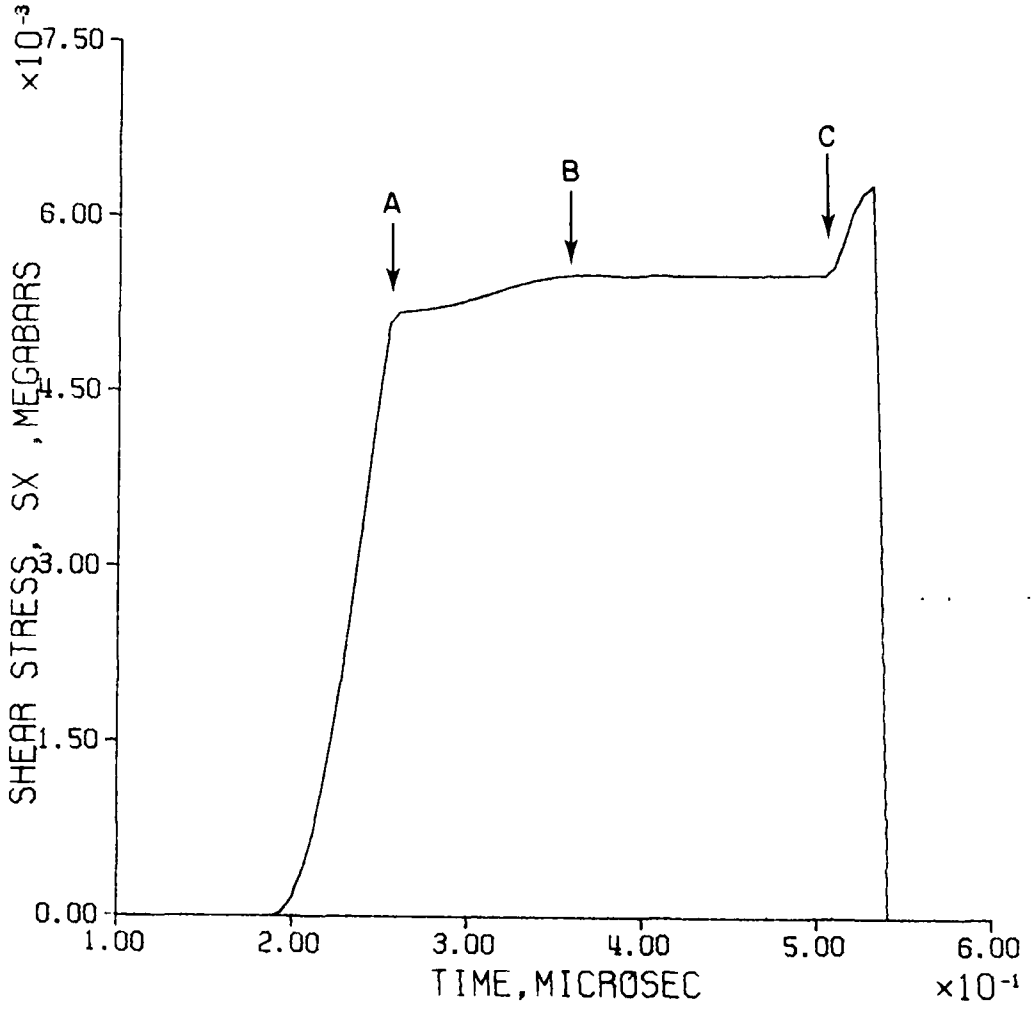
×10⁻³
7.50
6.00
4.50
3.00
1.50
0.00
SHEAR STRESS, SX , MEGABARS
A
B
C
1.00
2.00
3.00
4.00
5.00
6.00
TIME, MICROSEC
×10⁻¹

Fig. 4.5b(1.3)

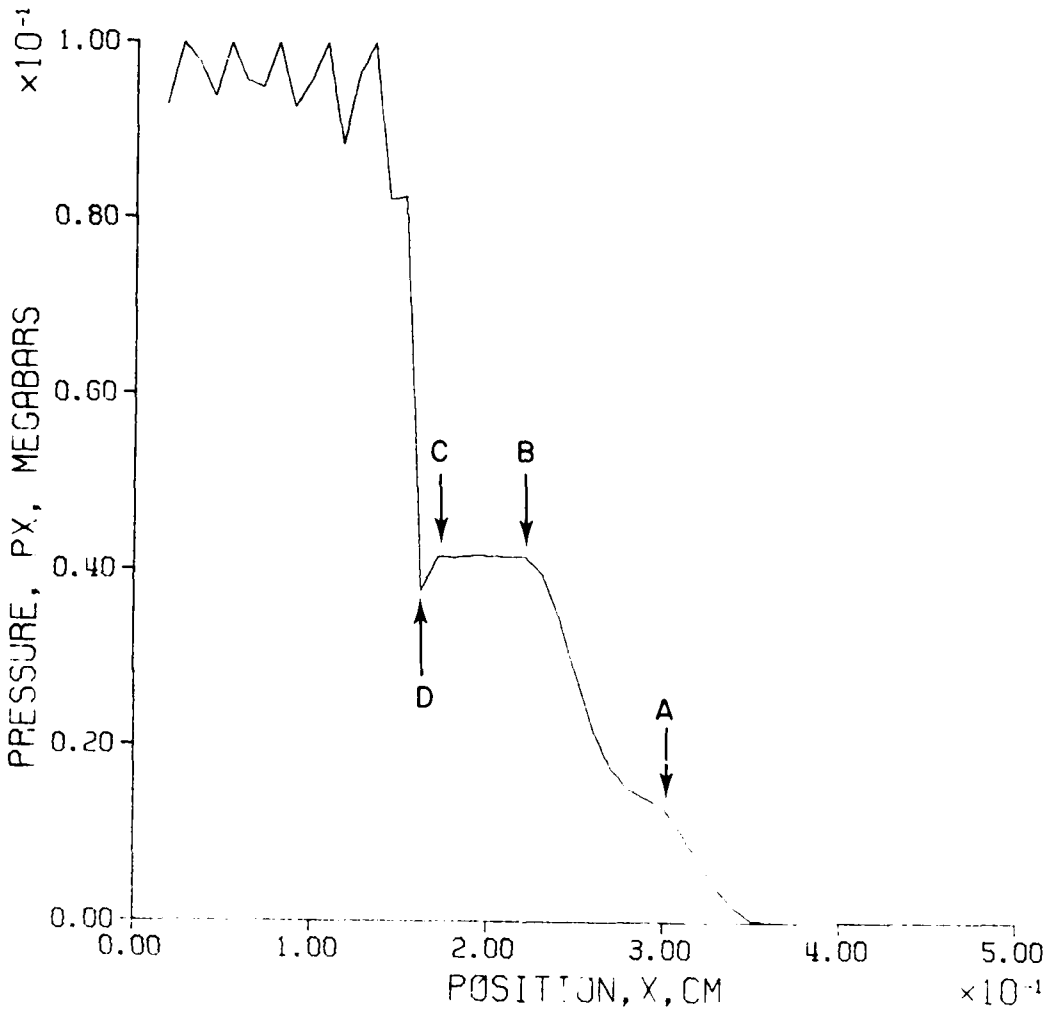
×10⁻¹
1.00
0.80
0.60
0.40
0.20
0.00
PRESSURE, PX, MEGABARS
C
B
D
A
0.00
1.00
2.00
3.00
4.00
5.00
POSITION, X, CM
×10⁻¹

Fig. 4.5b(2.1)

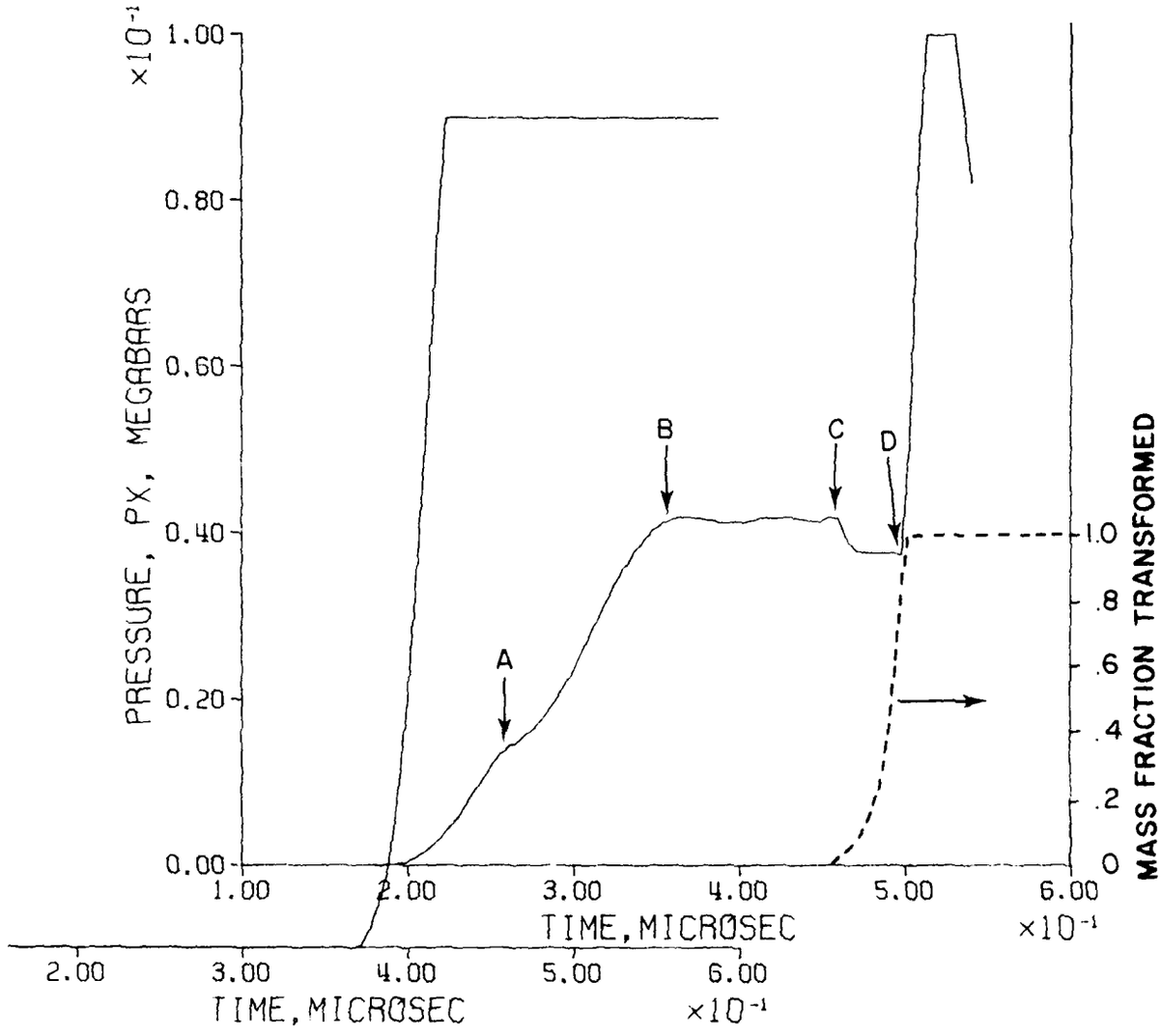
PRESSURE, PX, MEGABARS
×10⁻¹
1.00
0.80
0.60
0.40
0.20
0.00
A
B
C
D
1.00
2.00
3.00
4.00
5.00
6.00
TIME, MICROSEC
×10⁻¹
MASS FRACTION TRANSFORMED
1.0
.8
.6
.4
.2
0
2.00
3.00
4.00
5.00
6.00
TIME, MICROSEC
×10⁻¹

Fig. 4.5b(2.2)

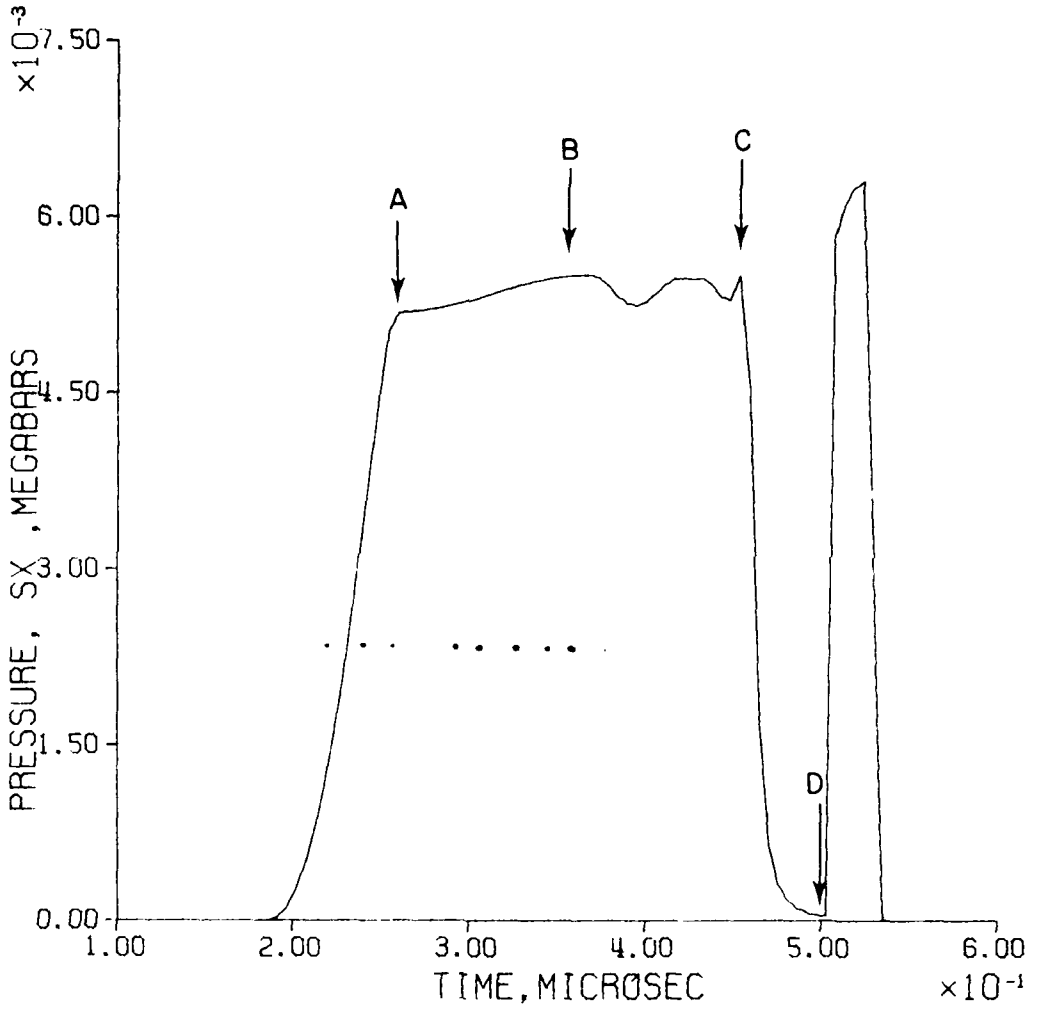
×10⁻³
7.50
6.00
4.50
3.00
1.50
0.00
PRESSURE, SX, MEGABARS
A
B
C
D
1.00
2.00
3.00
4.00
5.00
6.00
TIME, MICROSEC
×10⁻¹

Fig. 4.5b(2.3)

V. Discussion and Conclusions

i) The original concept of the experiment to study the collapse of stress deviators in a phase transition appears to have been sound. Numerical computations show that if transition occurs at lower P_x^T than HEL, a two wave structure appears if deviators collapse, three waves if they do not.

ii) Experiments are very difficult. They are plagued by extraordinary long rise times, not attributable to tilt of projectile relative to target. Not all of the experimental difficulties have been resolved, but we have reached a stage where solution appears within our grasp. Material quality and metallographic control are in hand, the furnace for hot shots is functioning well, and the tilt manipulator with auto-collimator appears to work well.

iii) There appears to be one inadequate record at T_o = 390°C which suggests deviator collapse.

iv) The P_x-T phase diagram for the Fe/30%Ni alloy agrees generally with that obtained by Rohde (1970). Low temperature points are a little higher than his, and this may relate to his observation that about 15% of the α-phase transformed to austenite before the transition pressure was reached.

v) Examination of recovered specimens for austenite suggests that the final phase reached in the transformation depends on impact pressure and initial temperature. The records are not complete, but they are in accord with the hypothesis that a triple point exists at about 200°C. At higher temperatures the material is shocked directly into the γ-phase. At lower temperatures and moderate pressures the shock carries the material into a different phase--possibly ε; and at

lower temperatures and high pressures it may be carried across the α-ε and ε-γ lines directly into the γ-phase. The speculative nature of this hypothesis has to be emphasized.

vi) Elastic precursors are often ill defined in this material, perhaps because of the dendritic structure of the martensite, but the average precursor amplitude is 9.0 ± 1 kbar and it appears to be independent of sample temperature between 20°C and 225°C.

There are several directions in which further work would be profitable:

a) With present information in hand study the α-γ transition in Fe/30Ni in the high temperature region ($\sim$400°C) for appearance and disappearance of two and three wave structures, depending on temperature. This was the principal original aim and it now appears to be within our grasp.

b) Determine in more detail the structure of the phase line and, by varying impact pressure, attempt to outline the ε-γ line (if it exists).

c) Extend these studies to other materials. Fe/Cr/Ni systems would be of considerable interest.

PART B

R. J. Livak

I. Metallurgical Processing

1.1 Material Fabrication

The Fe-30%Ni alloy used in this study was prepared by Carpenter Technology in Reading, Pennsylvania. A 200 mm long ingot with a square cross section that tapered from 70 mm on a side at the top to 48 mm at the bottom was vacuum induction melted and cast to assure metal cleanliness. The first ingot was received in the as-cast condition and was found to contain a large center pipe and extensive porosity. The unsound condition of this ingot made it unsuitable to use for the shock loading experiments.

A second ingot was prepared by vacuum induction melting and hot forged to produce a double octagon rod approximetely 38 mm in diameter in order to alleviate any casting porosity or pipe. The cast ingot was heated to 1150 - 1175°C for one hour, and one end was hot forged at this temperature. The ingot was reheated for 30 minutes, and then the other end was hot forged. The chemical composition of this second ingot, as determined by spectrographic and wet chemical analyses done by the supplier, is given in Table I.

TABLE I: Chemical Analysis of Fe-30%Ni Alloy

Heat No.	C	Mn	Si	P	S	Cr	Ni	Fe
00291	.005	<.01	<.01	<.005	.002	.01	29.85	Bal

1.2 Heat Treatment

Cylindrical samples for the shock experiments were cut and machined from the supplied rod and then heat treated to produce a martensitic (α') structure. The samples were austenitized in small stainless steel heat treating bags at 650°C for 2 hours to give the face-centered cubic γ phase. After cooling to room temperature in water, the samples were transformed to martensite by quenching to -196°C in liquid nitrogen.

Difficulties were encountered in resolving the Hugoniot elastic limit for the shock loaded martensitic samples. Because grain size can influence the relative distinctness of the HEL on the shock wave record, recrystallization experiments were done in an effort to develop a smaller grain size. Two sets of samples were reduced in thickness 28% and 40% by cold rolling and then samples were annealed for 20 minutes at temperatures ranging from 575°C to 675°C in 25°C increments. The annealed grain structures consisted of fairly equiaxed grains having a large variation in grain size and there were numerous annealing twins. All the annealed samples given 28% cold reduction had similar grain structures with a grain size of approximately 7 grains/mm as measured by the linear intercept method. For the samples given 40% cold reduction, the one annealed at 575°C had a somewhat smaller grain size of approximately 8 grains/mm than the other samples. None of the cold worked and annealed samples showed a significant reduction in grain size.

The thermal kinetics of the reverse transformation from martensite to austenite ($\alpha' \rightarrow \gamma$) were studied because some of the target samples were heated prior to shock loading up to 400°C for times as long as 30 minutes. A set of samples transformed to martensite in liquid nitrogen were given isochronal aging treatments for 30 minutes at temperatures ranging from 200°C to 550°C in 50°C increments. Up to 350°C, there was no observable

change in the martensitic microstructure as determined by optical metallography. The sample aged at 400°C showed partial transformation to austenite, and at 450°C the reverse transformation $\alpha' \rightarrow \gamma$ had almost proceeded to completion.

II. Microstructural Analysis

2.1 Optical Metallography

The metallurgical structures of samples given various treatments were examined using standard metallographic techniques. The samples were mounted in a room temperature thermosetting plastic (Kold Mount), ground to a flat surface, and then hand ground on wet silicon carbide abrasive paper to 600 grit. Polishing was done on a 6 μm diamond abrasive wheel followed by a final polish using a 0.05 μm gamma alumina wheel. The polished samples were etched by swabbing with 3% Nital (3% nitric acid in ethanol) and then examined with a metallurgical microscope at magnifications up to 500X.

Typical micrographs of the Fe-30%Ni samples prepared from the second ingot are shown in Plate I. The characteristic platelet martensite structure of a sample austenitized at 650°C and quenched in liquid nitrogen is shown in Plate I, top left. An example of a sample shock loaded to 90 kbars at room temperature (shot no. 79-039) is shown in Plate I, top right, for comparison. The appearance of both microstructures is very similar. One difference in the shock loaded sample is the occurrence of thin deformation twins in an austenite grain shown more clearly in Plate I, bottom left. These microstructures are similar to earlier results reported by Leslie et al. (1964) for an Fe-32%Ni alloy.

The samples shock loaded at elevated temperatures had similar microstructures, although there appeared to be a greater amount of austenite present as indicated by the light, featureless areas shown in Plate I, bottom

PLATE I

Optical micrographs of polished samples that were etched with 3% Nital.

top left: Fe-29.85%Ni alloy transformed to martensite by quenching to -196°C. Magn. 125X.

top right: Sample 79-039 after shock loading to 90 kbars at ambient temperature. Magn. 250X.

bottom left: Same sample as in top right. Magn. 250X.

bottom right: Sample 79-044 after shock loading to 65 kbars at 200°C. Magn. 125X.

PLATE I

right, of shot no. 79-044 shocked to 65 kbars at 200°C. The samples loaded to higher shock pressures showed evidence of grain boundary cracking, and one sample loaded to 140 kbars (no. 79-046) broke into several pieces.

2.2 Retained Austenite Measurements

Quantitative determination of the amount of retained austenite in liquid nitrogen quenched samples was done using the x-ray diffraction method described by Miller (1964). This technique is based on an empirical relationship between the integrated intensities of low order x-ray reflections from the face-centered cubic γ-phase and the body-centered α'-phase. The amount of austenite in some of the shock loaded samples was also measured. As reported earlier by Rohde et al. (1968) for the shock wave induced reverse martensitic transformation in an Fe-30%Ni alloy, the amount of reversal to the austenitic phase increases with increasing shock stress.

2.3 Transmission Electron Microscopy

To do more detailed microstructural analyses, thin foil samples for transmission electron microscopy (TEM) were prepared by electrochemical polishing. Thin slices approximately 400 μm thick were cut from the shock loaded samples using a low speed diamond cut-off wheel. These slices were hand ground to 200 μm thickness using wet silicon carbide abrasive paper and then chemically polished to 100 μm thickness in a hot mixed acid solution containing two parts acid ($10HCl:2HNO_3:1H_3PO_4$) to one part water. Small discs, 3 mm in diameter, were mechanically punched from the thinned slices for subsequent jet polishing. Final electrochemical polishing was done in a double jet polishing apparatus using a 5% perchloric acid/95% methanol electrolyte cooled to -35 to -40°C in a dry ice/isopropyl alcohol bath. A voltage of 80 V was used for polishing, and an optical sensing mechanism automatically turned off the current when perforation of the foil occurred.

The thin foils were examined in a JEM-200A electron microscope operated at an accelerating voltage of 200 kV to give maximum penetration of the foils. This instrument is located at the Hanford Engineering Development Laboratory (HEDL) in Richland, Washington, which is operated by Westinghouse under contract for the U.S. Department of Energy. Access to this instrument for this study was made possible by the kind cooperation of the personnel in the electron microscopy group at HEDL under the direction of J. Straalsund and T. Bierlein.

The TEM analysis involved the examination of bright-field and dark-field images of the microstructures in conjunction with selected-area electron diffraction patterns. In addition to dense dislocation tangles in the shock loaded samples, a prominent feature was the occurrence of microtwinning within the martensite platelets as shown in Plate II. Mechanical twinning in body-centered cubic metals becomes a preferred mode of deformation at high strain rates. Note in Plate II, bottom, that microtwinning did not occur in the adjoining martensite platelet. As shown in Plate III, microtwinning also occurred in a sample that had been transformed to martensite in liquid nitrogen but not shock loaded. There are a few twins visible in this micrograph that formed on a secondary twinning system at right angles to the primary twins. Dark-field imaging of the area in Plate III using a (002) α' reflection confirmed that these microtwins had formed in the martensite phase.

Most of the areas observed in the TEM thin foils were the body-centered cubic phase as determined by electron diffraction analysis. A few localized areas of the face-centered cubic austenite phase were observed. The heavily dislocated substructure gave poor image contrast and made analysis more difficult. The thin foil samples were ferromagnetic which caused deflection of the electron beam and gave some problems in orienting the foils for optimal

PLATE II

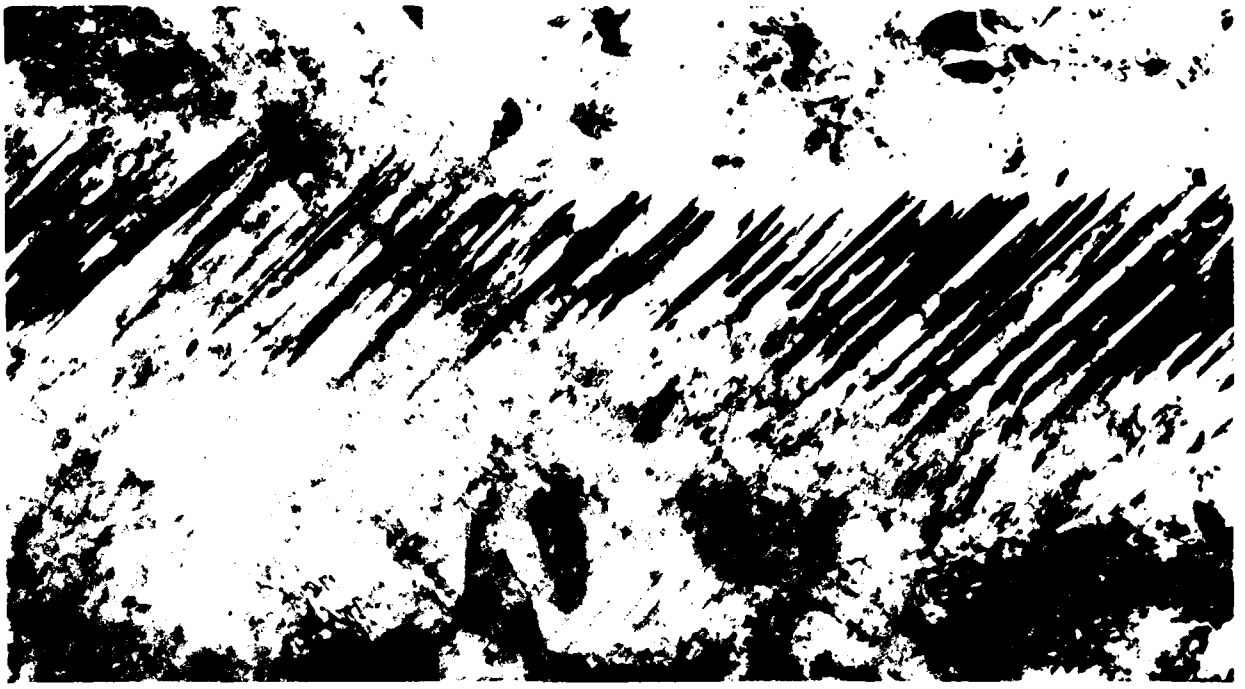

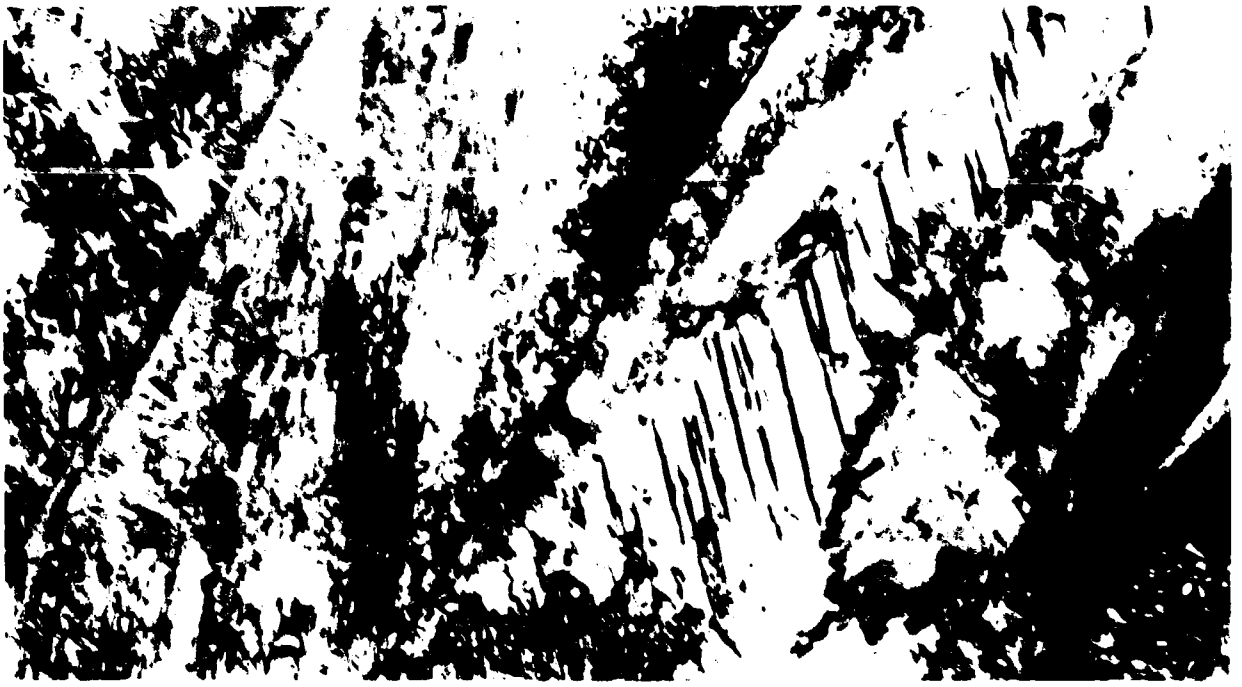

PLATE III

PLATE II

Transmission electron micrographs of thin foils prepared from shock loaded samples showing microtwinning.

top: Sample 79-039 shock loaded to 90 kbars at ambient temperature. Magn. 84,000X.

bottom: Sample 79-044 shock loaded to 65 kbars at 200°C. Magn. 135,000X.

PLATE III

Transmission electron micrograph of sample transformed to martensite by quenching to -196°C. Note small amount of microtwinning on secondary twinning system. Magn. 102,000X.

image contrast. Because the amount of austenite observed after shock loading depends upon the driving pressure (Rohde et al., 1968), these TEM observations indicate that relatively small volume fractions of austenite were produced by the pressure-temperature conditions used for these shock experiments. One of the thin foils after electropolishing was observed to have surface relief or rumpling around the hole indicating that thinning of the sample had resulted in the occurrence of the martenistic shear transformation.

Appendix to Part A

SOME NOTES ON PLASTICITY THEORY

The two principal postulates of conventional, time independent, isotropic plasticity theory are:

a) There exists a scalar yield function, $f(\underset{\sim}{\sigma})$, such that

$$\begin{aligned} f(\underset{\sim}{\sigma}) &\leq 0 \quad \text{when behavior is elastic} \\ f(\underset{\sim}{\sigma}) &= 0 \quad \text{when behavior is plastic} \end{aligned} \tag{1}$$

The equality defines the yield surface.

b) Increments in the various components of plastic strain make a constant ratio with corresponding derivatives of f:

$$\frac{d\varepsilon^p_{11}}{\partial f/\partial\sigma_{11}} = \frac{d\varepsilon^p_{12}}{\partial f/\partial\sigma_{12}} = \frac{d\varepsilon^p_{13}}{\partial f/\partial\sigma_{13}} = \frac{d\varepsilon^p_{22}}{\partial f/\partial\sigma_{22}} = \frac{d\varepsilon^p_{23}}{\partial f/\partial\sigma_{23}} = \frac{d\varepsilon^p_{33}}{\partial f/\partial\sigma_{33}}$$

This is more commonly written

$$d\varepsilon^p_{ij} = d\lambda \frac{\partial f}{\partial\sigma_{ij}} \tag{2}$$

where λ is a "progress parameter" for the loading process. It may vary as loading progresses.

Equation (2) is known as an "Associated Flow Rule," or sometimes "The Normality Condition." The latter name comes from the following relation:

$$\frac{df}{dt} = \frac{\partial f}{\partial\sigma_{ij}} \frac{d\sigma_{ij}}{dt}$$

In a space σ_{ij} of nine dimensions, f = const. describes an 8 dimensional surface gradient, $\nabla f = (\partial f/\partial\sigma_{ij} \cdot \hat{a}_{ij})$ is a vector normal to that surface. If the stress

AD-A082 003 WASHINGTON STATE UNIV PULLMAN DEPT OF PHYSICS F/G 11/6
SHOCK-INDUCED MARTENSITE REVERSAL IN FE/30%NI.(U)
FEB 80 G E DUVALL, P M BELLAMY, R J LIVAK DAAG29-77-C-0030
UNCLASSIFIED ARO-14619.1-MS NL

2 2

END
DATE FILMED
4 80
DTIC

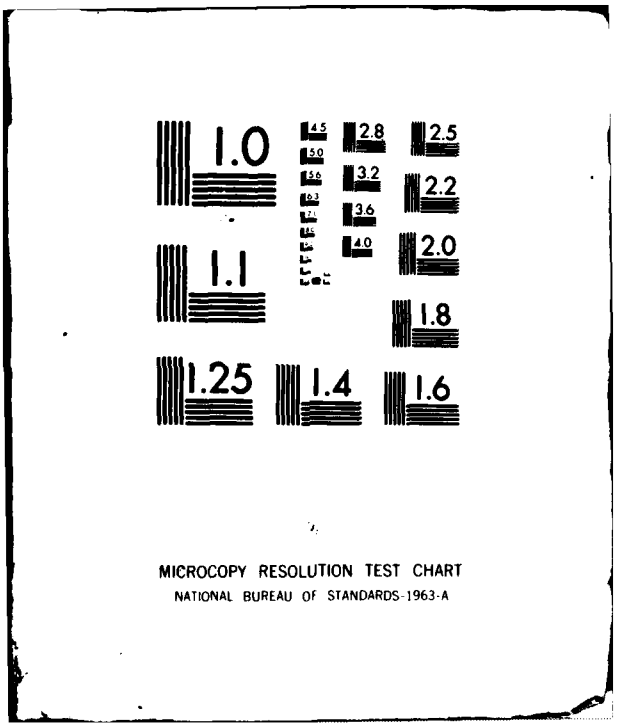

MICROCOPY RESOLUTION TEST CHART
NATIONAL BUREAU OF STANDARDS-1963-A

is constrained to lie on the yield surface, f = const., then df/dt ≡ 0 and the displacement of the nine-component stress vector must lie on the yield surface.

The yield surface, f, must be invariant under orthogonal transformation of coordinates, so it can be written as a function of the three invariants of the stress tensor, J_1, J_2, J_3. There are some variations among definitions of J_1, J_2, J_3, but the definitions given by Malvern (1969) are common:

$$J_1 = \sigma_{11} + \sigma_{22} + \sigma_{33} \equiv \sigma_{kk} = \mathrm{Tr}\underset{\sim}{\sigma} = -3p \tag{3}$$

where p is mean pressure.

$$J_2 = -(\sigma_{11}\sigma_{22} + \sigma_{22}\sigma_{33} + \sigma_{33}\sigma_{11}) + \sigma_{23}^2 + \sigma_{31}^2 + \sigma_{12}^2 \tag{4}$$

$$= \frac{1}{2}(\sigma_{ij}\sigma_{ij} - \sigma_{ii}\sigma_{jj}) = \frac{1}{2}\sigma_{ij}\sigma_{ij} - \frac{1}{2}J_1^2 \tag{4b}$$

$$J_3 = \det \underset{\sim}{\sigma}$$

$$= \begin{vmatrix} \sigma_{11} & \sigma_{12} & \sigma_{13} \\ \sigma_{21} & \sigma_{22} & \sigma_{23} \\ \sigma_{31} & \sigma_{32} & \sigma_{33} \end{vmatrix} = \frac{1}{6} e_{ijk} e_{pqr} \sigma_{ip} \sigma_{jq} \sigma_{kr} \tag{5}$$

It is almost universally believed that f is independent of J_3. This probably means that measurements are not yet sufficiently refined to detect its influence (Gupta, 1977).

In general,
$$\frac{\partial f}{\partial \sigma_{ij}} = \frac{\partial f}{\partial J_1}\frac{\partial J_1}{\partial \sigma_{ij}} + \frac{\partial f}{\partial J_2}\frac{\partial J_2}{\partial \sigma_{ij}} + \frac{\partial f}{\partial J_3}\frac{\partial J_3}{\partial \sigma_{ij}} \tag{6}$$

From Eq. (3) $(\partial J_1/\partial \sigma_{ij}) = 1$ if $i = j$; $= 0$ if $i \neq j$, i.e.,

$$\frac{\partial J_1}{\partial \sigma_{ij}} = \delta_{ij} \tag{7}$$

From Eq. (4b):

$$\frac{\partial J_2}{\partial \sigma_{ij}} = \sigma_{ij} - J_1 \frac{\partial J_1}{\partial \sigma_{ij}} = \sigma_{ij} - J_1 \delta_{ij} \tag{8}$$

From Eq. (5):

$$\begin{aligned}\frac{\partial J_2}{\partial \sigma_{mn}} &= \frac{1}{6}\left(e_{mjk}e_{nqr}\sigma_{jq}\sigma_{kr} + e_{imk}e_{pnr}\sigma_{ip}\sigma_{kr}\right.\\ &\qquad \left. + e_{ijm}e_{pqn}\sigma_{ip}\sigma_{jq}\right)\\ &= \frac{\sigma_{jq}\sigma_{kr}}{6}\left(e_{mjk}e_{nqr} + e_{jmk}e_{qnr} + e_{kjm}e_{rqn}\right)\\ &= \frac{1}{2}\, e_{jkm}e_{qrn}\sigma_{jq}\sigma_{kr}\end{aligned} \tag{9}$$

Substitution of Eqs. (7), (8), and (9) into (6) gives

$$\frac{\partial f}{\partial \sigma_{ij}} = \frac{\partial f}{\partial J_1}\delta_{ij} + \frac{\partial f}{\partial J_2}(\sigma_{ij} - J_1\delta_{ij}) + \frac{\partial f}{\partial J_3}\frac{1}{2}\, e_{pqi}e_{kmj}\sigma_{pk}\sigma_{qm} \tag{10}$$

From Eq. (10) we can derive the following special cases.

$$\frac{\partial f}{\partial \sigma_{11}} = \frac{\partial f}{\partial J_1} + (\sigma_{11} - J_1)\frac{\partial f}{\partial J_2} + \frac{1}{2}\, e_{pq1}e_{km1}\sigma_{pk}\sigma_{qm}\frac{\partial f}{\partial J_3}$$

The last term on the right hand side is

$$\begin{aligned}\frac{1}{2}(\delta_{pk}\delta_{qm} - \delta_{pm}\delta_{qk})\sigma_{pk}\sigma_{qm}\frac{\partial f}{\partial J_3} &= -\frac{1}{2}(\sigma_{pq}\sigma_{qp} - \sigma_{kk}\sigma_{mm})\frac{\partial f}{\partial J_3}\\ &= -J_2\frac{\partial f}{\partial J_3}\end{aligned}$$

i.e.,

$$\frac{\partial f}{\partial \sigma_{11}} = \frac{\partial f}{\partial J_1} + (\sigma_{11} - J_1)\frac{\partial f}{\partial J_2} - J_2\frac{\partial f}{\partial J_3} \tag{10.1}$$

similar expressions exist for $\partial f/\partial\sigma_{22}$, and $\partial f/\partial\sigma_{33}$, so

$$\frac{\partial f}{\partial p} = -3\frac{\partial f}{\partial J_1} = -3\left(\frac{\partial f}{\partial\sigma_{11}}\frac{\partial\sigma_{11}}{\partial J_1} + \frac{\partial f}{\partial\sigma_{22}}\frac{\partial\sigma_{22}}{\partial J_1} + \frac{\partial f}{\partial\sigma_{33}}\frac{\partial\sigma_{33}}{\partial J_1}\right)$$

$$= -3\left(\frac{\partial f}{\partial\sigma_{11}} + \frac{\partial f}{\partial\sigma_{22}} + \frac{\partial f}{\partial\sigma_{33}}\right)$$

or

$$\frac{\partial f}{\partial p} = -3\frac{\partial f}{\partial\sigma_{ij}}\delta_{ij} \tag{10.2}$$

As an alternative, f can be made a function of J_1, J_2^*, J_3, where J_2^* is the second invariant of the stress deviator tensor $\underset{\sim}{S}$.

$$S_{ij} = \sigma_{ij} - \frac{J_1}{3}\delta_{ij} \tag{11}$$

The trace of S_{ij} is identically zero, $J_1^* \equiv 0$. Therefore

$$J_2^* = \frac{1}{2}(S_{ij}S_{ij} - J_1^{*2}) = \frac{1}{2}S_{ij}S_{ij} \tag{12}$$

There is a simple relation between J_2^* and J_2:

$$J_2^* = \frac{1}{2}S_{ij}S_{ij} = \frac{1}{2}(\sigma_{ij} - \frac{J_1}{3}\delta_{ij})(\sigma_{ij} - \frac{J_1}{3}\delta_{ij})$$

$$= \frac{1}{2}(\sigma_{ij}\sigma_{ij} - \frac{2}{3}J_1\delta_{ij}\sigma_{ij} + \frac{J_1^2}{9}\delta_{ij}\delta_{ij})$$

$$\delta_{ij}\sigma_{ij} = \sigma_{ii} = J_1$$

$$\delta_{ij}\delta_{ij} = 3$$

Therefore

$$J_2^* = \frac{1}{2}(\sigma_{ij}\sigma_{ij} - \frac{2}{3}J_1^2 + \frac{1}{3}J_1^2)$$

$$= \frac{1}{2}(\sigma_{ij}\sigma_{ij} - J_1^2 + \frac{2}{3}J_1^2)$$

$$= J_2 + \frac{J_1^2}{3} \tag{13}$$

It's now evident that we can, without losing generality, write f as a function of (J_1, J_2^*, J_3) since J_2^* is a function of J_1 and J_2. In the special case where f depends on J_2^* alone, we have

$$\frac{\partial f}{\partial S_{ij}} = \frac{\partial f}{\partial J_2^*}\frac{\partial J_2^*}{\partial S_{ij}} = S_{ij}\frac{\partial f}{\partial J_2^*} \tag{14}$$

Probably the most commonly used yield criterion in analytical work is the von Mises criterion

$$f = J_2^* - \frac{Y^2}{3} \tag{15}$$

where Y is yield strength measured for a thin bar. Then

$$\frac{\partial f}{\partial J_2^*} = 1, \qquad \frac{\partial J_2^*}{\partial S_{ij}} = S_{ij}$$

so

$$\frac{\partial f}{\partial S_{ij}} = S_{ij} \tag{16}$$

Then the associated flow rule, Eq. (2), reduces to an analogue of Newton's Law for viscous flow:

$$d\varepsilon_{ij}^p = S_{ij}d\lambda \tag{17}$$

This same result can be obtained directly from Eq. (2), using Eqs. (7), (8), (13) and (15):

$$d\varepsilon_{ij}^p = d\lambda\frac{\partial f(J_2^*)}{\partial \sigma_{ij}} = d\lambda\frac{\partial f}{\partial J_2^*}\frac{\partial J_2^*}{\partial \sigma_{ij}}$$

$$\frac{\partial J_2^*}{\partial \sigma_{ij}} = \frac{\partial J_2}{\partial \sigma_{ij}} + \frac{2J_1}{3}\frac{\partial J_1}{\partial \sigma_{ij}}$$

$$= (\sigma_{ij} - J_1\delta_{ij}) + \frac{2J_1}{3}\delta_{ij}$$

$$= \sigma_{ij} + p\delta_{ij} = S_{ij}$$

Thus

$$d\varepsilon_{ij}^p = S_{ij}d\lambda$$

as before.

A misleading analogy is sometimes drawn between plastic flow and Newtonian flow for a viscous fluid. Divide Eq. (17) by the time increment dt and define $\kappa = dt/d\lambda$. The result is

$$S_{ij} = \dot{\varepsilon}_{ij}^p \tag{18}$$

If κ is defined as

$$\kappa = \frac{k}{\sqrt{\dot{\varepsilon}_{ij}^p \dot{\varepsilon}_{ij}^p /2}},$$

Eq. (19) is consistent with Eq. (15):

$$S_{ij}S_{ij} = 2J_2^* = \frac{2k^2\dot{\varepsilon}_{ij}^p \dot{\varepsilon}_{ij}^p}{\dot{\varepsilon}_{ij}^p \dot{\varepsilon}_{ij}^p}$$

which satisfies the conditions that $J_2^* = k^2$ at yield, with $k^2 = Y^2/3$. The analogy between Eq. (18) and Newtonian flow is misleading because $d\lambda$ is a progress parameter which has no relation to time. The basic assumption in this theory is that yield and flow are independent of time; time enters only as a progress variable.

Effect of J_1 Dependence.

If the associated flow rule applies (Eq. (2)), then any dependence of f on

J_1 is reflected by plastic dilatation, i.e.,

$$d\varepsilon_{ij}^{p} = d\lambda \left(\frac{\partial f}{\partial \sigma_{11}} + \frac{\partial f}{\partial \sigma_{22}} + \frac{\partial f}{\partial \sigma_{33}}\right) = 3d\lambda \frac{\partial f}{\partial J_1}$$

and the ratio of this increment to other plastic strain increments is, e.g.,

$$\frac{d\varepsilon_{ii}^{p}}{d\varepsilon_{ij}^{p}} = \frac{3\partial f/\partial J_1}{\partial f/\partial \sigma_{ij}} \tag{20}$$

Gupta (1977), in analyzing biaxial experiments, has found a volume change much greater than that given by Eq. (20). He concludes that from such experiments one cannot tell the difference between strain-hardening and J_1 dependence. He also points out that in minerals and rocks the flow rule, Eq. (2), is commonly violated, and he concludes that independent physical evidence is required in order to formulate flow relations for *equilibrium plasticity*. There is, furthermore, no violation of fundamental physical theories in assuming that $d\varepsilon_{ij}^{p} = 0$ when yield strength depends on pressure. The difficulty of resolving such questions is indicated by the following example for uniaxial strain. In that case

$$S_x \equiv S_{11} = -2S_y; \quad S_{ij} = 0, \; i \neq j$$

Where $S_y = S_{22} = S_{33}$,

$$J_2^* = 3S_x^2/4$$

If yield stress is a function of pressure, $p = -J_1/3$, Eq. (15) becomes

$$f(J_2^*, J_1) = \frac{3S_x^2}{4} = \frac{1}{3} Y(J_1)^2 \tag{21}$$

With Eq. (21) and $i = j = 1$, Eq. (20) becomes

$$\frac{d\varepsilon_{ii}^{p}}{d\varepsilon_{11}^{p}} \equiv \frac{d\theta^{p}}{d\varepsilon_{x}^{p}} = \frac{-2YdY/dJ_1}{\partial f/\partial \sigma_x} \tag{22}$$

To calculate $\partial f/\partial \sigma_x$, note that $S_x = 2(\sigma_x - \sigma_y)/3$, so that

$$f = [(\sigma_x - \sigma_y)^2 - Y^2]/3$$

Then

$$\partial f/\partial \sigma_x = 2(\sigma_x - \sigma_y - Y dY/dJ_1)/3$$

In uniaxial compression, $\sigma_x - \sigma_y = -Y$ after yield has occurred. Also pressure, $p = -J_1/3$, is a parameter more commonly used in experiments than J_1. With these substitutions

$$\frac{\partial f}{\partial \sigma_x} = -\frac{2Y}{3}\left(1 - \frac{1}{3}\frac{dY}{dp}\right) \tag{23}$$

Substitution of Eq. (23) into (22) yields

$$\frac{d\theta^p}{d\varepsilon_x^p} = \frac{-dY/dp}{1 - (1/3)dY/dp}$$

Numerical calculations associated with shock propagation experiments often indicate a dependence of Y on p. A representative number for dY/dp is about 0.03kb/kb. Substitution of this into Eq. (24) yields

$$d\theta^p/d\varepsilon_x^p \simeq -0.03 \tag{25}$$

The principal experimental effect of plastic dilatation is to modify the relations among stress and observable strains. Incremental stresses in uniaxial strain are written as

$$d\sigma_x = \lambda d\theta^e + 2\mu d\varepsilon_x^e$$

$$d\sigma_y = \lambda d\theta^e + 2\mu d\varepsilon_y^e$$

These can be transformed to the forms

$$d\sigma_x = (\lambda + 2\mu)d\varepsilon_x - 2\mu d\varepsilon_x^p\left(1 + \frac{\nu}{1-2\nu}\frac{d\theta^p}{d\varepsilon_x^p}\right) \tag{26}$$

$$d\sigma_y = \lambda d\varepsilon_x + \mu d\varepsilon_x^p\left(1 - \frac{1}{1-2\nu}\frac{d\theta^p}{d\varepsilon_x^p}\right) \tag{27}$$

If $dY/dp > 0$, its effect on σ_x is to diminish the difference between elastic and plastic curves. Its effect on σ_y is to increase the difference, with the result that resolved shear stress is less than would be calculated for no plastic dilatation:

$$d(\sigma_x - \sigma_y) = 2\mu d\varepsilon_x - 3\mu d\varepsilon_x^p\left(1 - \frac{1}{3}\frac{d\theta^p}{d\varepsilon_x^p}\right) \tag{28}$$

The net effect is small, so that even if the assumptions of vanishing plastic dilatation and pressure-dependent yield were incompatible, errors would be very small. Both of these conditions have been assumed in the numerical program developed for this problem.

REFERENCES

Averbach et al., Trans. ASM 42, 112 (1950).

Bertholf, L. D. et al., J. Appl. Phys. 46, 3776 (1975).

Blackburn, L. D., L. Kaufman and M. Cohen, Acta Met. 13, 533 (1965).

Bowden, H. G. and P. M. Kelly, Acta Met. 15, 1489 (1967).

Bowles, J. S., Acta Crystallography, 162-171 (March 1951).

Breedis, J. F., Trans. Met. Soc. AIME 230, 1583 (1964).

Coe, R. S., Contrib. Mineral. Petrol. 26, 247 (1970).

Dandekar, D. P. and G. E. Duvall, in Metallurgical Effects at High Strain Rates, Plenum Press, 1973. R. W. Rohde, B. M. Butcher, J. R. Holland and C. H Karnes, Eds.

Decker, R. F., "Transformations in 25% Ni Steels." Paper No. 12 in Research Seminar on High-Nickel Alloys for High Temperatures: Iron-Nickel Alloys; Stainless Steels. March 20, 1960, The Duquesne Club, Pittsburgh, Pa. Sponsored and printed by the International Nickel Co., Development and Research Division.

Forbes, J. W., Ph.D. Thesis, Washington State University (1976).

Fowler, C. M., F. S. Minshall, and E. G. Zukas, in Response of Metals to High Velocity Deformation, P. G. Sherman and V. F. Zackay, Eds. Interscience, 1961.

Fowles, G. R., G. E. Duvall, J. Asay, P. Bellamy, F. Feistmann, D. Grady, T. Michaels, and R. Mitchell, Rev. Sci. Instr. 41, 984 (1970).

Gibbs, J. W., "On the Equilibrium of Heterogeneous Substances," Scientific Papers, Dover, 194 (1971).

Graham, R. A., D. H. Anderson, and J. R. Holland, J. Appl. Phys. 38, 223 (1967).

Gupta, Y. M., Acta Met. 25, 1509 (1977).

Gust, W. H. and E. B. Royce, J. Appl. Phys. 41, 2443 (1970).

Hilliard, J. E. and J. W. Cahn, Trans. AIME 221, 344 (1961).

Johnson, J. N. and W. Band, J. Appl. Phys. 38, 1578 (1967).

Johnson, J. N., O. E. Jones, and T. E. Michaels, J. Appl. Phys, 41, 2330 (1970).

Kamb, W. B., J. Geophys. R. 66, 259 (1961).

Kennedy, J. D. and W. B. Benedick, Bull. Am. Phys. Soc. II, 10, 1112 (1965).

Kennedy, J. D. and W. B. Benedick, J. Phys. Chem. Solids 27, 125 (1966).

Lawrence, R. J., Report No. SLA-73-0635, Sandia Laboratories, Albuquerque, N.M. (1973).

Leslie, W. C., D. W. Stevens, and M. Cohen, in High-Strength Materials, V. F. Zackay, ed., pp. 382-435, John Wiley and Sons, New York, 1964.

Lindgren, R., Metal Progress 57, 102 (1965).

Loree, T. R., R. H. Warnes, E. G. Zukas, and C. M. Fowler, Science 153, 1277 (1966).

Machlin, E. S. and M. Cohen, Trans. AIME - J. Metals, 1019 (Nov. 1951).

Malvern, L. E., Introduction to the Mechanics of a Continuous Medium, Prentice-Hall (1969), pp. 89-94.

Miller, R. L., Trans. A.S.M. 57, 892 (1964).

Otte, H. M., Acta Met. 5, 614 (1957).

Papadakis, E. P. and E. L. Reed, J. Appl. Phys. 32, 682 (1961).

Patel, J. R. and M. Cohen, Acta Met. 1, 531 (1953).

Paterson, M. S., Rev. Geophys. and Sp. Physics II, No. 2, 355 (1973).

Pope, L. E. and L. R. Edwards, Acta Met. 21, 281 (1973).

Reed, R. P. and J. F. Breedis, in Behavior of Materials at Cryogenic Temperatures, a symposium held at the 68th Annual Meeting of the ASTM, Lafayette, Ind., June 13-18, 1965. ASTM Special Technical Publication No. 387, pp. 60-132. LC No. Sci-TA-460-S9395.

Robin, P. Y. F., Am. Mineralogist 59, 1286 (1974).

Rohde, R. W., J. R. Holland, and R. A. Graham, Trans. Met. Soc. AIME 242, 2017 (1968).

Rohde, R. W. and R. A. Graham, Trans. Met. Soc. AIME 245, 2441 (1969).

Rohde, R. W., Acta Met. 18, 903 (1970).

Stepakoff, G. L. and L. Kaufman, Acta Met. 16, 13 (1968).

Van Thiel, M., Compendium of Shock Wave Data, UCLR-50108, Vol. 3, p. 662 (1977).

Wilkins, M. L., in Methods of Computational Physics, B. Alder, S. Fernbach and M. Rotenberg, eds., Vol. III, Acad. Press, New York (1964).

Zukas, E. G. and L. S. Levinson, private communication (1976).